

Contents

List of figures	VI
List of tables	VII
1 Introduction	1
1.1 Motivation	1
1.2 Troubles	1
1.3 Approach	2
2 Theory	3
2.1 Chemistry	3
2.1.1 Oxalic Acid	3
2.1.2 Phosphoric Acid	3
2.1.3 Aluminum Dissolution Acid	3
2.2 Ideal Gas Law	3
2.2.1 Boyle–Mariotte Law	3
2.3 Hexane	4
2.3.1 Saturated Vapor Pressure	4
2.3.2 Liquid Density	4
2.3.3 Gas Density	4
2.4 Laplace–Young equation	4
2.5 Kelvin Equation	4
2.6 Condensation and evaporation in a cylindrical pore	5
2.6.1 Closed pore	6
2.6.1.1 Closed straight pore	6
2.6.1.2 Closed funneled pore - large end open	6
2.6.1.3 Closed funnelled pore - small end open	6
2.6.2 Open cylindrical pore	7
2.6.2.1 Open straight pore	7
2.6.2.2 Open funnelled pore	7
2.6.3 Isotherm comparison	13
2.7 Snell's Law	13
2.8 Fresnel Equations	14
2.8.1 Two Interface Transmission	15
2.9 Blablabla Näherung	16
2.9.1 Transmission of Nanoporous Membranes in Empty and Filled State	17
2.9.1.1 Transmission of Empty AAM Membrane	17
2.10 Rayleigh Scattering	18
2.11 Index Matching	18
3 Experimental	19
3.1 Alumina membranes	19
3.1.1 Membrane production	19
3.1.1.1 Anodizing	19

3.1.1.2	Aluminum dissolution	21
3.1.1.3	Barrier layer dissolution	22
3.1.2	Membrane specifications	22
3.2	Experimental setup	23
3.2.1	Volumetric setup	23
3.2.1.1	Cell temperature regulation	24
3.2.1.2	Pressure gauges	24
3.2.2	Laser transmission setup	24
3.2.3	Camera setup	24
3.3	Experimental procedure	24
3.3.1	Bypass	25
3.3.1.1	Changing the membrane	26
4	Analysis	27
4.1	Isotherm computation	27
4.1.1	Volumetric isotherm	27
4.1.1.1	Porosity	29
4.1.1.2	Determination of the saturated vapor pressure	30
4.1.1.3	Diameter error using Kelvin equation	30
4.1.2	Optical measurements	30
4.2	Conducted measurements	31
4.3	Inhomogeneities on one wafer	32
4.4	Comparison of closed and open pores	32
4.4.1	Bad open pores	35
4.4.2	Inverse funnelling	35
4.4.2.1	Funnellization of closed pores increased by immersion in phosphoric acid	37
4.4.2.2	Inverse funnelling upon barrier layer dissolution	40
4.4.3	Etch rate difference	40
4.4.3.1	Pore opening widening pores much less than expected	40
4.4.3.2	Etch rate of phosphoric acid on alumina not clear	41
4.4.4	Do thinner membranes improve things?	42
4.4.5	Transmission signal not well understood	44
4.5	Pore quality linked to transmission drop and hysteresis	47
4.6	Testing theory using electron beam microscopy	47
4.7	Pore size reduction using atomic layer deposition	47
4.7.1	Atomic layer deposition effectively reduces pore diameters	49
4.7.2	Diameter reduction by atomic layer deposition is reproducible	49
4.7.3	Atomic layer deposition parameters need improvement	49
4.8	Isotherms proves powerful to detect and characterize defects	54
Bibliography		58

List of Figures

2.1	The graph shows the pressure to diameter conversion by KELVIN equation (compare eq. (2.7)) for the parameters $T = 19^\circ\text{C}$, $\gamma_{T=19^\circ\text{C}}^{\text{hexane}} = 0,018\,605 \frac{\text{N}}{\text{m}}$ and $V_{\text{mol}, T=19^\circ\text{C}}^{\text{hexane}} = 0,130\,53 \frac{\text{L}}{\text{mol}}$	5
2.2	Absorption (a) and desorption (b) isotherm of a straight cylindrical pore open on one end. The corresponding processes inside the pore are illustrated below the isotherm itself. Colors of the arrows between pore states and the respecting pressure range of the graph match.	8
2.3	Absorption (a) and desorption (b) isotherm of a funnelled cylindrical pore open on the large end. The corresponding processes inside the pore are illustrated below the isotherm itself. Colors of the arrows between pore states and the respecting pressure range of the graph match.	9
2.4	Absorption (a) and desorption (b) isotherm of a funnelled cylindrical pore open on the small end. The corresponding processes inside the pore are illustrated below the isotherm itself. Colors of the arrows between pore states and the respecting pressure range of the graph match.	10
2.5	Absorption (a) and desorption (b) isotherm of a straight cylindrical pore open on both ends. The corresponding processes inside the pore are illustrated below the isotherm itself. Colors of the arrows between pore states and the respecting pressure range of the graph match.	11
2.6	Absorption (a) and desorption (b) isotherm of a funnelled cylindrical pore open on both ends. The corresponding processes inside the pore are illustrated below the isotherm itself. Colors of the arrows between pore states and the respecting pressure range of the graph match.	12
2.7	Absorption and desorption isotherm loops for various kinds of cylindrical pores. For the funnelled pores it is $d > d'$	13
2.8	Visual derivation of SNELL's law.	14
2.9	Sketch for the derivation of the FRESNEL equations. The index i stands for the incident wave, r for the reflected and t for the transmitted. The continuity of the components parallel to the $n_1 - n_2$ -interface is visualized. For the derivation please see 2.8.	15
2.10	balblabla	16
2.11	Graphical solution of the inequality eq. (2.31). While the blue shaded area also respects the inequality eq. (2.25), the orange shaded area shows the more general case $1 = n_1 < n_2, n_3$. Both cases yield a weaker transmission for the two interface transmission than for the single interface.	17
2.12	Using the blabla approximation for the refractive index of a nanoporous medium the transmission in its empty state is computed in section ???	18
3.1	Setup for the anodizing of the membrane production. The aluminum wafer functions as anode while a platinum plate makes for the cathode. The oxalic acid is stirred during the whole process.	20

3.2	Production stages of the membrane production. It starts with a wafer of bulk aluminum (dark gray) (a) which is then anodized yielding (b), where light gray represents alumina. The latter is then dissolved producing a bulk aluminum wafer with hexagonally arranged hollows (c). By the second anodizing straight parallel pores are created (d). After dissolving the remaining aluminum (e) the barrier layer etched to open the pores (f). For the variable specifications please refer to section 3.1.1.	21
3.3	Setup for the aluminum dissolution step. The wafer is immersed in acid composed according to eq. (3.6) which dissolves aluminum according to section ???	22
3.4	Setup for the <i>barrier layer</i> dissolution. The wafer is floated (a) or immersed (b) in phosphoric acid dissolving alumina according to section ??? . For best results a combination of floating and immersing is used (please refer to section 3.1.1.3 for clarification of <i>best</i>).	22
3.5	Experiment setup with bypass which allows to pump the whole system without changing the opening of the PFEIFFER microvalve. The temperatures within the reservoir and the cell are measured by the thermometers T_{res} and T_{cell} . Furthermore, P_{res} and P_{cell} are the two installed pressure gauges. The void is experimentally realized by a primary pump.	23
3.6	Sketch of the laser transmission setup.	24
3.7	Experiment setup with bypass which allows to pump the whole system without changing the opening of the PFEIFFER microvalve. The temperatures within the reservoir and the cell are measure by the thermometers T_{res} and T_{cell} . Furthermore, P_{res} and P_{cell} are the two installed pressure gauges. The void is experimentally realized by a primary pump. Furthermore, the laser transmission setup and the camera setup are outlined. Only one of the two is set in place at the same time though.	25
4.1	Raw volumetric isotherm data recorded with the experimental setup as explained in section 3.3 for one cycle without a membrane inside the cell and one with a membrane inside the cell. (a) shows the pressure values over time making the condensation and evaporation plateaus of absorption and desorption of hexane within the membrane's pores visible. (b) is the pressure loop which is relevant for the computation of the isotherms. Again, the before mentioned plateaus are visible as dips in the time derivative of the pressure.	28
4.2	(a) shows the raw data of the isotherm with membrane and interpolation of the reference isotherm without membrane. Also, the subtraction of the latter (compare integrand of eq. (4.1)) is plotted where the area to be integrated for the absorption and desorption isotherm is shaded light green. The integration according to eq. (4.3) results in the isotherm displayed in (b).	29
4.3	Wafer 295 and 296 processing scheme. While a  signifies a recorded isotherm, the  means MEB pictures have been taken. Red marks pores closed on one end, green pores open on both ends. The processed wafers are immersed in phosphoric acid for t_{immerse} or floated on for t_{float}	31
4.4	Convention used to assign membrane depending on their position on the wafer.	32
4.5	Comparison of closed pore membranes of one wafer. (a) compares membranes of wafer 296 while fig. 4.5(b) deals with 295.	33
4.6	Comparison of open pore membranes of one wafer. (a) compares membranes of wafer 292 while fig. 4.6(b) deals with 295.	34
4.7	Comparison of the isotherms of membranes with closed pores to those with open pores. (a) shows membranes of wafer 296, while (b) displays those of wafer 295. The increase of size of the hysteresis is clearly observable.	36
4.8	Full comparison of the closed pore membranes of wafer 296 with the open pore membrane 296b'. For interpretation please refer to section 4.4.	37

4.9	Images taken of wafer 295 during the <i>barrier layer</i> dissolution process. (a) shows milky aspects that appear after approximately twenty minutes while (b) has been taken just before removing the wafer from the acid. At this point the whole surface of the wafer is covered by phosphoric acid that passed through the pores.	38
4.10	Membrane 296c' has been immersed in phosphoric acid for $t_{296c'} = 13$ min, 296d' for $t_{296d'} = 26$ min. (a) shows the isotherms of the immersion experiment conducted using wafer 296. The shift to larger pressures of the beginning of the evaporation branch and the unmoving beginning of the condensation branch are clearly visible. (b) and (c) are higher resolution plots of the relevant areas of the evaporation and respectively condensation branch of the isotherm on a pore diameter scale. For interpretations please refer to ???. ???EXPLAIN WHY EVAP START AND COND START ARE THE SPOTS TO LOOK AT ???	39
4.11	Immersion of a closed pore membrane resulting in an increase of the funnelling aspect of the pores as shown in (b) due to the saturation of the acid within the pores. The visualized theory is backed by the isotherms in fig. 4.10(a) which lead to the etch rate dependency plotted in (a) on the height within a pore. For further explanations please refer to ???.	40
4.12	Comparison of the isotherms measured for the membranes 296a, 296e' and 296f'. While the pore diameters are marginally smaller for the membranes 296e' and 296f' than they are for 296a, the overall picture is equivalent. It makes for closed pores (or constricted open pores as explained in section 4.4) with the same funnelling aspect.	41
4.13	Electron beam microscopy images of membrane 296e' that has been floated on acid for $t_{fl} = 13$ min. (a) shows the cross section view with the attempt to measure the thickness of the membrane's <i>barrier layer</i> , while (b) is the aluminum side on which the membrane has been floated on.	42
4.14	43
4.15	Electron beam microscopy images of membrane 295g' with measurements of the pore diameters on the solution side (a) and aluminum side (b).	44
4.16	P_{rel} transmission isotherms of the membranes 292d (a), 296b' (b), 295d' (c), and 295f" (d). All membranes have open pores. Unlike the isotherm of membrane 292d, the transmission drops of condensation and evaporation are of the same magnitude. The magnitudes of condensation and evaporation dip are reversed in respect to membrane 292d for membrane 295f 200ALD.	45
4.17	Disorder between neighboring pores during absorption (a) and desorption (b). Important is the larger degree of disorder upon the absorption process. Upon condensation pores fill immediately when the spinodal pressure $P_{sp}(d_{min})$ is reached, where d_{min} is the radius of the opening at the small end. The evaporation is continuous at equilibrium pressure $P_{eq}(d)$ and empties each pore simultaneously while the diameter d is large enough.	46
4.18	Comparison of the isotherms of the membranes 295d' and 295g' on a KELVIN diameter axis. Important for the analysis in section 4.5 is.	47
4.19	Comparison of membrane 295e' in initial open pore state and after 100 and 200 cycles of ALD over relative pressure axis in (a). While the shape of the isotherm does not change for the first 100 cycles, the result after the second 100 cycles is drastic. (b) shows the comparison of initial state membrane 295e' and 100 cycles of ALD membrane 295e" on a KELVIN diameter axis. For analysis please read section 4.7.	48
4.20	Full comparison of the closed pore membranes of wafer 296 with the open pore membrane 296b'. For interpretation please refer to section 4.4.	50

4.21 Plots for the analysis of membrane 295e". (a) shows the isotherms over relative pressure while (b) shows it over a KELVIN diameter axis. On the latter graph, the isotherm data of membrane 295e'' is converted once using the KELVIN equation for open pores and once using it for closed pores. The black circles mark the overlap of the signals on the same diameter range.	51
4.22 Plots for the analysis of membrane 295f". (a) shows the isotherms over relative pressure while ?? shows it over a KELVIN diameter axis. On the latter graph, the isotherm data of membrane 295f'' is converted once using the KELVIN equation for open pores and once using it for closed pores. The black circles mark the overlap of the signals on the same diameter range.	52
4.23 Electron beam microscopy images of membrane 295f''. (a) and (b) show images of the solution and aluminum side with pore diameter measurements. (c) captures the grayscale gradient on the membrane's cross section which gets lighter upon approaching the center from both sides.	53
4.24 Isotherm measurement of membrane 295d". The volumetric isotherm does not show any signal whereas the transmission measurement yields a lower transmission coefficient at saturated vapor pressure than in vacuum.	54
4.25 The isotherm of membrane 295c is shown in (a). To analyse the two step condensation, the isotherm is plotted on a pore diameter scale using the KELVIN equation (section 2.5) once under the assumption of condensation at equilibrium pressure for closed pores (cp) and once under that of spinodal pressure for open pores (op) in (b). For interpretations please read ??.	56
4.26 MEB images of the aluminum side of membrane 295c. Areas of none open pores are clearly visible.	57

List of Tables

4.1	Wafer specifications. The wafers thickness l_{pore} , floating time t_{float} of the <i>barrier layer</i> dissolution process and pore diameter dispersion $\Delta d_{\text{pore}}^{\text{MEB}}$ measured by electron beam microscopy are noted. The latter two parameters apply to the open pore membranes of the respective wafer.	32
4.2	Diameter reduction per minute of immersion derived from the isotherms of the membranes 296a, 296c, 296d.	38

1 Introduction

1.1 Motivation

The fundamental idea is to test models of condensation and evaporation of liquids in confinement. To this end, a well characterized confinement is necessary. The latter shall be realized using nanoporous alumina membranes. The production of these is rather advanced as they are commonly used for the production of nanowires. Moreover, the shape of the pores is ideally cylindrical which makes for a simple geometry. A nanoporous alumina membrane includes a large number of parallel pores. Therefore, any experiment conducted on one of these membranes yields a result that averages over all of these pores. This is why, ideally, monodisperse alumina membranes shall be produced.

As a liquid to condense inside the pores of these membranes, hexane is used. There are multiple reasons for that. First, other teams have used hexane for this type of experiments before. This means that reference isotherms exist that the results can be compared to. Moreover, hexane permits to experiment at ambient temperature which makes things much easier. The fact that this is only a preexperiment for later experiments using helium, the use of liquids like nitrogen seems to make experimenting more difficult while offering no advantages.

The models to be tested are primarily the KELVIN equation and the SAAM and COLE theory. There are multiple variations though, as for example there is a modified KELVIN equation taking into account the wetting film which the basic KELVIN equation does not. In addition to that, thermal activation and the temperature relative to the critical temperature of the used fluid are relevant. The latter is one reason why finally, the experiment is planned to be conducted using helium. Finally, there are other more sophisticated models that need to be tested. Due to the small variations that are expected, again, the probing of the latter requires helium. Last but not least, in order to also study cavitation in alumina membranes, inc bottle like cavities with constricted openings must be produced. As for both, the helium experiments and for the inc bottle openings, pores of sub ten nanometer diameter must be synthesized in a controlled way, the production process needs to be improved. This becomes the main goal of the conducted experiments described in this article.

1.2 Troubles

Early on, the conducted experiments prove the membranes to be not as ideal as was hoped for. The idea of the perfect cylindrical pores of the same diameter is replaced by the conclusion that the pores' diameter is not only distributed over the membranes but also varies within a single pore. This variation manifests in the way of a funnelling aspect that makes for a conical shape, rather than a cylindrical, and also as corrugations. As explained above, the confinement needs to be well characterized to be able to test the models of condensation and evaporation. In contrast to that, the geometrical shape of the pores does not allow for this kind of precise characterization. Using electron beam microscopy, the opening diameters of the pores can be checked on top and bottom side. Furthermore, a cross section view yields some information about the straightness and possible defects along the length of the pores. As the pores' length ranges in the order of micrometers though, while the diameters' magnitude is nanometers, this still gives little information about the overall pore shape. Moreover, the microscopy images can not be precisely evaluated due to the unknown porosity of the membranes and again the lack of information on the shape. In the course of the experiments

a way is developed to at least delimit a range for the porosity and so allow for a more sophisticated analysis of the electron beam microscopy images under the assumption of a certain pore geometry.

The bottom line is that neither the exact geometry and distribution of pore shapes and sizes is known, nor are the condensation and evaporation models clear. Thus, the first step must be to understand and refine the production process of the membranes and to hereby make for the best possible characterization of the confinement.

1.3 Approach

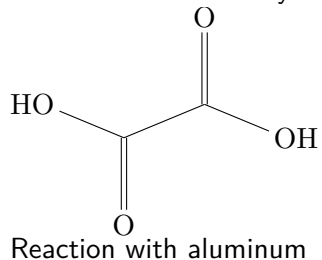
To understand the membranes' characteristics and to use this knowledge to improve the production process, rather large pore diameters of above fourty nanometer diameter, for which KELVIN equation is assumed to be sufficiently precise, are probed using multiple techniques. The core of the conducted experiments relies on thermodynamics using volumetric measurements. In addition, optical measurements and also visual documentation are used along with electron beam microscopy. All the aquired data is then interpreted and tested for coherence to finally draw conclusions on the membranes' characteristics. From the aquired results, questions rise about the effects of different production steps which are then taken a closer look at.

2 Theory

2.1 Chemistry

2.1.1 Oxalic Acid

Oxalic acid is a dicarboxylic acid with the formula C₂H₂O₄.



2.1.2 Phosphoric Acid

2.1.3 Aluminum Dissolution Acid

2.2 Ideal Gas Law

The ideal gas law can be written as

$$PV = nRT \quad (2.1)$$

with the pressure P , volume V , number of moles of gas n , temperature T and ideal gas constant

$$R = 8,314\,459\,8(48) \frac{\text{J}}{\text{K mol}}. \quad (2.2)$$

It is an approximation of the behaviour of gases which can be applied for sufficiently low pressures and simple atoms or molecules which do not interact strongly (for example noble gases).

2.2.1 Boyle–Mariotte Law

For a constant temperature T and constant number of moles of gas n , the ideal gas law eq. (2.1) yields the BOYLE-MARIOTTE law

$$P_1V_1 = P_2V_2. \quad (2.3)$$

It permits to measure a volume V_2 by expanding the known volume V_1 of gas and monitoring pressures P_1 and P_2 before and after the expansion.

2.3 Hexane

2.3.1 Saturated Vapor Pressure

2.3.2 Liquid Density

2.3.3 Gas Density

2.4 Laplace-Young equation

Due to the surface tension γ , the interface between two static fluids is curved. The shape of this curvature is related to the capillary pressure difference ΔP sustained across the mentioned interface by the YOUNG-LAPLACE equation

$$\begin{aligned}\Delta P &= -\gamma \cdot \nabla \hat{\mathbf{n}} \\ &= \gamma \left(\frac{1}{R_1} + \frac{1}{R_2} \right),\end{aligned}\quad (2.4)$$

with the unit vector $\hat{\mathbf{n}}$ orthogonal to the interface and the curvature radii R_1 and R_2 . The relation so implies, that the surface of a gas-liquid interface will always strive towards a homogeneous curvature to achieve an equilibrium state regarding pressure differences along the surface.

2.5 Kelvin Equation

To get to Kelvin equation from Laplace young equation one uses the equality of chemical potentials $\mu_{Liquid}(P_{liquid}) = \mu_{Gas}(P_{gas})!!!$

liquid incompressible

integration of gibss duhem realtion leads to chemical potential dependent on the density

$$dG = SdT + VdP - Ndm \text{umit} T = constantV \quad (2.5)$$

$$dG = VdP - Ndm \mu \quad (2.6)$$

The KELVIN equation is given by

$$RT \cdot \ln \left(\frac{p_v}{p_{sv}} \right) = \gamma V_m \cdot \left(\frac{1}{r_1} + \frac{1}{r_2} \right), \quad (2.7)$$

with the gas constant R , the temperature T , p_v the vapor pressure and p_{sv} the saturated vapor pressure. Furthermore, γ is the surface tension, V_m the molar volume and r_i , $i \in \{1, 2\}$, are the radii defining the curvature of the meniscus that forms the surface of the liquid.

The conducted experiment makes use of samples with cylindrical pores. Thus, the volume's radii become

$$r_1^{\text{cyl}} = r^{\text{cyl}} < 0, \quad r_2^{\text{cyl}} \rightarrow \infty$$

for a cylindrical meniscus and

$$r_1^{\text{hsp}} = r_2^{\text{hsp}} = r^{\text{hsp}} < 0$$

for a hemispheric meniscus. Plugging these radii into equation eq. (2.7) yields the respecting KELVIN equations for a cylindrical volume

$$RT \cdot \ln \left(\frac{p_v^{\text{cyl}}}{p_{sv}} \right) = \frac{\gamma V_m}{r^{\text{cyl}}} < 0 \quad (2.8)$$

$$RT \cdot \ln \left(\frac{p_v^{\text{hsp}}}{p_{sv}} \right) = 2 \cdot \frac{\gamma V_m}{r^{\text{hsp}}} < 0 \quad (2.9)$$

and thus,

$$\ln\left(\frac{p_v^{\text{cyl,hsp}}}{p_v}\right) < 0 \implies p_v^{\text{cyl,hsp}} < p_v.$$

The equations eq. (2.8) and eq. (2.9) each can be solved for the radius

$$r^{\text{cyl}} = \frac{\gamma V_m}{RT} / \ln\left(\frac{p_k^{\text{cyl}}}{p_v}\right) \quad (2.10)$$

$$r^{\text{hsp}} = 2 \cdot \frac{\gamma V_m}{RT} / \ln\left(\frac{p_k^{\text{hsp}}}{p_v}\right) = 2 \cdot r^{\text{cyl}}. \quad (2.11)$$

Here, the factor of 2 between the two conversions is of much importance for the understanding of the theory of condensation and evaporation in cylindrical pores. The conversion is illustrated in fig. 2.1 for a cylindrical and a spherical meniscus (respectively the equilibrium and the spinodal mechanism). In the course of this report, the isotherms will be displayed on a

$$P_{\text{rel}} = \frac{P_v}{P_{\text{sv}}} \quad (2.12)$$

axis. Nevertheless, a lot of the analysis will be done talking pore diameters. In doubt, please refer to fig. 2.1 for a conversion.

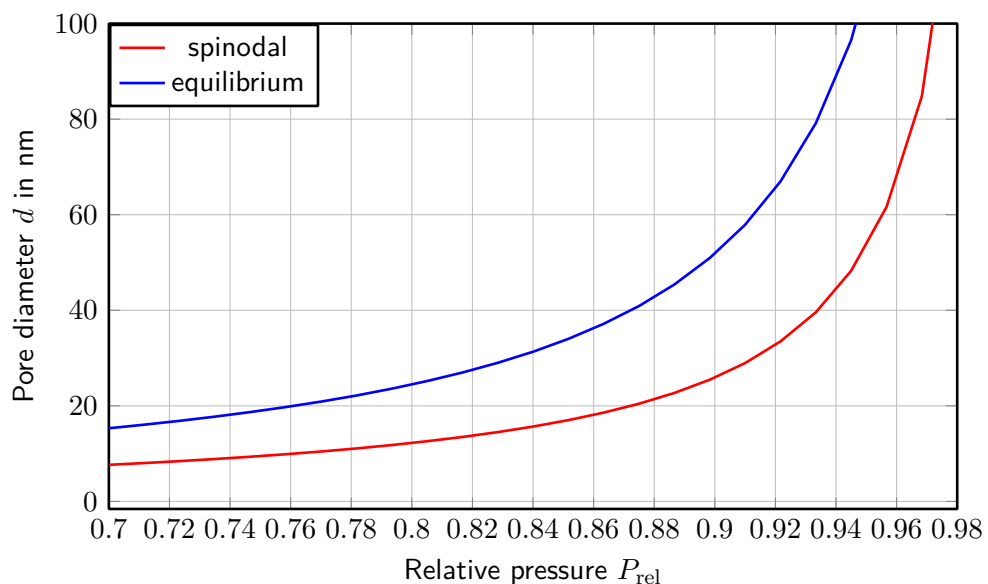


Figure 2.1 The graph shows the pressure to diameter conversion by KELVIN equation (compare eq. (2.7)) for the parameters $T = 19^\circ\text{C}$, $\gamma_{T=19^\circ\text{C}}^{\text{hexane}} = 0,018\,605 \frac{\text{N}}{\text{m}}$ and $V_{\text{mol}, T=19^\circ\text{C}}^{\text{hexane}} = 0,130\,53 \frac{\text{L}}{\text{mol}}$.

2.6 Condensation and evaporation in a cylindrical pore

To understand the condensation and evaporation of hexane in the alumina membranes, used for the conducted experiments, the processes must be understood for a single pore. The following explanation starts off with a straight cylindrical pore which is closed on one end. Then, funnelization is included in the theory. Finally, the model is applied to cylindrical pores open on both ends, straight and funnelled.

As a precondition, all pores are wetting. This means when exposed to vapor, a liquid film forms on their surface.

2.6.1 Closed pore

The term *closed pore* shall from now on be linked to a pore that is only open at one end.

2.6.1.1 Closed straight pore

The absorption isotherm of a straight cylindrical pore is illustrated in fig. 2.2 (a) with the corresponding processes inside the pore. Exposing the pore to vapor yields a wetting film on its surface (orange pressure range of the isotherm). As by LAPLACE-YOUNG eq. (2.4) different radii of menisci correspond to different pressures. Therefore, the film starts forming a spherical meniscus at the closed end of the pore (green). Upon reaching equilibrium pressure $P_{\text{eq}}(d)$ the pore fills due to the translational symmetry of the meniscus leaving only a spherical meniscus at the open end (red). The latter relaxes with increasing pressure till an even surface is left at saturated vapor pressure P_{sv} (blue).

Figure 2.2 (b) shows the corresponding desorption isotherm. When lowering the pressure from saturated vapor pressure, a spherical cap meniscus forms on the open end of the pore (orange pressure range of the isotherm). At equilibrium pressure this meniscus becomes spherical and invariant to translation inside the pore (green). Therefore, the pore empties except for a film on its surface (red). The film gets thinner with decreasing pressure and completely disappears when vacuum is reached.

2.6.1.2 Closed funneled pore - large end open

The absorption isotherm of a funnelled pore that is closed on the small end is shown in fig. 2.3 (a). Increasing the vapor pressure yields a thickening wetting film on the surface of the pore (orange pressure range of the isotherm). At the bottom of the pore a spherical cap meniscus forms that becomes a spherical meniscus at equilibrium pressure $P_{\text{eq}(r')}$ (green). At this point the pore starts to fill significantly with increasing pressure. It does not fill at one given pressure though as for the meniscus to move to larger radii, the pressure must also increase. Except for the spherical meniscus at the open end, the pore is filled at equilibrium pressure $P_{\text{eq}}(d)$. This continuous filling is implied by the red colored range of the absorption isotherm. The spherical meniscus relaxes into a spherical cap meniscus and finally transforms into an even surface at saturated vapor pressure.

The desorption isotherm is illustrated in fig. 2.3 (b). First, a spherical cap meniscus forms on the open end (orange) which transforms into a spherical meniscus upon reaching equilibrium pressure $P_{\text{eq}}(d)$ (green). At this pressure the pore begins to empty continuously till $P_{\text{eq}}(d')$ is reached (red). Only a film covering the pore's surface is left. The latter evaporates with decreasing pressure and a dry pore is left at zero pressure.

2.6.1.3 Closed funnelled pore - small end open

Figure 2.4 (a) shows the absorption isotherm of a funnelled pore that is closed at the large end. With increasing vapor pressure a film forms on the pore's surface (orange pressure range of the isotherm) and a spherical cap meniscus forms at the closed end. The latter becomes a spherical meniscus upon reaching equilibrium pressure $P_{\text{eq}}(d)$ (green). As

$$P_{\text{eq}}(d) < P_{\text{eq}}(d') \quad (2.13)$$

holds for this type of pore, the latter fills completely at this pressure. Only a spherical cap meniscus at the open end is left as the current vapor pressure, according to eq. (2.13), already exceeds the respecting equilibrium pressure. The liquids surface flattens at saturated vapor pressure.

The corresponding desorption isotherm is illustrated in fig. 2.4 (b). Decreasing the vapor pressure starting at saturated vapor pressure P_{sv} yields a spherical cap meniscus at the open end of the pore

(orange). The meniscus evolves to a spherical meniscus upon reaching equilibrium pressure $P_{\text{eq}}(d')$ (green). At this pressure, due to eq. (2.13), the pore empties completely leaving only a wetting film on its surface (red). The latter disappears in vacuum.

2.6.2 Open cylindrical pore

The term *open pore* shall from now on be linked to a pore that is open at both ends.

2.6.2.1 Open straight pore

Figure 2.5 (a) shows the desorption isotherm of an open pore of straight cylindrical shape and the corresponding processes inside the pore. As a wetting pore of diameter d is regarded, a film of liquid appears on the inside of the pore at low pressures already (orange pressure range of the isotherm). The latter forms a cylindrical meniscus. Upon increasing the pressure, the film thickens in correspondence to the green pressure range of the isotherm. Reaching the spinodal pressure $P_{\text{sp}}(d)$, the films collapse yielding a filled pore with menisci at either open end (red). The menisci are spherical cap menisci as

$$P_{\text{eq}}(d) < P_{\text{sp}}(d) < P_{\text{sv}} \quad (2.14)$$

holds for this type of pore, where $P_{\text{eq}}(d)$ is the equilibrium pressure and P_{sv} the saturated vapor pressure. The menisci relax upon further increasing the pressure and finally transform into even surfaces at saturated vapor pressure (blue).

The desorption isotherm of a straight cylindrical pore is illustrated in fig. 2.5 (b). Again, the corresponding processes inside the pore are illustrated below. At first, spherical cap menisci form on either end of the filled pore (orange). Upon reaching equilibrium pressure $P_{\text{eq}}(d)$ these menisci are spherical (green) and invariant regarding translation along the pore axes. Moreover, the vapor is not saturated yet, so the pore empties leaving only a film of liquid on the inside of the pore (red). The film gets thinner with decreasing pressure and disappears at saturated vapor pressure (blue).

As condensation and evaporation for a perfect cylindrical pore occur on two different values of vapor pressure, the spinodal pressure P_{sp} and the equilibrium pressure P_{eq} , the process yields a hysteresis. A complete isothermal loop of condensation and evaporation is shown in fig. 2.7.

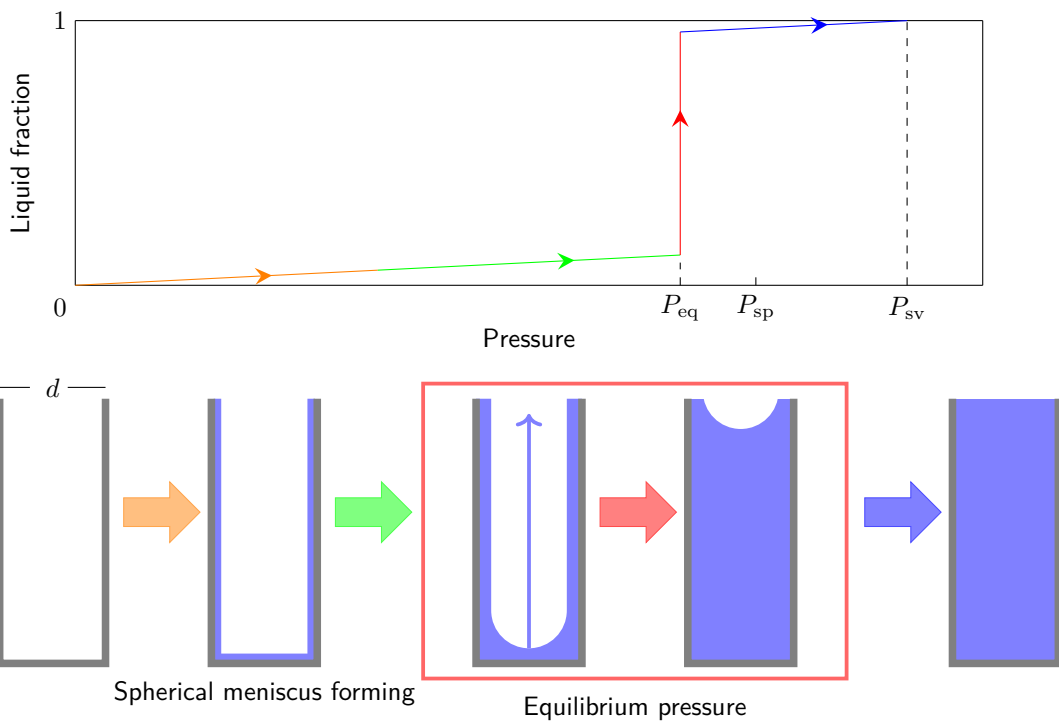
2.6.2.2 Open funnelled pore

Here, a funnelled cylindrical pore that is open at both ends is regarded. A precondition shall be that the funnelization is small in respect to the pore's diameter, in explanation

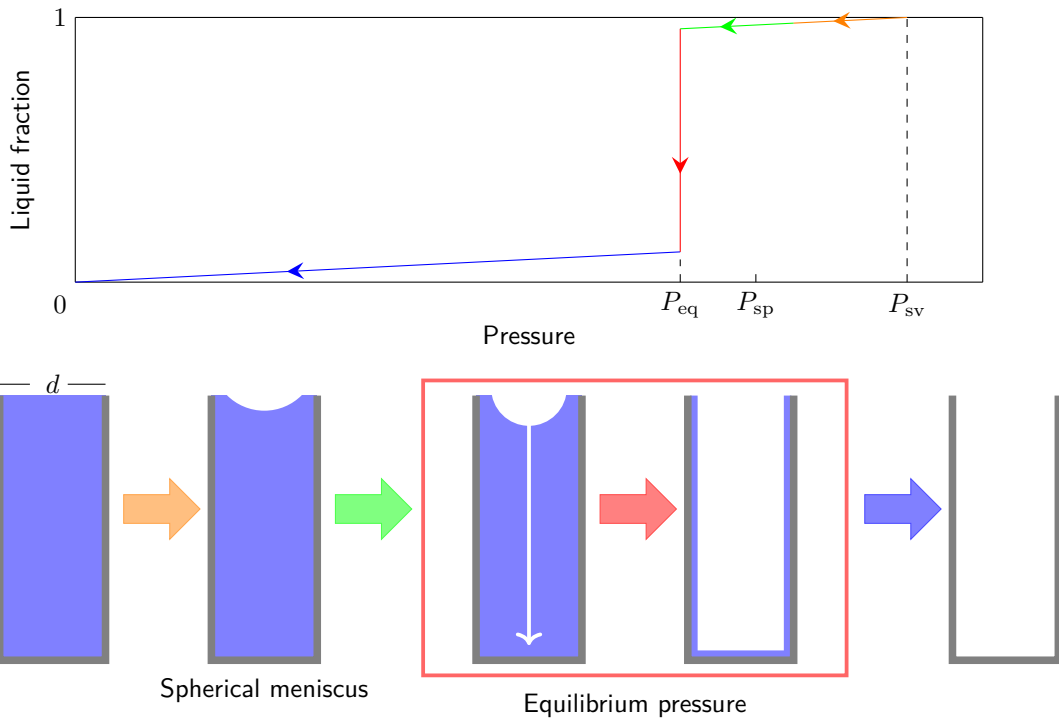
$$P_{\text{sp}}(d') \geq P_{\text{eq}}(d). \quad (2.15)$$

The absorption isotherm is illustrated in fig. 2.6 (a). Exposed to vapor, the surface of the pore wets leaving a thickening film (orange and green pressure range of the isotherm). At spinodal pressure $P_{\text{sp}}(d')$, the films collapse on the small end of the pore yielding a closed pore. The liquid bridge forms spherical menisci on both sides and in reference to eq. (2.15), the pore fills completely leaving only a spherical cap meniscus at each end. These relax when further increasing the vapor pressure and disappear at saturated vapor pressure P_{sv} .

Figure 2.6 (b) shows the desorption isotherm of the regarded pore. Spherical cap menisci form at both ends when reducing the vapor pressure from saturated vapor pressure (orange pressure range of the isotherm). Upon reaching equilibrium pressure $P_{\text{eq}}(d)$, the meniscus on the large end transforms into a spherical meniscus (green). Then, the pore starts to continuously empty from the large end with decreasing pressure. At $P_{\text{eq}}(d')$, only a wetting film is left on the surface of the pore (red). This film disappears at zero pressure (blue).

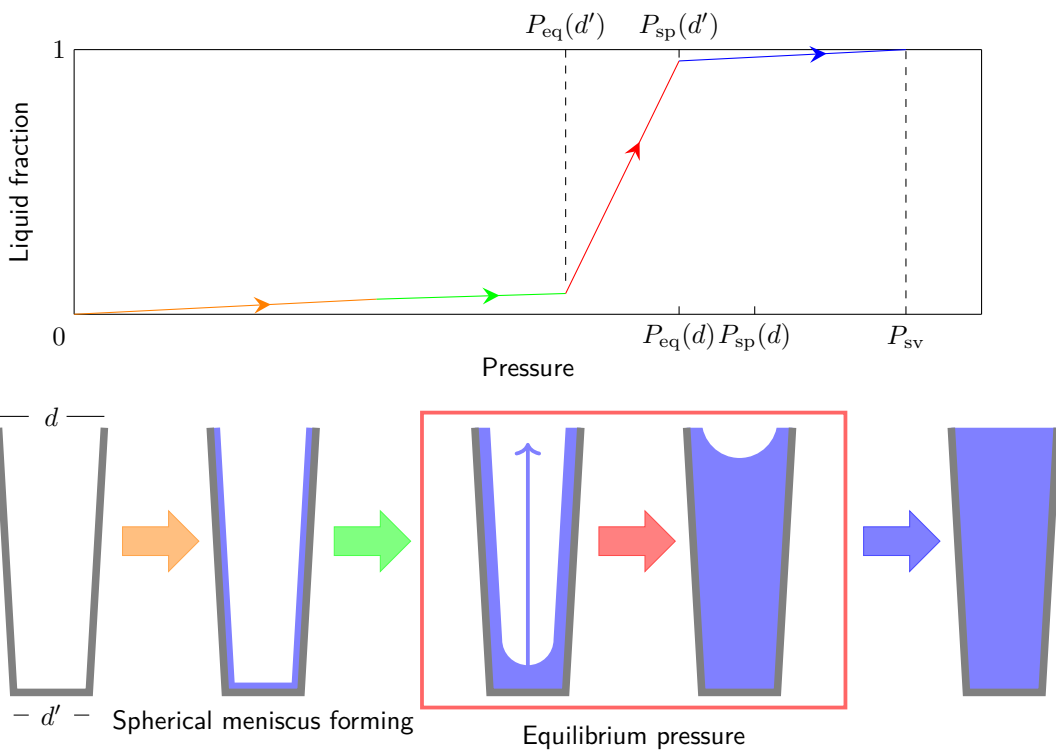


(a) Absorption isotherm. Significant is the absorption at equilibrium pressure.

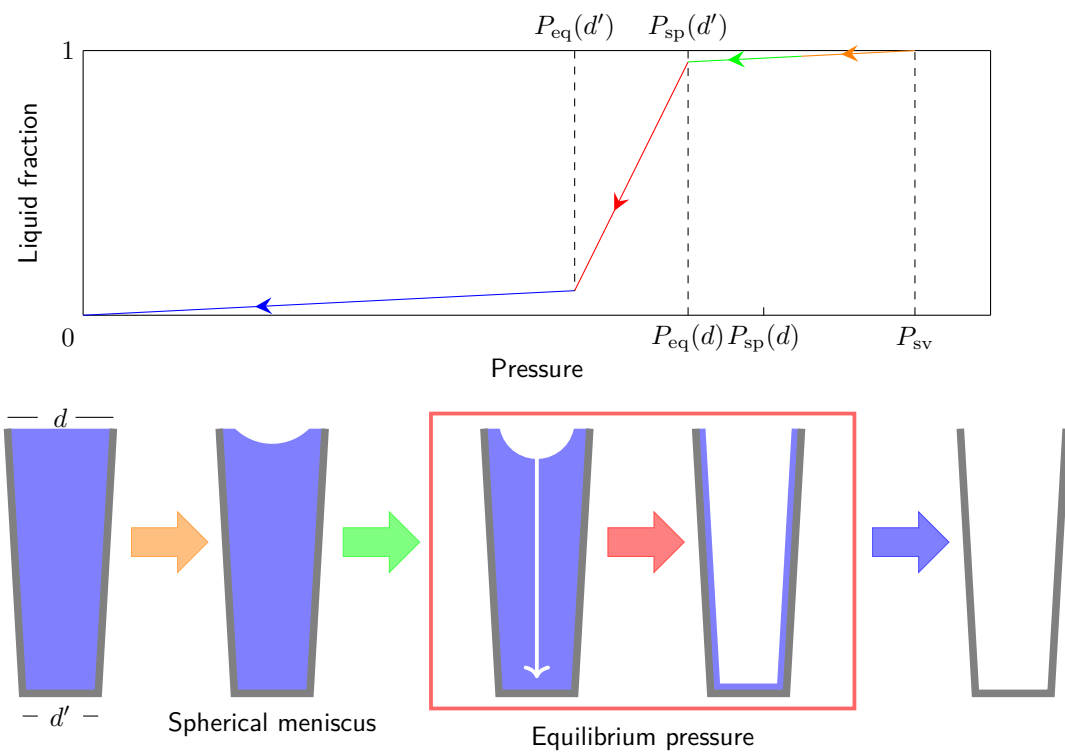


(b) Desorption isotherm. Significant is the desorption at equilibrium pressure.

Figure 2.2 Absorption (a) and desorption (b) isotherm of a straight cylindrical pore open on one end. The corresponding processes inside the pore are illustrated below the isotherm itself. Colors of the arrows between pore states and the respecting pressure range of the graph match.

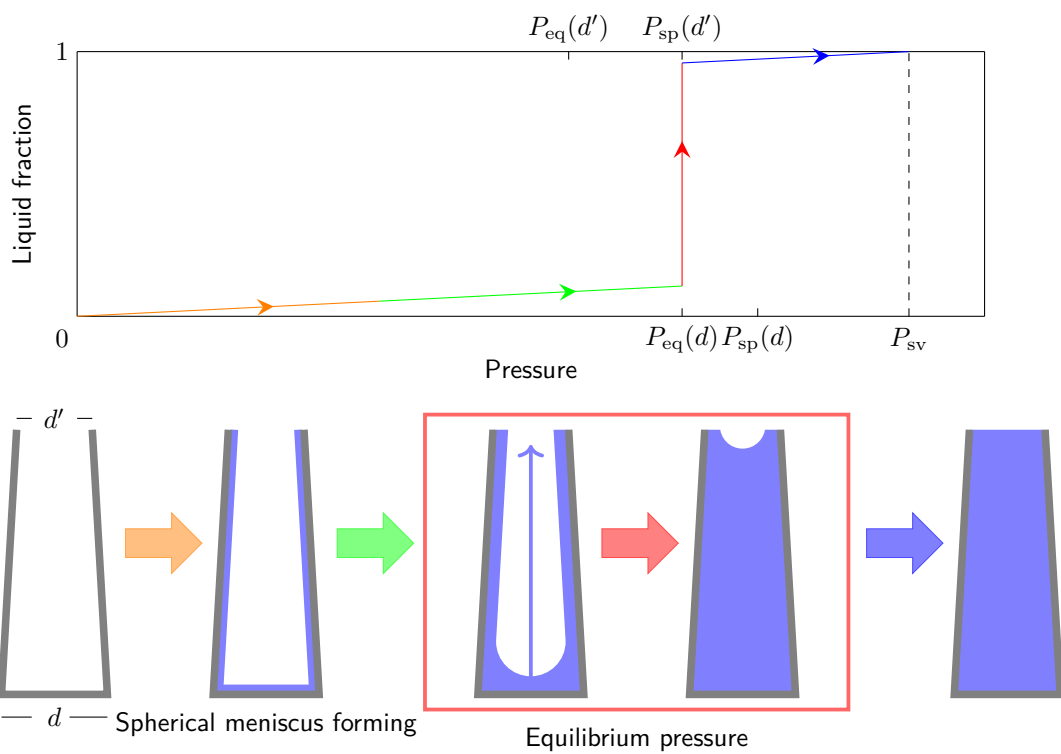


(a) Absorption isotherm. Significant is the absorption at equilibrium pressure.

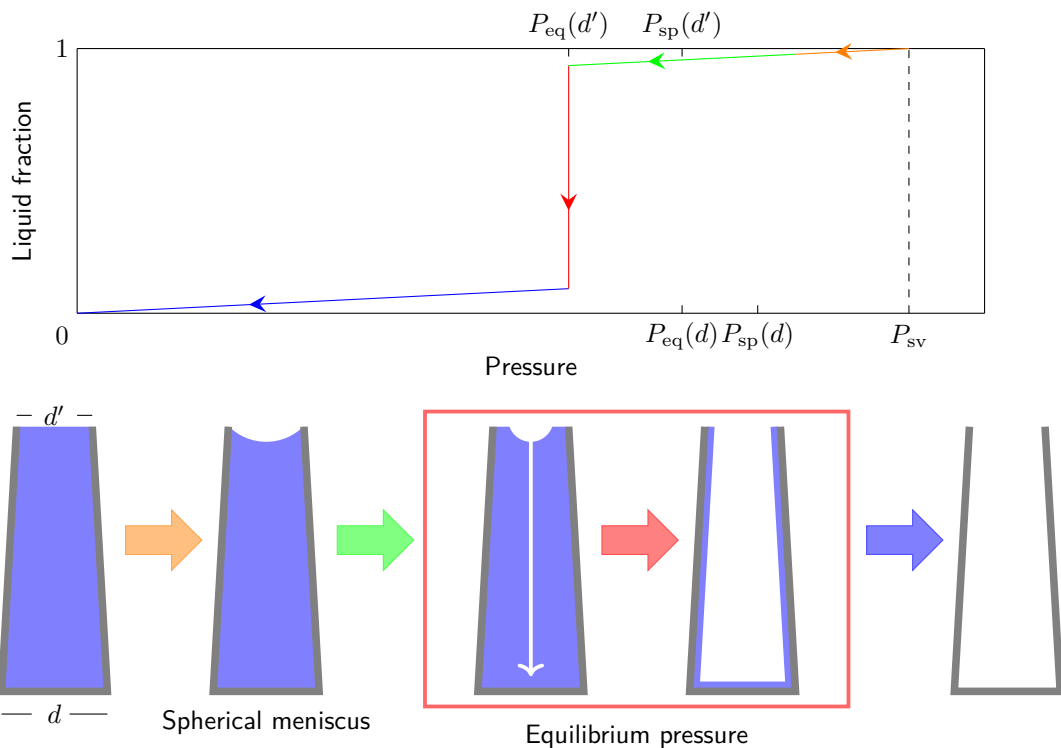


(b) Desorption isotherm. Significant is the desorption at equilibrium pressure.

Figure 2.3 Absorption (a) and desorption (b) isotherm of a funnelled cylindrical pore open on the large end. The corresponding processes inside the pore are illustrated below the isotherm itself. Colors of the arrows between pore states and the respecting pressure range of the graph match.

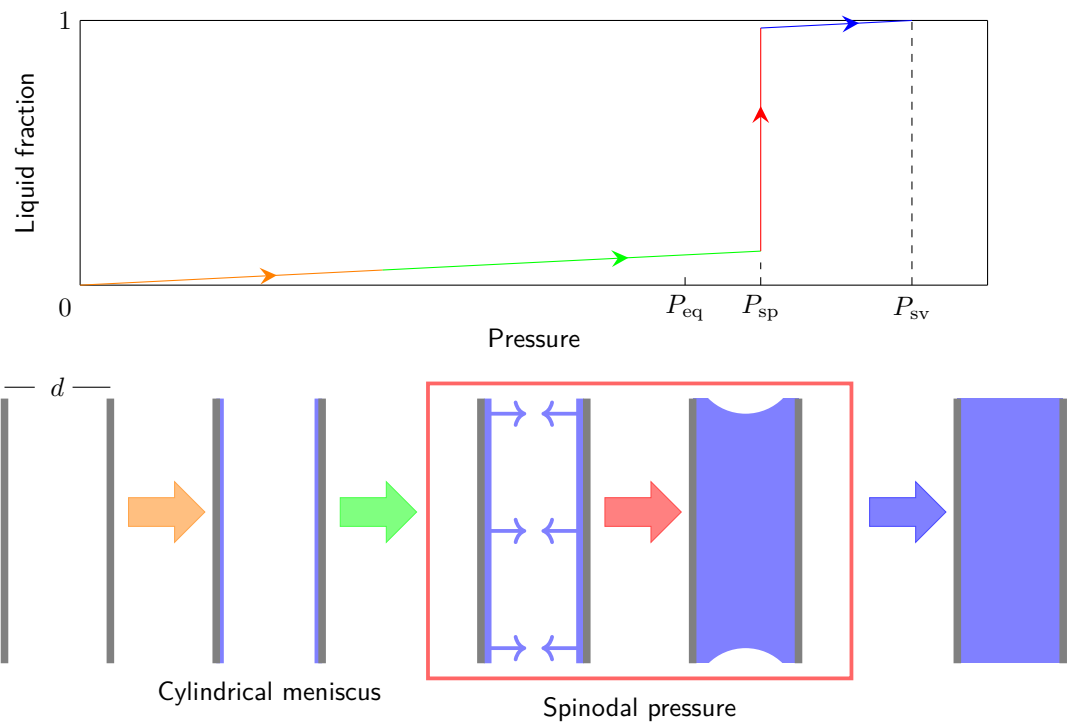


(a) Absorption isotherm. Significant is the absorption at equilibrium pressure $P_{eq}(d)$.

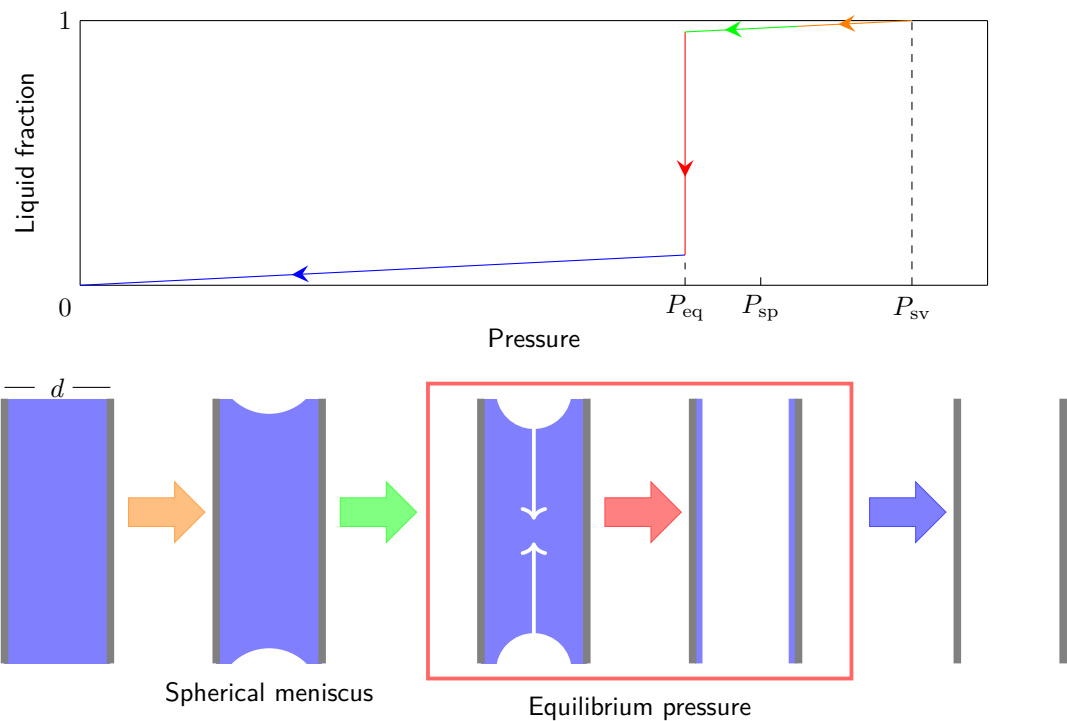


(b) Desorption isotherm. Significant is the desorption at equilibrium pressure $P_{eq}(d')$.

Figure 2.4 Absorption (a) and desorption (b) isotherm of a funnelled cylindrical pore open on the small end. The corresponding processes inside the pore are illustrated below the isotherm itself. Colors of the arrows between pore states and the respecting pressure range of the graph match.

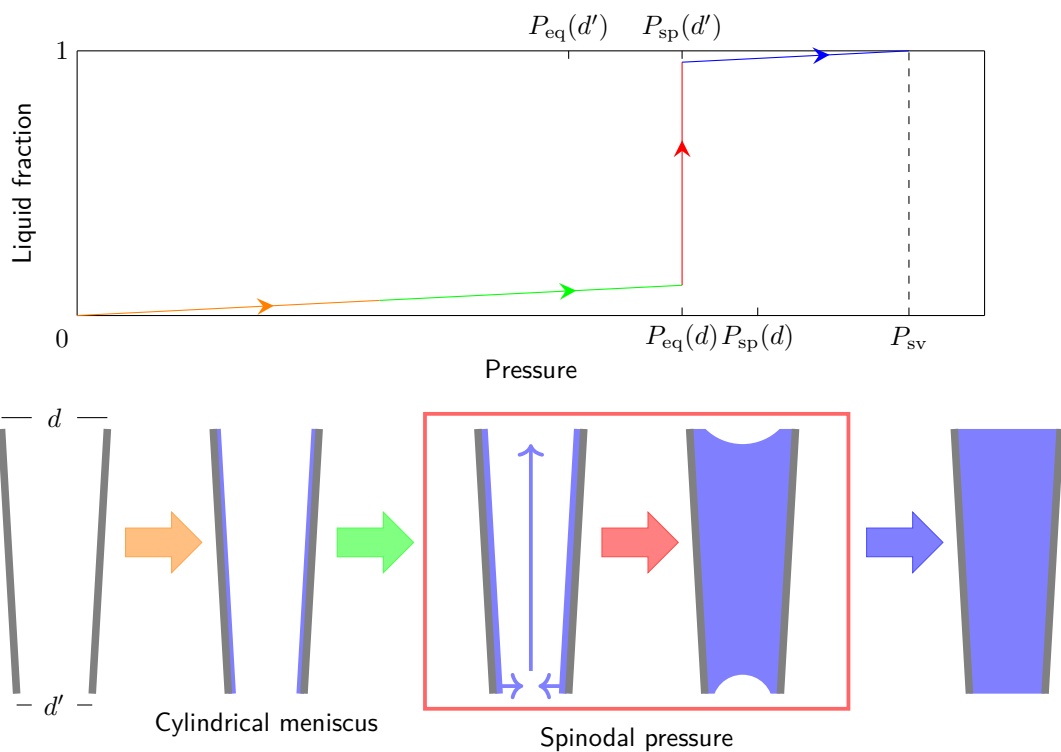


(a) Absorption isotherm. Significant is the absorption at spinodal pressure.

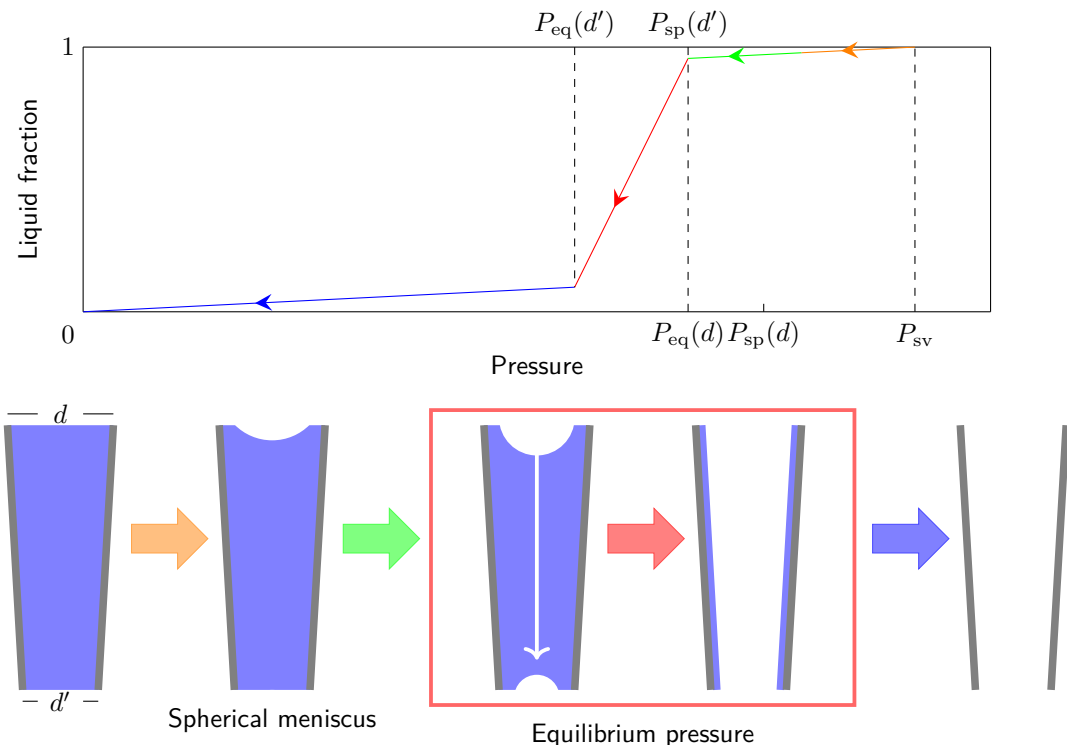


(b) Desorption isotherm. Significant is the desorption at equilibrium pressure.

Figure 2.5 Absorption (a) and desorption (b) isotherm of a straight cylindrical pore open on both ends. The corresponding processes inside the pore are illustrated below the isotherm itself. Colors of the arrows between pore states and the respecting pressure range of the graph match.

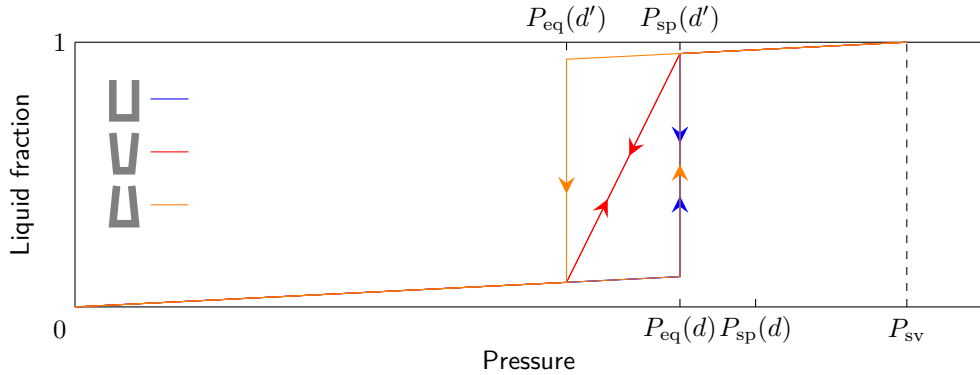


(a) Absorption isotherm. Significant is the absorption at spinodal pressure $P_{\text{sp}}(d') \geq P_{\text{eq}}(d)$.

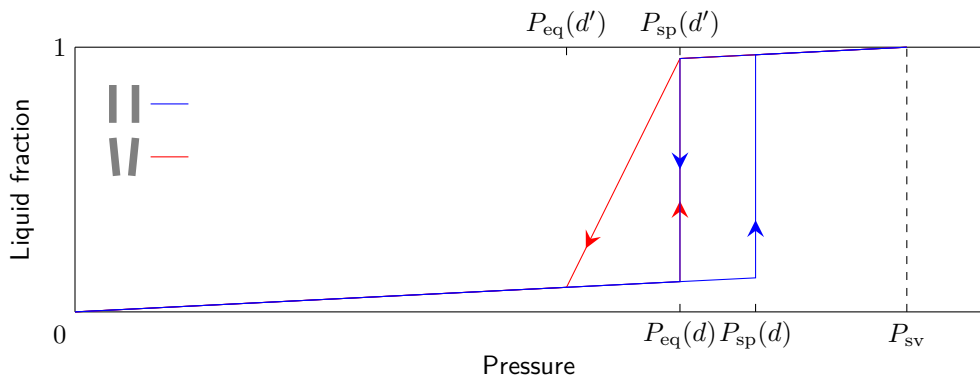


(b) Desorption isotherm. Significant is the continuous desorption at the equilibrium pressures $P_{\text{sp}}(d)$ to $P_{\text{sp}}(d')$.

Figure 2.6 Absorption (a) and desorption (b) isotherm of a funnelled cylindrical pore open on both ends. The corresponding processes inside the pore are illustrated below the isotherm itself. Colors of the arrows between pore states and the respecting pressure range of the graph match.



(a) Cylindrical pore open on one end.



(b) Cylindrical pore open on both ends.

Figure 2.7 Absorption and desorption isotherm loops for various kinds of cylindrical pores. For the funnelled pores it is $d > d'$.

2.6.3 Isotherm comparison

From the previous sections a resume as to which kind of pore yields which kind of absorption and desorption isotherm loop can be concluded. The loops for closed pores are shown in fig. 2.7 (a), those for closed pores in (b). Closed pores do not necessarily result in a hysteresis, open pores do so.

2.7 Snell's Law

The law of refraction by SNELL describes relation between the angles of incidence and refraction of an electromagnetic wave that passes from a medium with refractive index n_1 to a medium with the index n_2 . It is derived from FERMAT's principle, which implies that an electromagnetic wave traveling from point A to point B always takes the fastest path possible. Using the dependency of the speed of light on the index of refraction of a medium

$$v_i = \frac{c}{n_i}, \quad (2.16)$$

according to figure fig. 2.8, the wave takes the time

$$t = \frac{\sqrt{x^2 + a^2}}{v_1} + \frac{\sqrt{(l-x)^2 + b^2}}{v_2} \quad (2.17)$$

to travel from A to C . To find the shortest possible time depending on the parameter x , equation eq. (2.17) is derived and equated to zero yielding the SNELL's law

$$n_1 \sin(\alpha) = n_2 \sin(\beta). \quad (2.18)$$

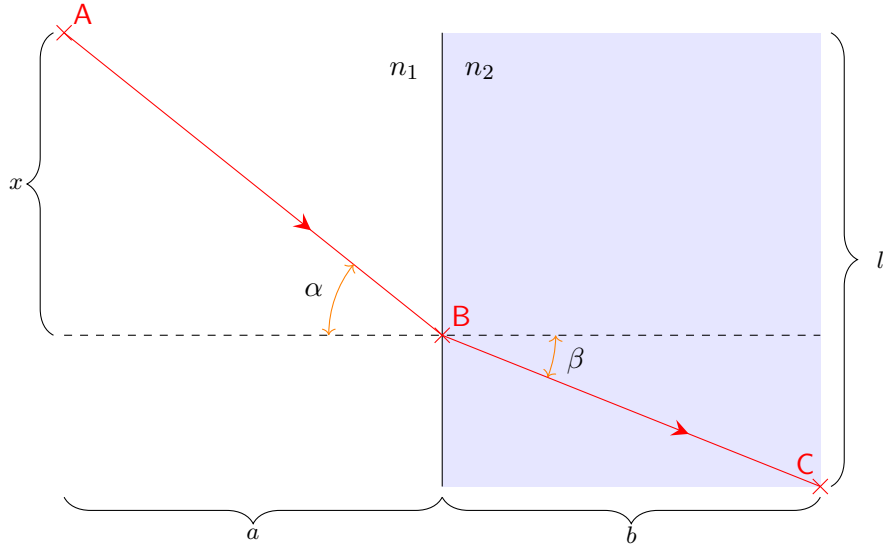


Figure 2.8 Visual derivation of SNELL's law.

2.8 Fresnel Equations

The FRESNEL equations describe the transmission and reflection coefficients of an electromagnetic wave passing from a medium with a refractive index n_1 to a medium with refractive index n_2 . They are derived from the MAXWELL equations and the SNELL's law as follows. An electromagnetic wave hitting an interface as described above is partially reflected and partially transmitted. The law of reflection yields the reflection angle

$$\theta_r = \theta_i, \quad (2.19)$$

where θ_i is the incident angle (compare figure fig. 2.9). Moreover, the transmitted part behaves according to SNELL's law resulting in the angle θ_t (section section 2.7). In the following, only o-polarized waves shall be regarded. The MAXWELL equations yield the electromagnetic boundary conditions

$$\begin{aligned} E_i \cos \theta_i + E_r \cos \theta_i &= E_t \cos \theta_t \\ H_i - H_r &= H_t. \end{aligned} \quad (2.20)$$

In words, the components of the magnetic field H_{\parallel} and the electric field E_{\parallel} are continuous. Using

$$\begin{aligned} H &= \sqrt{\frac{\epsilon}{\mu}} E \\ n &= c \sqrt{\epsilon \mu} \end{aligned} \quad (2.21)$$

to solve the equations eq. (2.20) yields the FRESNEL equations

$$\begin{aligned} r_p &= \frac{E_r^p}{E_i^p} = \frac{\frac{n_1}{\mu_1} \cos \theta_t - \frac{n_2}{\mu_2} \cos \theta_i}{\frac{n_1}{\mu_1} \cos \theta_t + \frac{n_2}{\mu_2} \cos \theta_i} \\ t_p &= \frac{E_t^p}{E_i^p} = \frac{2 \frac{n_1}{\mu_1} \cos \theta_t}{\frac{n_1}{\mu_1} \cos \theta_t + \frac{n_2}{\mu_2} \cos \theta_i}. \end{aligned} \quad (2.22)$$

Assuming non magnetic materials, in explanation

$$\mu_1 = \mu_2 \mu_0, \quad (2.23)$$

and using SNELL's law to simplify, eq. (2.22) becomes

$$\begin{aligned} r_p &= \frac{n_1 \cos \theta_t - n_2 \cos \theta_t}{n_1 \cos \theta_t + n_2 \cos \theta_t} \\ t_p &= \frac{2n_1 \cos \theta_i}{n_1 \cos \theta_t + n_2 \cos \theta_t}. \end{aligned} \quad (2.24)$$

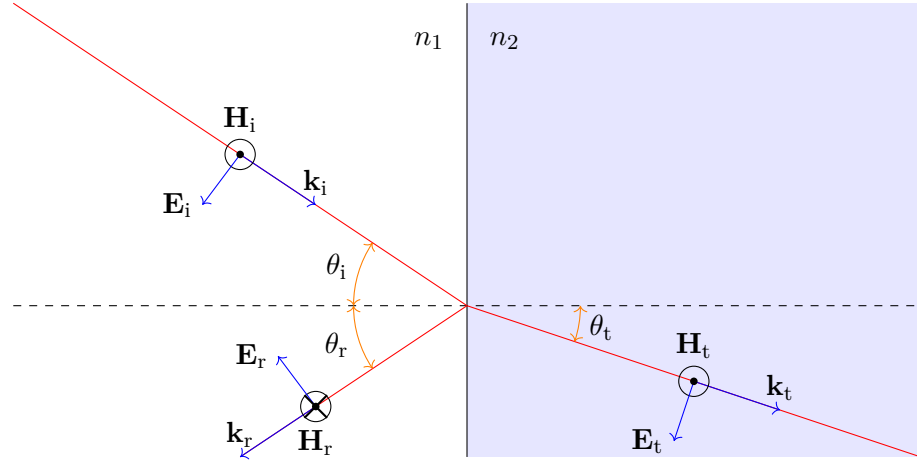


Figure 2.9 Sketch for the derivation of the FRESNEL equations. The index i stands for the incident wave, r for the reflected and t for the transmitted. The continuity of the components parallel to the n_1 - n_2 -interface is visualized. For the derivation please see 2.8.

2.8.1 Two Interface Transmission

In this section, the transmission of an electromagnetic wave through two media of increasing refractive indices

$$1 = n_1 < n_2 < n_3 \quad (2.25)$$

shall be compared to that a single interface transmission with

$$1 = n_1 < n_3. \quad (2.26)$$

Figure fig. 2.10 shows the two situations and defines the respective angles. To simplify the situation further

$$\alpha = 0 \quad (2.27)$$

shall be assumed as the incident angle. Hereby, the FRESNEL transmission coefficient eq. (2.24) becomes

$$t_p = \frac{2n_1}{n_1 + n_2} \quad (2.28)$$

as by SNELL's law eq. (2.27) makes for

$$\alpha = \beta = \gamma = \delta = 0. \quad (2.29)$$

Because more diffracting matter is added to the system, the two interface transmission is expected to yield a lower transmission than the single interface transmission, even though refractive index contrasts

$$\Delta n = n_i - n_j, \quad \{i, j\} \in \{1, 2, 3\}, \quad (2.30)$$

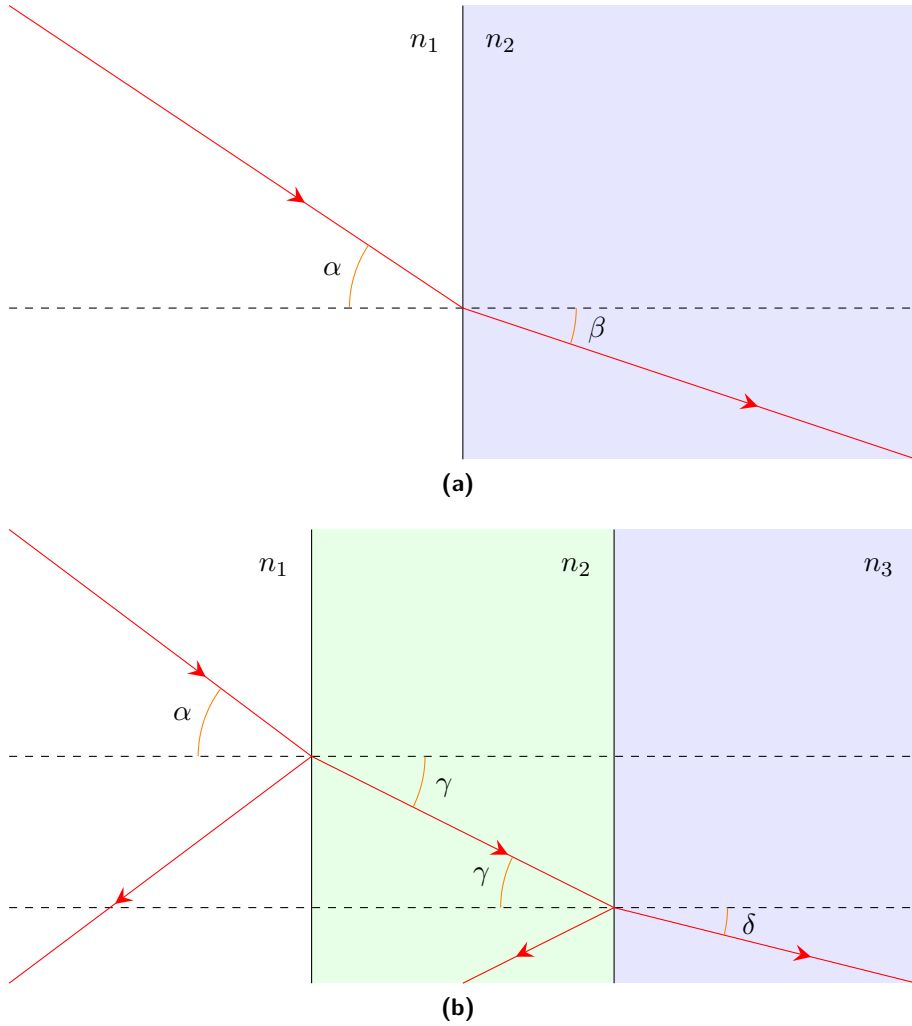


Figure 2.10 balblabla

are smaller. Therefore, the inequality

$$\begin{aligned} t_p^{13} &> t_p^{123} = t_p^{12} \cdot t_p^{23} \\ \frac{2n_1}{n_1 + n_3} &> \frac{2n_1}{n_1 + n_2} \cdot \frac{n_2}{n_2 + n_3} \end{aligned} \quad (2.31)$$

is regarded. With figure fig. 2.11 eq. (2.31) is solved graphically. The yielded result is that the transmission of the two interface transmission is indeed weaker than for the single interface assuming the inequality eq. (2.25).

2.9 Blablabla Näherung

The refractive index of a porous medium with structures in the range of the wavelength of the transmitting light can be approximated by the blablabla???. Using the porosity \$0 < \phi < 1\$ as a parameter it is assumed that the effective refractive index behaves like

$$n_{\text{eff}} = n_1 (1 - \phi) + n_2 \phi \quad (2.32)$$

where \$n_{1,2}\$ are the indices of the two components the medium is composed off (for nanoporous alumina membranes in empty state the components are alumina and vacuum for example).

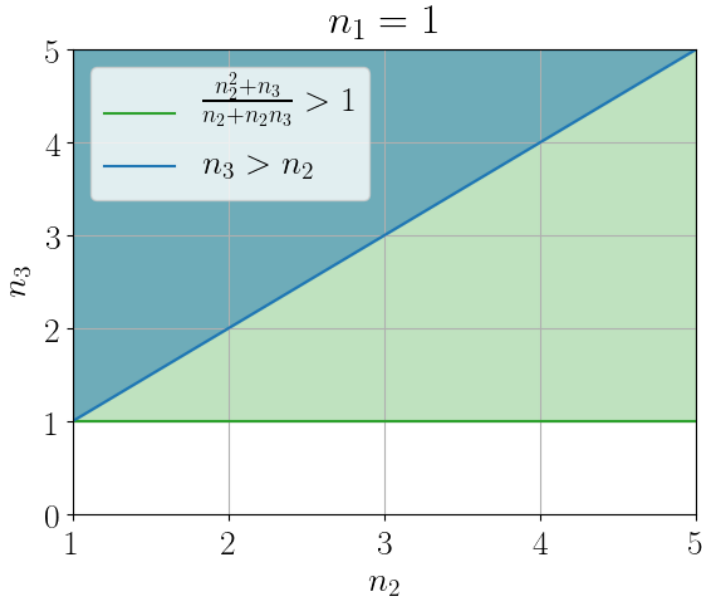


Figure 2.11 Graphical solution of the inequality eq. (2.31). While the blue shaded area also respects the inequality eq. (2.25), the orange shaded area shows the more general case $1 = n_1 < n_2, n_3$. Both cases yield a weaker transmission for the two interface transmission than for the single interface.

2.9.1 Transmission of Nanoporous Membranes in Empty and Filled State

Here, nanoporous media made of an arbitrary material with the sole condition that $n_{\text{mat}} > 1$ shall be regarded in empty and filled state. The wetting liquid's refractive index be $n_{\text{liq}} > 1$. The approximation eq. (2.32) yields the inequality

$$n_{\text{eff}}^{\text{empty}} = n_1 \cdot (1 - \phi) + n_{\text{vac}} \cdot \phi < n_1 (1 - \phi) + n_{\text{liq}} \phi = n_{\text{eff}}^{\text{filled}}, \quad (2.33)$$

where

$$1 = n_{\text{vac}} < n_{\text{liq}} \quad (2.34)$$

with the refractive index of vacuum n_{vac} . Referring to eq. (2.24) yields the transmission coefficients

$$T_{\text{empty}} = \left(\frac{2n_{\text{vac}}}{n_{\text{vac}} + n_{\text{eff}}^{\text{empty}}} \right)^2 \stackrel{\text{eq. (2.33)}}{>} \left(\frac{2n_{\text{vac}}}{n_{\text{vac}} + n_{\text{eff}}^{\text{filled}}} \right)^2 = T_{\text{filled}} \quad (2.35)$$

when assuming an incident angle $\theta_i = 0$ once again.

2.9.1.1 Transmission of Empty AAM Membrane

To give an example, the transmission coefficient of an empty nanoporous alumina membrane as used in the conducted experiments is computed in the following. The alumina membranes parameters are

$$\phi = 25 \% \quad (2.36)$$

$$n_{\text{Al}_2\text{O}_3} = 1,7682 \quad (2.37)$$

which make for a transmission coefficient of

$$T_{\text{Al}_2\text{O}_3}^{\text{empty}} = 0,9024. \quad (2.38)$$

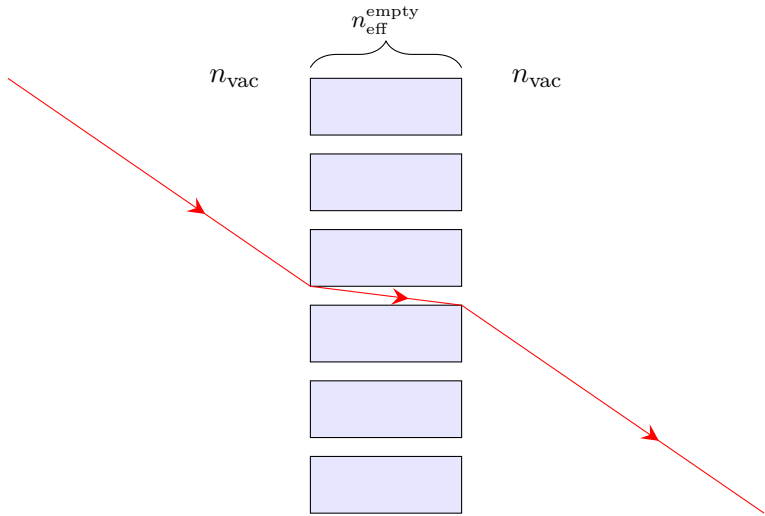


Figure 2.12 Using the blabla approximation for the refractive index of a nanoporous medium the transmission in its empty state is computed in section ???.

2.10 Rayleigh Scattering

2.11 Index Matching

3 Experimental

3.1 Alumina membranes

3.1.1 Membrane production

The alumina membrane production process starts with a circular wafer of amorphous aluminum of 99,999 % purity. With an initial thickness of $h_{\text{Al}} = 1 \text{ mm}$ and diameter of $d_{\text{wafer}} = 5 \text{ cm}$, one wafer is cut into twelve square membranes of side length $l_{\text{membrane}} = 1 \text{ cm}$.

First, the aluminum is anodized to create parallel pores that are arranged in a hexagonal order (compare section section 3.1.1.1). For the conducted experiment, pore lengths $l_{\text{pore}} = 30 \mu\text{m}$ and $60 \mu\text{m}$ are used. After the anodizing, the remaining aluminum of the wafer is dissolved by immersion in as specified in eq. (3.6) in section 3.1.1.2). Last, the so called *barrier layer* closing the pores on the bottom end is etched using oxalic acid (section section 3.1.1.3).

3.1.1.1 Anodizing

Figure 3.1 shows a sketch of the anodizing setup. The bulk aluminum wafer (compare fig. 3.2(a)), which functions as the anode, is glued to a copper plate using none conductive silver paste. Only one circular surface is exposed to the acid. The cathode is given by a platinum plate that is placed at a horizontal distance of 3 cm from the anode. The whole setup is immersed in oxalic acid that is stirred at all times. The anodizing of the wafers is conducted at a constant voltage $U_{\text{anodizing}}$. To produce parallel pores, the anodizing is carried out in two stages. Both use the same setup with the same parameters.

The pore diameter d_{pore} and the inter pore distance $d_{\text{interpore}}$ depends on the anodizing conditions, in explanation the voltage $U_{\text{anodizing}}$, the oxalic acid's molar concentration $n_{\text{C}_2\text{H}_2\text{O}_4}$ and the acid temperature $T_{\text{C}_2\text{H}_2\text{O}_4}$. Feasible are diameters of 10 nm to 100 nm. To produce wafers with the pore specifications

$$\begin{aligned} d_{\text{pore}} &= 40 \text{ nm}, \\ d_{\text{interpore}} &= 100 \text{ nm}, \end{aligned} \tag{3.1}$$

the parameters

$$\begin{aligned} U_{\text{anodizing}}^{40 \text{ nm}} &= 40 \text{ V}, \\ n_{\text{C}_2\text{H}_2\text{O}_4} &= 0,5 \frac{\text{mol}}{\text{l}}, \\ T_{\text{C}_2\text{H}_2\text{O}_4} &= 15^\circ\text{C} \end{aligned} \tag{3.2}$$

are used for the two anodizings. This makes for a growth rate of alumina of

$$r_{\text{Al}_2\text{O}_3} \approx 8 \frac{\mu\text{m}}{\text{s}}. \tag{3.3}$$

The first anodizing treats the raw bulk aluminum wafer. By the oxalic acid $\text{C}_2\text{H}_2\text{O}_4$, pathways are etched into the aluminum which follow no pattern at first. Only some of them continue to grow

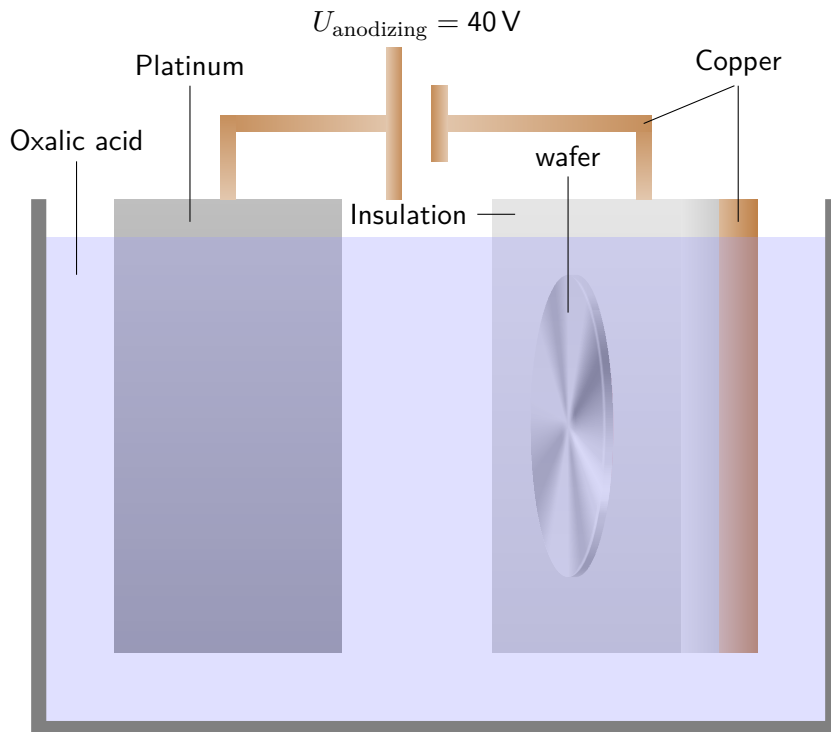


Figure 3.1 Setup for the anodizing of the membrane production. The aluminum wafer functions as anode while a platinum plate makes for the cathode. The oxalic acid is stirred during the whole process.

forming real pores, though. With the ongoing anodizing pores start to combine to form larger pores and finally areas of hexagonally arrange pores are created throughout the wafer. The longer the anodizing process is carried out, the larger these ordered areas become. Figure fig. 3.2(b) shows the cross-section of a wafer observable at this point. Because the process transforms aluminum to alumina (compare section ???) at a given penetration speed, the so called *barrier layer* of alumina separates the pores from the bulk aluminum.

Before the second anodizing, the wafer is immersed in a mixture of chromic and phosphoric acid with the concentrations

$$\begin{aligned} n_{\text{H}_3\text{PO}_4} &= 0,4 \frac{\text{mol}}{\text{l}} \\ n_{\text{C}_2\text{O}_3} &= 0,2 \frac{\text{mol}}{\text{l}} \end{aligned} \quad (3.4)$$

at a temperature of

$$T_{\text{C}_2\text{O}_3}^{\text{H}_3\text{PO}_4} = 0,2 \frac{\text{mol}}{\text{l}} \quad (3.5)$$

Hereby the created alumina is dissolved. This yields a slightly thinner wafer of bulk aluminum, where the thickness d'_{Al} depends on the time of the first anodizing. The relevant difference to the initial wafer are the areas of hexagonally arranged hollows (compare figure fig. 3.2(c)).

Due to this new surface structure, the second anodizing yields a wafer with a top layer of alumina penetrated by parallel, hexagonally arranged pores. Again, the *barrier layer* of alumina separates the pores from the bulk aluminum as illustrated in figure fig. 3.2(d). Increasing the time of the second anodizing increases the length of the pores l_{pore} and hereby the thickness of the final wafer. As the second anodizing is carried out under the same conditions as the first, the pore size d_{pore} is the same in both production steps.

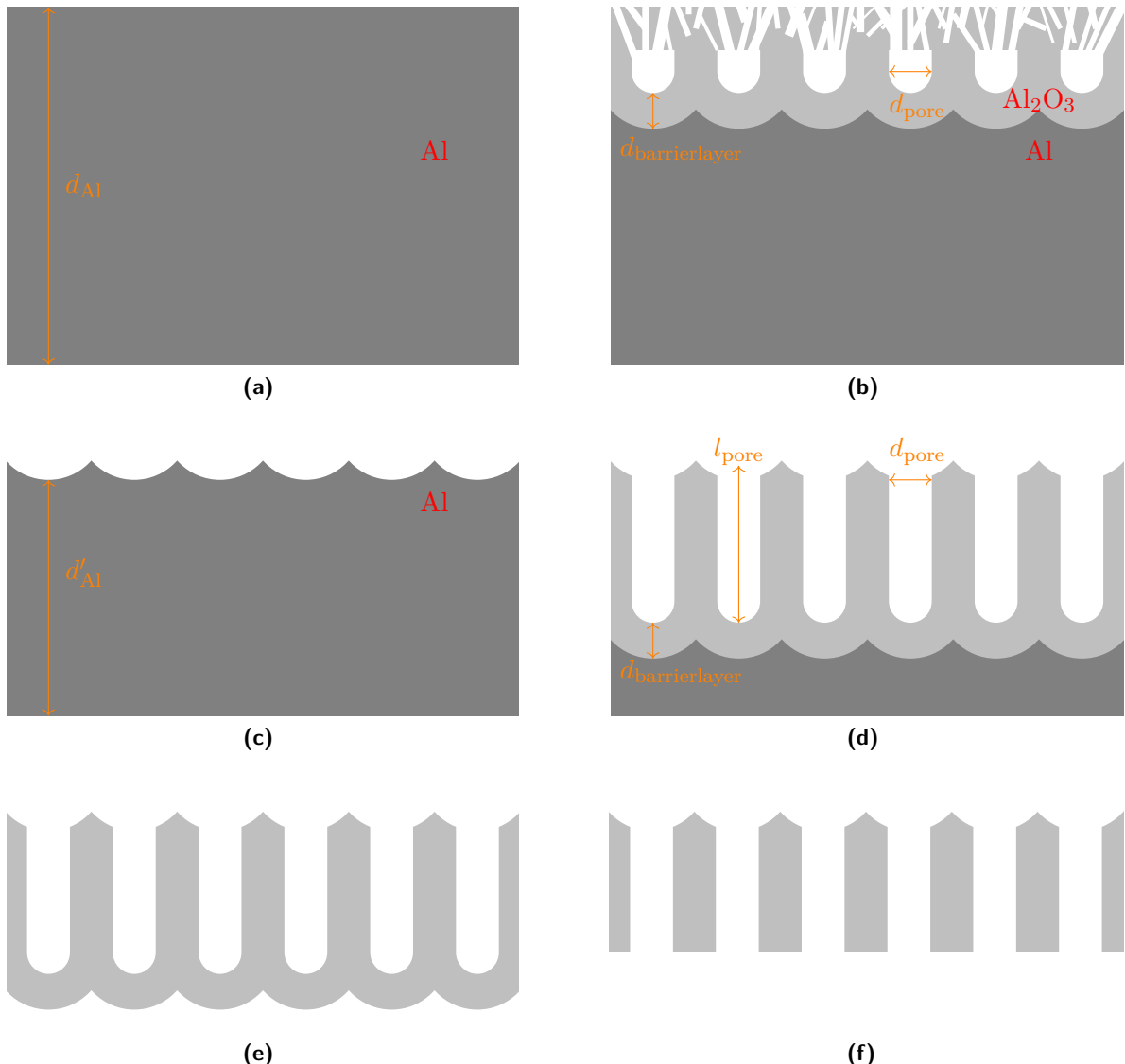
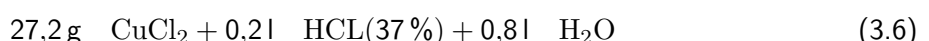


Figure 3.2 Production stages of the membrane production. It starts with a wafer of bulk aluminum (dark gray) (a) which is then anodized yielding (b), where light gray represents alumina. The latter is then dissolved producing a bulk aluminum wafer with hexagonally arranged hollows (c). By the second anodizing straight parallel pores are created (d). After dissolving the remaining aluminum (e) the barrier layer etched to open the pores (f). For the variable specifications please refer to section 3.1.1.

3.1.1.2 Aluminum dissolution

To dissolve the remaining aluminum on the bottom side of the wafer, it is immersed in an acid composed of



at a temperature of

$$T = 0^\circ\text{C} \quad (3.7)$$

as shown in figure fig. 3.3. The latter transforms the aluminum to copper in a very exothermic reaction (compare section ???). A lot of turbulences are created and thus this step limits either the thickness or the size of the wafers because it can easily break.

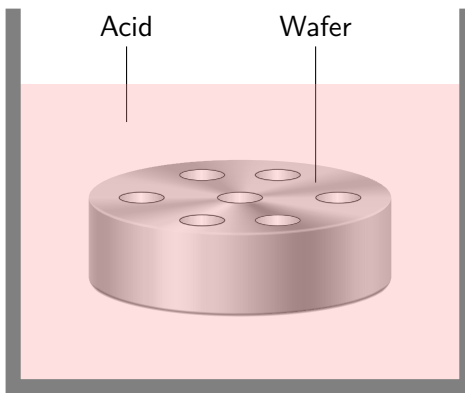


Figure 3.3 Setup for the aluminum dissolution step. The wafer is immersed in acid composed according to eq. (3.6) which dissolves aluminum according to section ???.

3.1.1.3 Barrier layer dissolution

The *barrier layer* dissolution is one step of the membrane production chain that is taken a closer look at in this report. The procedure is done using phosphoric acid of the concentration

$$n_{\text{H}_3\text{O}_4\text{P}} = 0,2 \frac{\text{mol}}{\text{l}}. \quad (3.8)$$

To dissolve the *barrier layer* and hereby open the pores, the wafers are floated on phosphoric acid as shown in figure fig. 3.4(a). Moreover, some membranes are immersed (compare fig. 3.4(b)) in the run of the experiments with the same aim of dissolving the *barrier layer*. If not explicitly mentioned though, the dissolution process has been conducted by floating for the respective membrane.

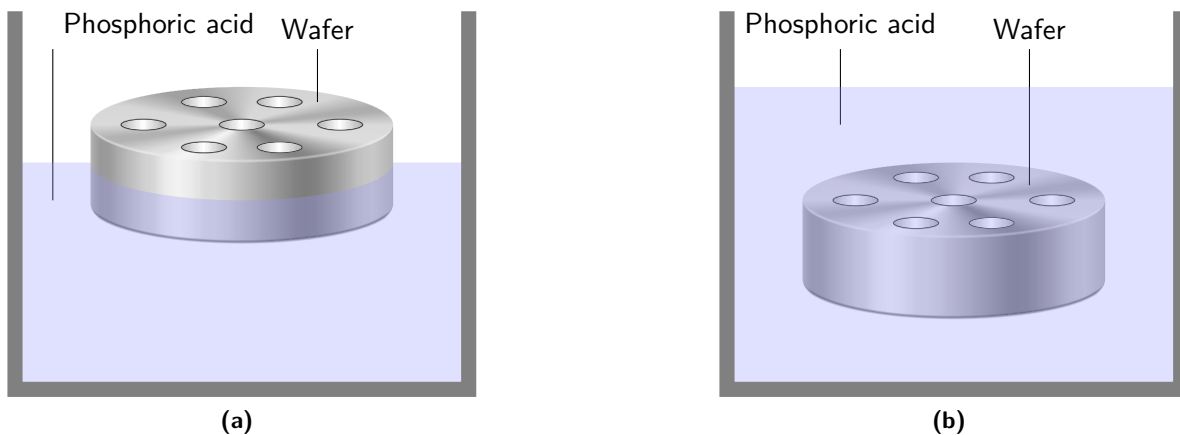


Figure 3.4 Setup for the *barrier layer* dissolution. The wafer is floated (a) or immersed (b) in phosphoric acid dissolving alumina according to section ????. For best results a combination of floating and immersing is used (please refer to section 3.1.1.3 for clarification of *best*).

3.1.2 Membrane specifications

For the experiments, square alumina membranes of DRAW A NICE IMAGE OF A MEMBRANE AND A PORE HERE???

3.2 Experimental setup

The experimental setup consists of two independent parts. To record isotherms, the core of the experiment is the volumetric measurement conducted in the setup explained in section 3.2.1. In addition to that, there are a light transmission setup and a camera setup that can be set up one at a time. Both setups are used to monitor what happens during the absorption and desorption isotherms using optics. While the camera setup provides for a visual interpretation of the occurrences, the data acquired by the light transmission measurement is used to measure the heterogeneities of the processes and put it in context with the volumetric isotherms.

3.2.1 Volumetric setup

The initial volumetric setup is sketched in fig. 3.5. A thermostatted bath by LAUDA functions as a reservoir of bulk hexane and is connected to the rest of the experiment via a valve. Behind the valve lies a cross leading to a pressure gauge P_{res} , via another valve to a primary pump (void), and via a PFEIFFER microvalve to the cell containing the sample membrane. This branch is also connected to a pressure gauge P_{cell} . The microvalve is the key part of the experiment as it allows for the extremely low flow rates that are necessary for the conducted experiment (section 3.3). Furthermore, the temperature of the cell and that of the thermostatted bath are monitored by the thermometers T_{cell} and T_{res} .

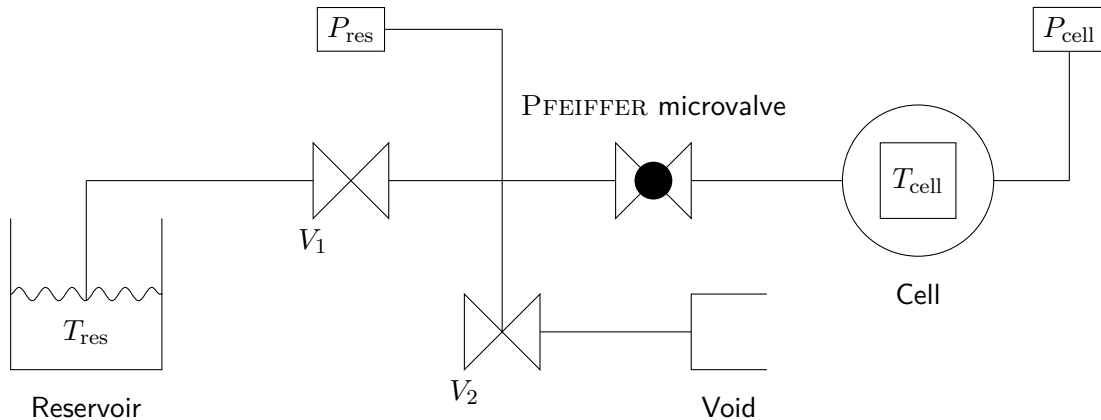


Figure 3.5 Experiment setup with bypass which allows to pump the whole system without changing the opening of the PFEIFFER microvalve. The temperatures within the reservoir and the cell are measured by the thermometers T_{res} and T_{cell} . Furthermore, P_{res} and P_{cell} are the two installed pressure gauges. The void is experimentally realized by a primary pump.

The whole experiment setup is placed in a climatized room set to

$$T_{\text{room}} = 23 \text{ }^{\circ}\text{C}. \quad (3.9)$$

The coldest point of the experiment must be the cell containing the sample membrane as to be sure no hexane condenses anywhere else in the setup. Therefore, the temperature of the cell is regulated to

$$T_{\text{cell}} = 19 \text{ }^{\circ}\text{C} \quad (3.10)$$

as explained in section 3.2.1.1 while the reservoir of bulk hexane is set to a temperature of

$$T_{\text{res}} = 21 \text{ }^{\circ}\text{C} \quad (3.11)$$

using the LAUDA.

3.2.1.1 Cell temperature regulation

The cell itself is made of a copper ring which is sealed on both sides using sapphire windows. Making use of indium O-rings, the windows are pressed onto the the copper ring by two aluminum rings. This circular cell is designed so it can be mounted to a second copper construction which is connected to a PELTIER heat pump and a heater. Moreover, two thermometers installed - one for the temperature regulation feedback loop and one for the output value. While the power of the PELTIER is fixed, the heater's power output is controlled by the feedback loop. From the microvalve to the pressure gauge P_{cell} , the setup is packed in styrofoam for thermal insulation from the room temperature and also to minimize the gradient inside this part of the setup. At first, the regulation has been run via a regular computer. As this led to breakdowns of the regulation for short periods of time multiple times per hour, the regulation was then externalized to an RASPBERRY PI. It regulates the temperature to $T_{\text{cell}} = 19,000(5)^\circ\text{C}$.

3.2.1.2 Pressure gauges

Because of its high resolution, at first, a KELLER S21 ??? pressure gauge was used for P_{cell} . As its construction contains a porous O'ring that could be identified as the source of degassing inside the system, the gauge has been swapped for a WIKA ??? which exposes only metallic parts to the system. P_{res} uses the same model of pressure gauge.

3.2.2 Laser transmission setup

The laser transmission setup is sketched out in fig. 3.6. In the path of the initial laser beam, a collimator and a diaphragm are placed before the cell. After being RAYLEIGH scattered by the membrane (please refer to ?? for explanations), the beam then passes another diaphragm and a collecting lens before hitting the photodiode.

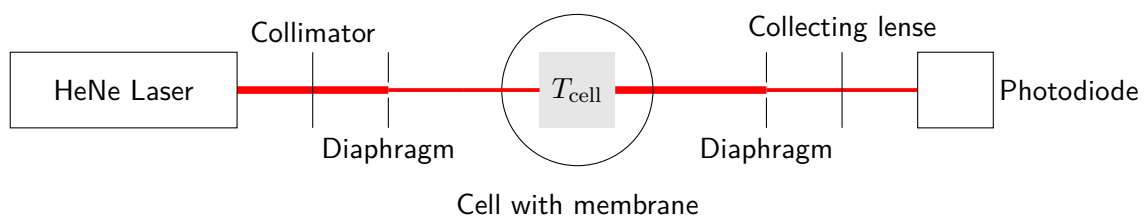


Figure 3.6 Sketch of the laser transmission setup.

3.2.3 Camera setup

To record images of the membranes during the absorption and desorption isotherms, a camera is installed and focused on the alumina membrane. A ???MODEL??? is used without any further optical instruments.

3.3 Experimental procedure

To start an experiment (here also referred to as an isotherm) the valve U_1 is closed while U_2 and the PFEIFFER microvalve U_{PV} are fully opened. This allows the primary pump, which experimentally realizes the void, to pump the system. As the condensation of hexane inside the sample starts at a pressure of about 150 mbar, it is not import to reach low pressures in this step. On the other hand

the pumping is used to clean the system of air which unavoidably enters the system when places the membrane inside the cell (or removing it from of the cell).

After pumping the system, U_2 is closed and the condensation process initialized by setting U_{PV} to a sufficiently low opening voltage and opening U_1 . Sufficiently low opening voltage shall imply that the condensation plateau of the condensation inside the membrane's pores is distinguishable on the recorded P over t isotherm. The employed flow rate's magnitude is $10^{-5} \frac{\text{mbar l}}{\text{s}}$.

To also record the bulk condensation plateau, which defines the saturated vapor pressure P_{sv} in the evaluation process, the setup is left condensing inside the cell for five hours after the pressure inside the cell reaches $P_{cell} = 150 \text{ mbar}$. This way a small amount of bulk liquid is condensed inside the cell. At the end of the process, all the valves are closed.

The evaporation process is then initialized by opening the valve U_2 . Meanwhile, the PFEIFFER microvalve is set to a sufficiently low opening voltage U_{PV} to permit the primary pump to pump the system. Again, sufficiently low implies that the evaporation plateau of the liquid evaporating from the membrane's pores is visible on the recorded P over t isotherm. The system is left in this state till the pressure inside the cell P_{cell} reached a given setpoint at which the microvalve is fully opened to pump the system and prepare for another isotherm.

3.3.1 Bypass

As the flow rate of hexane in the system only depends on the opening of the PFEIFFER microvalve and the pressures P_{res} and P_{cell} , this opening should always be the same to be able to compare multiple isotherms. Due to the uncertainty of the microvalve showing some hysteresis upon opening and closing, a bypass is added to the setup. As shown in fig. 3.7, the new setup allows to pump the part of the system containing the cell without changing the opening of the PFEIFFER microvalve now. This way there is no need to ever change the before mentioned opening and one potential error source is removed from the system.

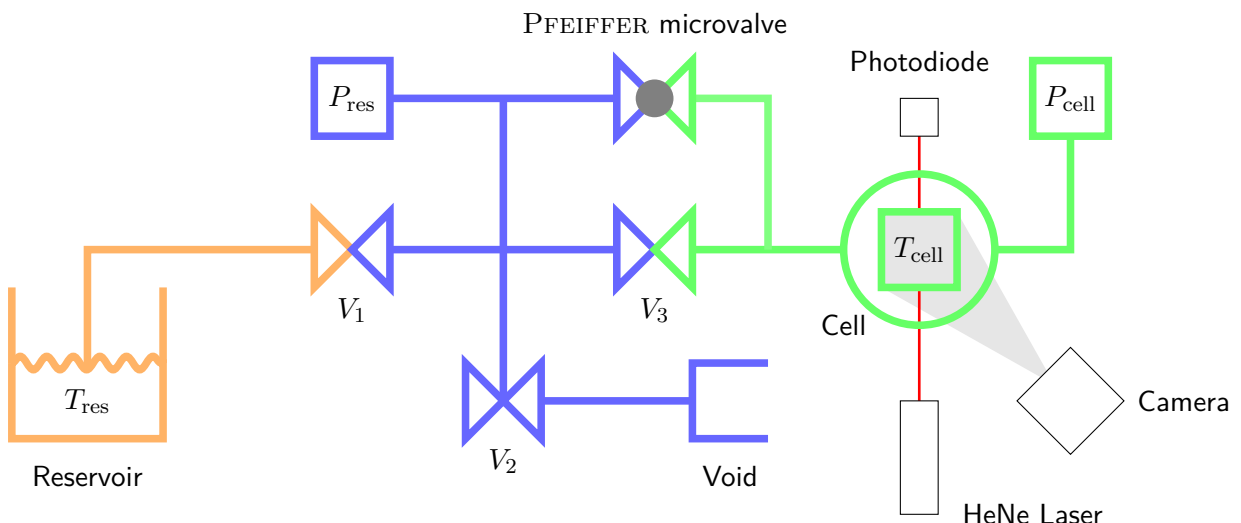


Figure 3.7 Experiment setup with bypass which allows to pump the whole system without changing the opening of the PFEIFFER microvalve. The temperatures within the reservoir and the cell are measure by the thermometers T_{res} and T_{cell} . Furthermore, P_{res} and P_{cell} are the two installed pressure gauges. The void is experimentally realized by a primary pump. Furthermore, the laser transmission setup and the camera setup are outlined. Only one of the two is set in place at the same time though.

The green volume of the system, which is the one of interest for the isotherm computation, is calibrated using the method explained in section section 2.2.1. Its volume is

$$V_{cell} = 8,27 \text{ cm.} \quad (3.12)$$

3.3.1.1 Changing the membrane

To change the sample, the copper cell must be opened and therefore detached from the rest of the system. After placing the membrane to be measured inside the cell, the latter is then reconnected to the system. As a result, the inside of the cell is at atmospheric pressure. Before the bypass was installed, to pump the cell, the PFEIFFER microvalve had to be opened. Using the small opening also used for the isotherms would have made for an unbearably long pumping process. For an approximation please refer to fig. 4.1(a) in ?? where hexane is pumped from the system. As the evaluation of the volumetric measurements depends strongly on the opening of the PFEIFFER microvalve which is not guaranteed to reopen without a hysteresis even if the same voltage as before is applied, the bypass has been installed to create a way to pump the system without touching the PFEIFFER's opening. From this point on, the contamination of the cell with degassing grease and the VCR connectors, that do leak to a certain degree are the most prominent hazards of the membrane changing process.

4 Analysis

4.1 Isotherm computation

In the following, evaluation of the recorded raw data is presented for volumetric (section 4.1.1) and for the optical measurements (section 4.1.2).

4.1.1 Volumetric isotherm

To compute the isotherms from the recorded data the experiment needs to be conducted not only with a membrane inside of the cell, but also with an empty cell. From here on, the following indices shall be used:

- 1 → no membrane
- 2 → membrane.

Furthermore, the variables P_i , \dot{P}_i , V_i , T_i , n_i and \dot{n}_i , $i \in \{1, 2\}$, refer to the values measured inside of the cell, in explanation the red marked part of the system in fig. 3.7. The raw isotherms of the two experiments are shown in fig. 4.1. The plateaus of the yellow curve with membrane inside the cell of the plot versus time correspond to the dips of the time derivative of the pressure of the versus pressure plot. This can be explained by the hexane condensing inside the membrane's pores at a given pressure due to which the continuing matter flow into the cell does not yield an increase of pressure.

Regarding the system with an empty cell, it is clear that the ideal gas law can be used to compute the flow rate of hexane (compare section 2.2). By solving for the amount of matter

$$n_1 = \frac{P_1 V_1}{R T_1},$$

taking into account that the temperature of the cell is regulated at T_1 and the volume V_1 is constant, the flow of matter becomes

$$\dot{n}_1 = \frac{V_1}{R T_1} \cdot \dot{P}_1.$$

Furthermore, the flow of matter for the system with a membrane inside the cell can be interpreted as the sum of the flow into the membrane \dot{n}_2^{mem} and the flow into the system volume excluding the membrane \dot{n}_2^{cell} . This can be rewritten yielding

$$\dot{n}_2^{\text{mem}} = \dot{n}_2 - \dot{n}_2^{\text{cell}},$$

where \dot{n}_2^{mem} obeys ideal gas law. Using the fact that the flow through the PFEIFFER valve only depends on the pressure difference $\Delta P_i = P_i^{\text{tank}} - P_i^{\text{cell}}$, assuming that $P_1^{\text{tank}} = P_2^{\text{tank}}$ leads to

$$\begin{aligned}\dot{n}_2^{\text{mem}}(P_2) &= \dot{n}_1(P_2) - \dot{n}_2^{\text{cell}}(P_2) \\ &= \frac{V_1}{R T_1} \cdot \dot{P}_1(P_2) - \frac{V_2}{R T_2} \cdot \dot{P}_2(P_2)\end{aligned}\tag{4.1}$$

Figure 4.2(a) shows the computation steps visually using the respective plots versus time.

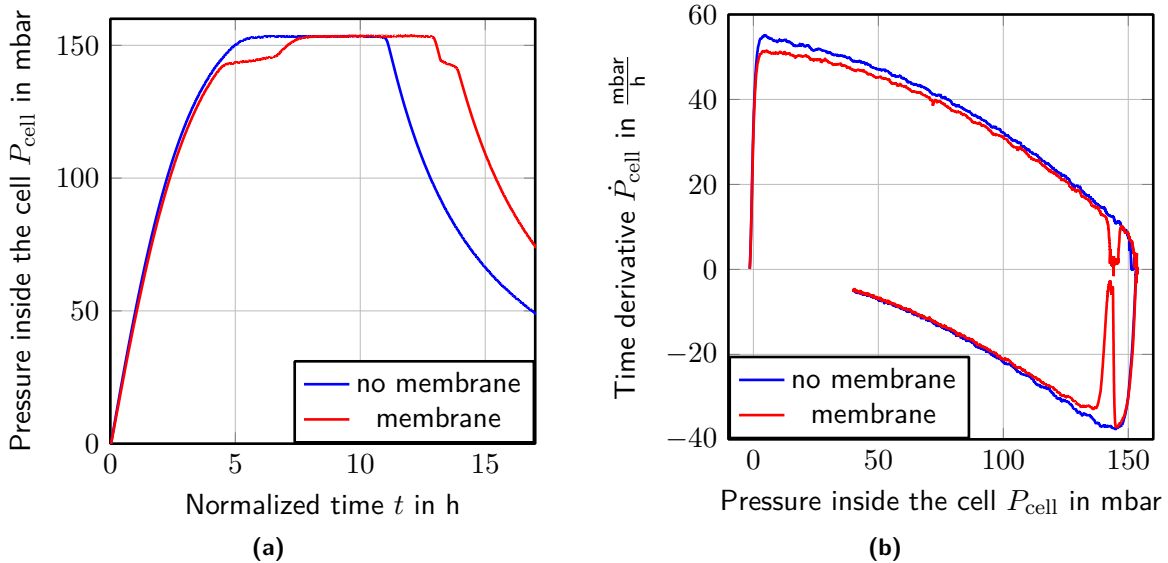


Figure 4.1 Raw volumetric isotherm data recorded with the experimental setup as explained in section 3.3 for one cycle without a membrane inside the cell and one with a membrane inside the cell. (a) shows the pressure values over time making the condensation and evaporation plateaus of absorption and desorption of hexane within the membrane's pores visible. (b) is the pressure loop which is relevant for the computation of the isotherms. Again, the before mentioned plateaus are visible as dips in the time derivative of the pressure.

As the temperature of the system is regulated ($T = T_1 = T_2 = \text{const.}$) and because $V = V_1 \approx V_2$ since $V_{\text{mem}} \ll V_1$, equation eq. (4.1) yields

$$n_2^{\text{membrane}} = \frac{V}{RT} \int_0^{t_2} (\dot{P}_1(t'_1) - \dot{P}_2(t'_2)) dt'_2. \quad (4.2)$$

Important at this point is the dependency of $\dot{P}_1(t_1)$ on t_1 while the integration is over t_2 .

As the experimental setup yields discrete values at given time intervals Δt , the data evaluation makes use of a sum rather than an integration.

$$n = \frac{V}{RT} \sum (\dot{P}_1(P_1 = P_2) - \dot{P}_2(P_2)) \cdot \Delta t \quad (4.3)$$

yields the molar amount of hexane condensed inside the membrane. Figure fig. 4.2(b) shows the result of the integration eq. (4.3) for membrane 296d. It is an absorption and desorption isotherm for hexane inside the porous alumina membrane. The bulk condensation and evaporation is not visible, as it is also recorded with the reference isotherm without membrane inside the cell.

What stings the eye is that the sharp rise of the condensation branch does not start at the liquid fraction $LF = 0$. The same goes for the evaporation branch. It only drops to a liquid fraction value $LF > 0$ and then decreases superimposed with the condensation branch. While it would be reasonable to renormalize the graph so only the mentioned sharp rise and drop are relevant for the isotherm as this part is where the pores fill or empty at spinodal or equilibrium pressure (section 2.6), it is not done here. The reason for this is that the initial rise of the isotherms is assumed to be due to the build up of a film on the membranes surfaces. This is part of the theory of condensation and evaporation in confinement even though the film is ignored in the basic KELVIN equation (section 2.5). ???MAKE A COMPUTATION AS TO HOW MANY MOLES OF LIQUID ARE EXPECTED FOR THE FILMS ON ONE SINGLE MEMBRANE???

Moreover, the plots

$$i \quad \text{over} \quad j, \quad i \in \{n, LF, FF\}, \quad j \in \{P_{\text{cell}}, P_{\text{rel}}, D_{\text{kelvin}}\} \quad (4.4)$$

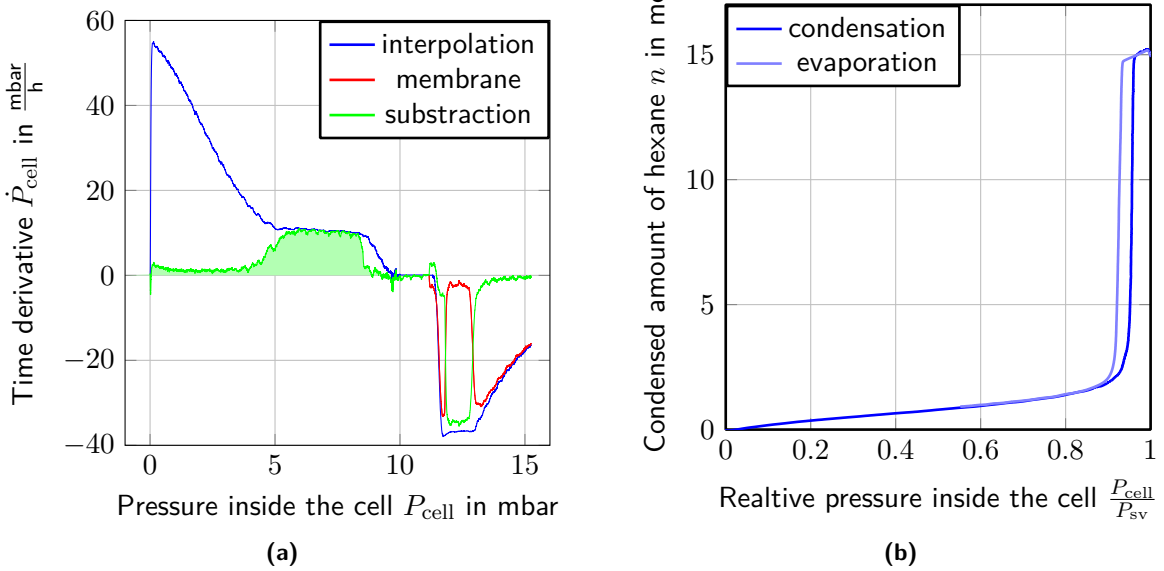


Figure 4.2 (a) shows the raw data of the isotherm with membrane and interpolation of the reference isotherm without membrane. Also, the subtraction of the latter (compare integrand of eq. (4.1)) is plotted where the area to be integrated for the absorption and desorption isotherm is shaded light green. The integration according to eq. (4.3) results in the isotherm displayed in (b).

are of interest, where

$$P_{\text{rel}} = \frac{P_{\text{cell}}}{P_{\text{sv}}^{\text{exp}}}, \quad (4.5)$$

with the saturated vapor pressure P_{sv} .

$$LF = \frac{n}{n_{\max}} \quad (4.6)$$

is the liquid fraction of hexane condensed inside the pores of the membrane using the total maximum amount of condensed hexane n_{\max} and last,

$$FF = \frac{V_{\text{hex}}^{\text{cond}}}{V_{\text{mem}}} \quad (4.7)$$

with the volume of condensed hexane $V_{\text{hex}}^{\text{cond}}$ and the membrane's volume V_{mem} , is the filled fraction of the membrane. Its maximum corresponds to the porosity of the membrane. For the computation please refer to ??.

For the computation of the introduced physical sizes, the saturated vapor pressure P_{sv} must be determined.

4.1.1.1 Porosity

Equation eq. (4.3) gives the molar amount of hexane n_{hex} condensed inside the membrane's pores. Furthermore, for the given pressures 0 mbar to 160 mbar hexane in its liquid form can be regarded as incompressible and therefore the hexane's volume be computed via

$$V_{\text{hex}} = n_{\text{hex}} \cdot V_{\text{mol,hex}}.$$

. The thickness l_{pore} of the membrane is easily determinable via MEB views since its magnitude is micrometers. Finally, the area A_{mem} of the measured samples is derived from a photo taken using binoculars.

Using these information the porosity ϕ of a given membrane is given by

$$\phi = 1 - \frac{V_{\text{hex}}}{V_{\text{mem}}}, \quad (4.8)$$

with the membrane's volume

$$V_{\text{mem}} = A_{\text{mem}} \cdot l_{\text{pore}}.$$

4.1.1.2 Determination of the saturated vapor pressure

As the bulk condensation plateau shows a slight drift (compare figure fig. 4.1), using the maximum measured pressure P_{cell} does not yield the saturated vapor pressure P_{sv} but a higher value. In addition, depending on the contamination of the system by air or degassing grease, the measured value for P_{sv} shifts due to the partial pressures. To probe the reproducibility of an isotherm loop including the grade of contamination, the node[anchor=south]maximum measured pressure for different membranes is compared. As the system is opened to replace the membrane in between the isotherms, each cycle is independent. For the change of membrane process please read section 3.3.1.1. The result of the experiment is that $P_{\text{sv}}^{\text{exp}}$ fluctuates by

$$\delta P_{\text{sv}}^{\text{exp}} = \pm 0,5 \text{ mbar}. \quad (4.9)$$

As the relevant plateau of condensation and evaporation inside the pores of the membrane occur at about

$$P_{\text{plateaus}} = 140 \text{ mbar}, \quad (4.10)$$

$\delta P_{\text{sv}}^{\text{exp}}$ translates to an error of about

$$\delta P_{\text{rel}} \leq \pm 0,005. \quad (4.11)$$

4.1.1.3 Diameter error using Kelvin equation

GAUSSIAN error propagation to check the precision of the experiment.

4.1.2 Optical measurements

As mentioned in section 3.2, the light transmission setup is independent from the volumetric measurements and also the evaluations do not depend on each other. The light transmission is rather a tool to check on the theory of evaporation and condensation within the membrane using a different approach.

To compute the transmission coefficient of a membrane, it is measured in dry state using the same transmission setup as during the volumetric experiment yielding $T_{\text{mem}}^{\text{dry}}$. Then, the first measured intensity value I_0 of a given isotherm is assigned to the dry coefficient as at this point no hexane is condensed inside of the membranes pores yet. From there on, each intensity measurement is translated to a transmission coefficient according to

$$T(t) = T_{\text{mem}}^{\text{dry}} \cdot \frac{I_0}{I(t)}. \quad (4.12)$$

The aquired physical size can be interpreted as explained in the following ??.

As a forword shall be mentioned that the observed transmission drops' magnitude cannot be explained by simple media transmissions as explained in section 2.8.1. Even counting multiple transitions for a diagonal transmission of a membrane, the regular transmission is not a sufficient explanation as the filled state of a membrane should by that theory be less transmitting than the empty state whereas the opposite is observed. To explain the phenomena, RAYLEIGH scattering and index matching, which are explained in section 2.10 and section 2.11 respectively, must be taken into account.

4.2 Conducted measurements

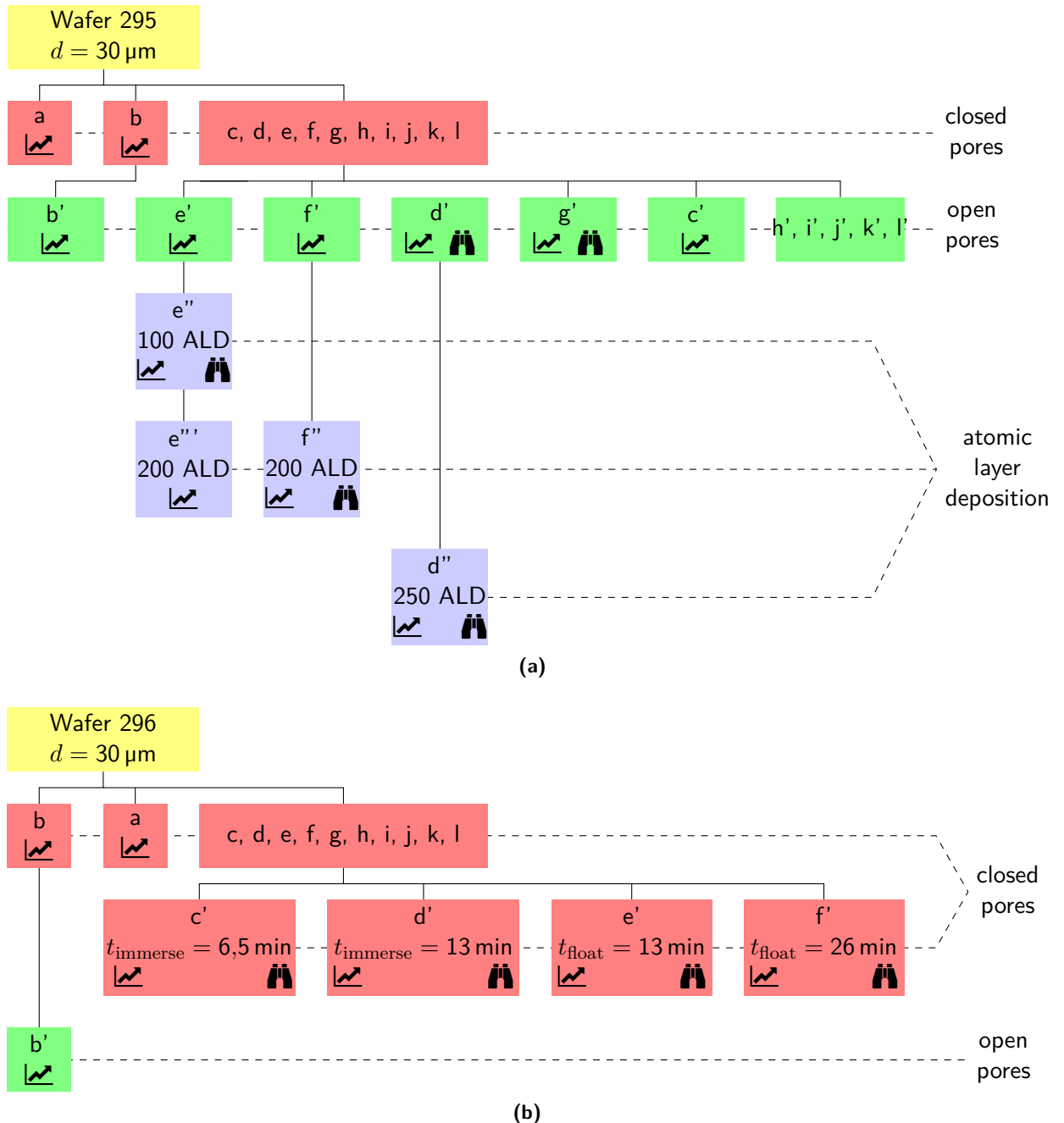


Figure 4.3 Wafer 295 and 296 processing scheme. While a signifies a recorded isotherm, the means MEB pictures have been taken. Red marks pores closed on one end, green pores open on both ends. The processed wafers are immersed in phosphoric acid for t_{immerse} or floated on for t_{float} .

General: From one wafer we can test different things as we have 12 membranes. Wafer produced as a whole so membranes should be equivalent. ADD THE CIRCLE HERE!!!

Membranes of four different wafers produced according to section 3.1.1 have been measured. Table 4.1 summarizes the specifications of the different wafers. As multiple membranes in the same state of the same wafer yielded different results, the position of the single membranes on the wafer were taken note for newly produced wafers. Therefore, for the wafers 295 and 296, the membranes' names correspond to the positions shown in fig. 4.4. Furthermore, all conducted measurements on the membranes in different states are noted on fig. 4.3.

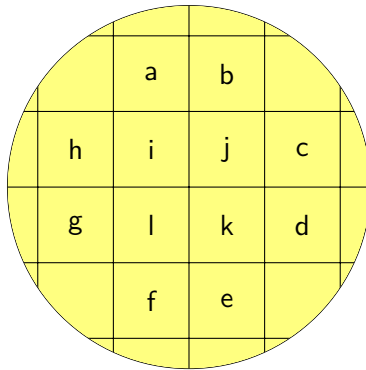


Figure 4.4 Convention used to assign membrane depending on their position on the wafer.

Table 4.1 Wafer specifications. The wafers thickness l_{pore} , floating time t_{float} of the barrier layer dissolution process and pore diameter dispersion $\Delta d_{\text{pore}}^{\text{MEB}}$ measured by electron beam microscopy are noted. The latter two parameters apply to the open pore membranes of the respective wafer.

Wafer	l_{pore} [μm]	t_{float} [min]	$\Delta d_{\text{pore}}^{\text{MEB}}$ [nm]
292	60	0	
294	60	0	
295	60	35	
296	30	40	7

4.3 Inhomogeneities on one wafer

To start with, the wafers shall be tested for inhomogeneities. Therefore, isotherms of one wafer's membranes which are in the same technical state, meaning they have undergone exactly the same treatments, are compared. This is done for both, closed pore membranes and open pore membranes. Because opening the membranes' pores involves one more production step, here, closed pore membranes are regarded first.

Figure 4.5 shows a comparison of closed pore membranes for wafer 295 and 296. Even though the membranes 296e' and 296f' had already been treated using phosphoric acid at the time of the measurements, the pores are still assumed to be closed as will be explained in section 4.4.

While for both wafers, with one exception being membrane 295c, the overall shape of the different membranes' volumetric isotherms matches, they are distributed along a short distance of the P_{rel} -axis. As long as the shapes and also the size of the hysteresis match, this can be explained by a differing pore size distribution for the different membranes. NEED DIAMETER CONVERSION FOR THIS??? Membrane 295c shall not be analysed at this point as it will be dealt with in detail in section 4.8. Moreover, also the transmission measurements yield optical signals of similar shapes. Unclear at this point is the variation in magnitude that can be extreme for some membranes as the example of 296f' compared to 296b shows.

4.4 Comparison of closed and open pores

Show comparison of 294, 295 and 296. Speak about the context to theory. Testing the efficiency of opening procedure. Theory test relies on the fact that pores are well open. ADD ONE THAT DID NOT WORK

Hysteresis for closed: corrugations

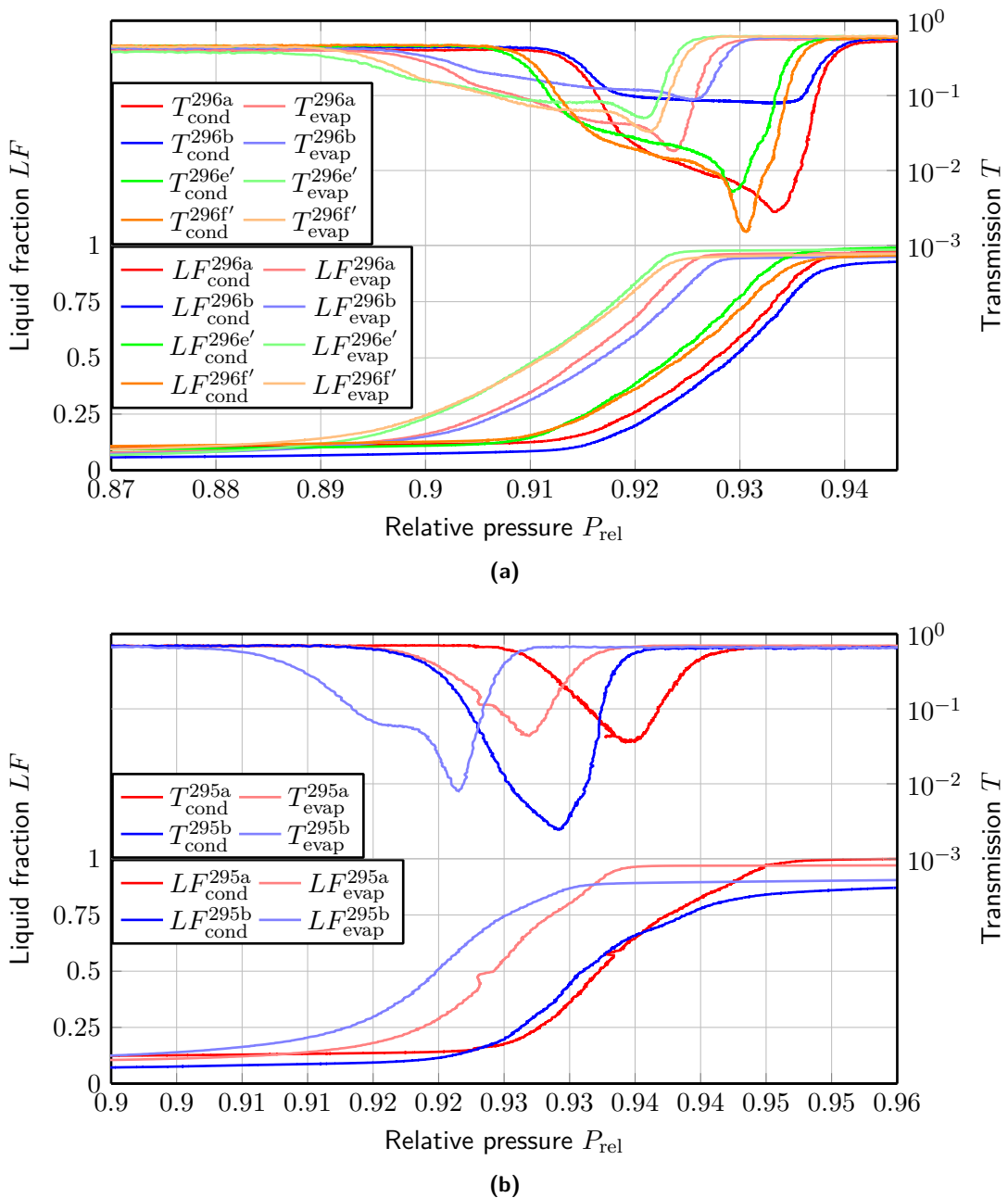


Figure 4.5 Comparison of closed pore membranes of one wafer. (a) compares membranes of wafer 296 while fig. 4.5(b) deals with 295.

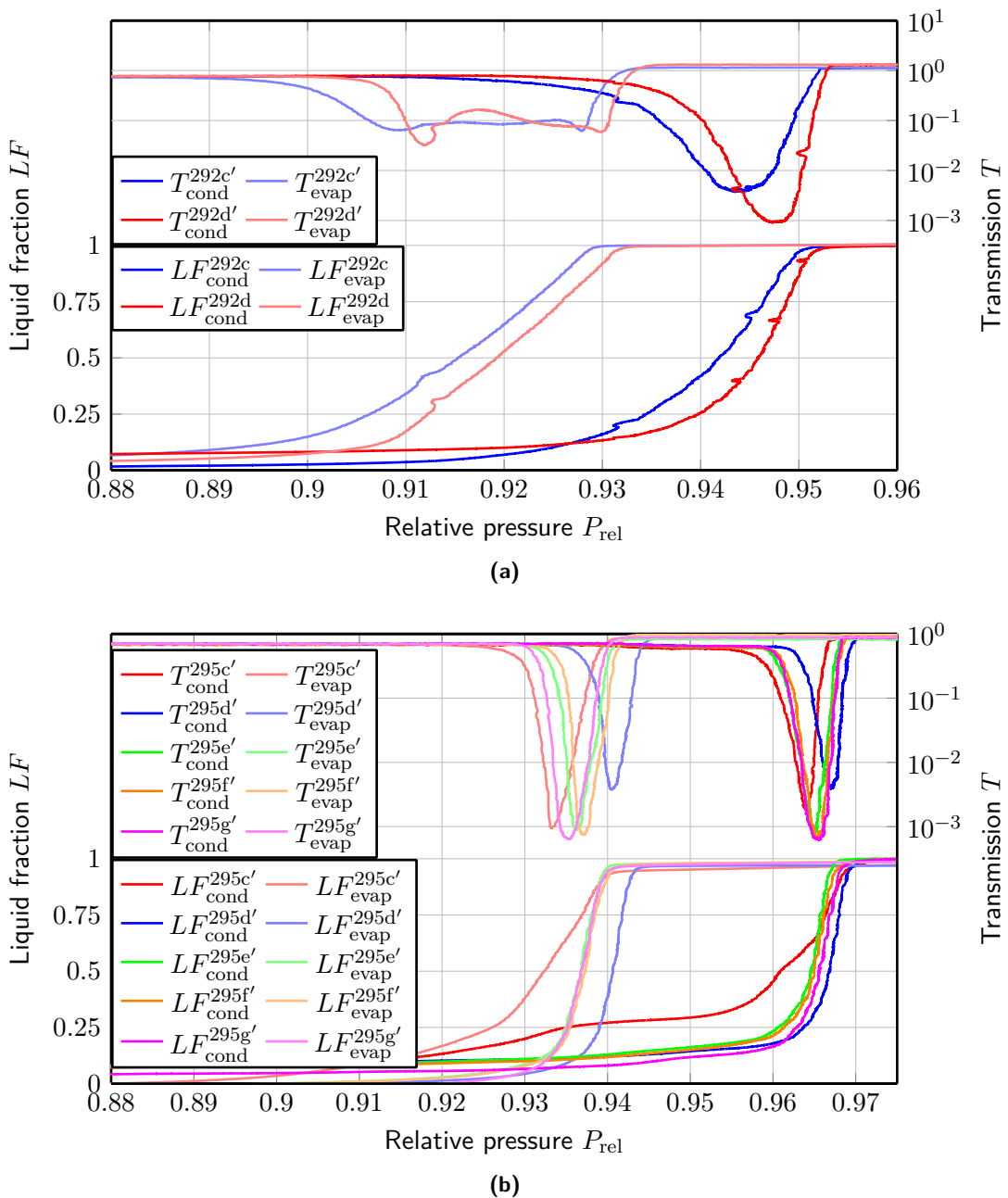


Figure 4.6 Comparison of open pore membranes of one wafer. (a) compares membranes of wafer 292 while fig. 4.6(b) deals with 295.

Hysteresis difference: Coherent with theory

This section shall serve to determine a systematic change of the isotherm by the *barrier layer* dissolution process which opens the pores on the bottom side. Moreover, the coherence with theory shall be regarded. Figure 4.7 shows the comparisons of closed pore and open pore membranes of the wafers 295 and 296. For both, closed and open pore measurements, the same membranes are used before and after the *barrier layer* dissolution to leave no doubt as to the inhomogeneities of the wafers.

Firstly, in reference to the model explained in section 2.6, the occurrence of a hysteresis for the volumetric isotherm of a closed pore membrane must be explained. The answer to that question has already been given by (???cite bruschi???:) It occurs due to intra pore corrugations. The modulation of the diameter along the pore's length corresponds to a varying equilibrium pressure. This makes for a non vertical isotherm.

Next, the difference between the isotherms for closed and open pores is regarded. Clearly, the size of the hysteresis increases. This tendency is coherent with theory as the latter predicts a hysteresis for open pores but as mentioned above, none for closed pores. Moreover, the evaporation branch of the open pore isotherm is shifted towards higher pressures as compared to the closed pore isotherm. That implies an increase of the pore diameter upon dissolving the *barrier layer*.

To prove that all the closed pore membranes of wafer 296, of which some have been treated using phosphoric acid, are indeed closed pore membranes, they are added to the graph of the membranes 296b and 296b' as shown in fig. 4.8. The comparison of the different membranes yields a significant difference of the hysteresis' size of 296b op and all other membranes, which show a much smaller hysteresis. As the size of the hysteresis for the rest of the membranes is approximately uniform and the variation of the condensation and evaporation pressures are only slightly shifted, this implies that indeed, all membranes except 296b op contain pores open only on one end. Which cannot be observed though, that is whether the pores already have microscopic openings on the barrier layer side. If that were the case, hexane would condense there at spinodal pressures lower than the equilibrium pressure of the small ends. Hereby, the pores would be left in a closed shape. This case would not be visible on the volumetric measurements as the condensed amount of hexane necessary to close the pores were so small. If the openings were so large already as for the spinodal pressure to be larger than the equilibrium pressure of the small end, in explanation

$$P_{\text{sp}}(d_{\text{pore}}) \leq P_{\text{eq}}(d_{\text{pore}}), \quad (4.13)$$

where d_{pore} is the small end's pore diameter, that case would be visible on the isotherm because whole pores would fill at higher pressures. Therefore, the latter case can be excluded.

4.4.1 Bad open pores

Talks about 294 and leads to

4.4.2 Inverse funnelling

What stings the eye of the attentive reader is that the evaporation branch also becomes more sharp for the open pores.

An explanation of the latter two phenomena can be taken from the production step of the *barrier layer* dissolution. As displayed in fig. 4.9(a), the wafer at some point becomes milky. Comparing these milky aspects to images taken during the condensation process of an isotherm as displayed in ??? leads to the conclusion, that at this point some of the pores start filling or are already filled with phosphoric acid. This phenomena lasting for a couple of minutes is followed by fifteen more minutes of floating until the wafer is completely covered by acid that flowed through the now open

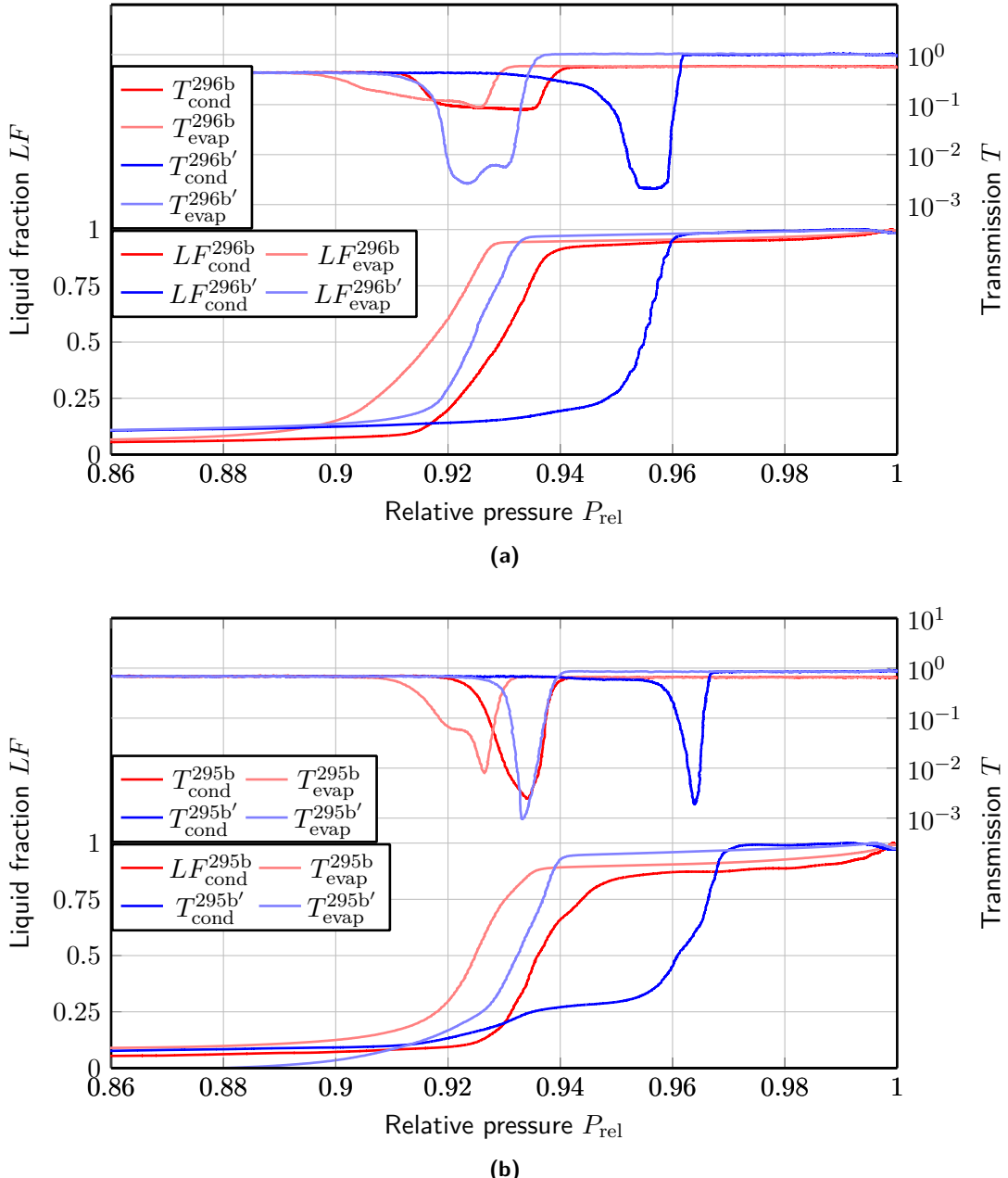


Figure 4.7 Comparison of the isotherms of membranes with closed pores to those with open pores. (a) shows membranes of wafer 296, while (b) displays those of wafer 295. The increase of size of the hysteresis is clearly observable.

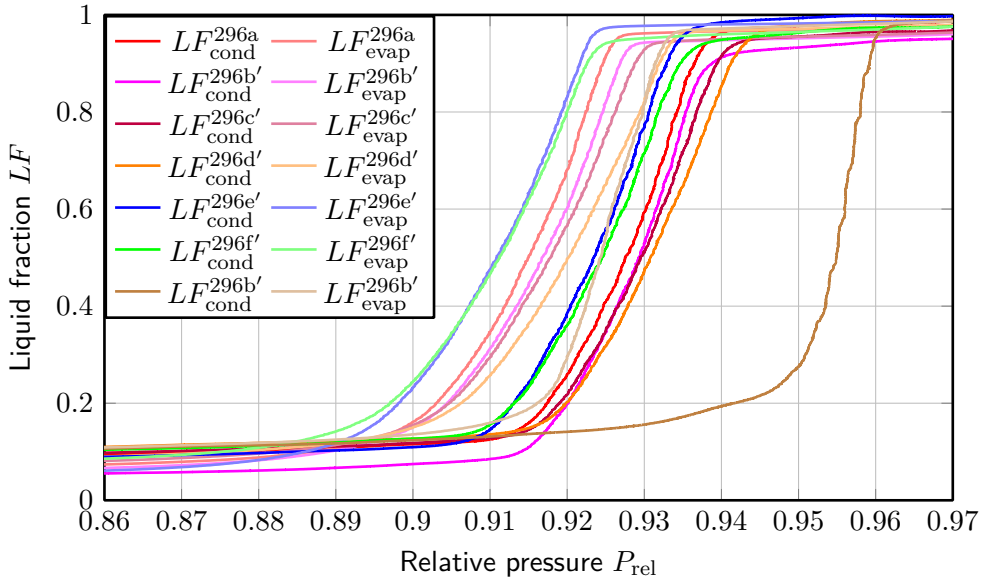


Figure 4.8 Full comparison of the closed pore membranes of wafer 296 with the open pore membrane 296b'.
For interpretation please refer to section 4.4.

pores (compare fig. 4.9(b)). That means during at least

$$t_{\text{filled}} = 15 \text{ min} \quad (4.14)$$

the pores are filled by phosphoric acid. That at the end of the process, the wafer is covered by a clearly visible layer of acid, means that there must be some flux of acid through the pores. On the other hand, taking into account the sharpening evaporation branch of the volumetric isotherms implies either a sharpening pore size distribution or a decrease of the funnelling or corrugation aspect of the pores.

By linking the occurring milky aspects to the filling of only some of the pores, meaning not all pores fill at the same time but over a span of

$$t_{\text{milky}} = 3 \text{ min}, \quad (4.15)$$

implies that the pore size distribution should rather be increased than decreased. Excluding this point only leaves corrugations and funnelling as explanations for the sharpening isotherms. As there is no reason to believe that an etching process could flatten a corrugated surface though, the straightening of the pores is more likely. Moreover, this inverse funnelling could be explained by the acid saturating along the axis of the pores. The theory of inverse funnelling is probed by experiments that will be analysed in section 4.4.2.

4.4.2.1 Funnelling of closed pores increased by immersion in phosphoric acid

Derive and explain etch rate gradient and influence on the pores' shape.

Understanding the inverse funnelling becomes one of the main goals of the experiments with wafer 296 as it might be used to correct the shapes of the pores of a given membrane. Therefore, immersion experiments where two closed pore membranes are immersed in phosphoric acid for

$$\begin{aligned} t_{\text{im}}^{296c'} &= 6.5 \text{ min}, \\ t_{\text{im}}^{296d'} &= 13 \text{ min}, \end{aligned} \quad (4.16)$$

and then the shapes of the volumetric isotherms compared to each other and addition with an untreated closed pore membrane. Focus lies on the shape of the isotherms. Small shifts in diameters

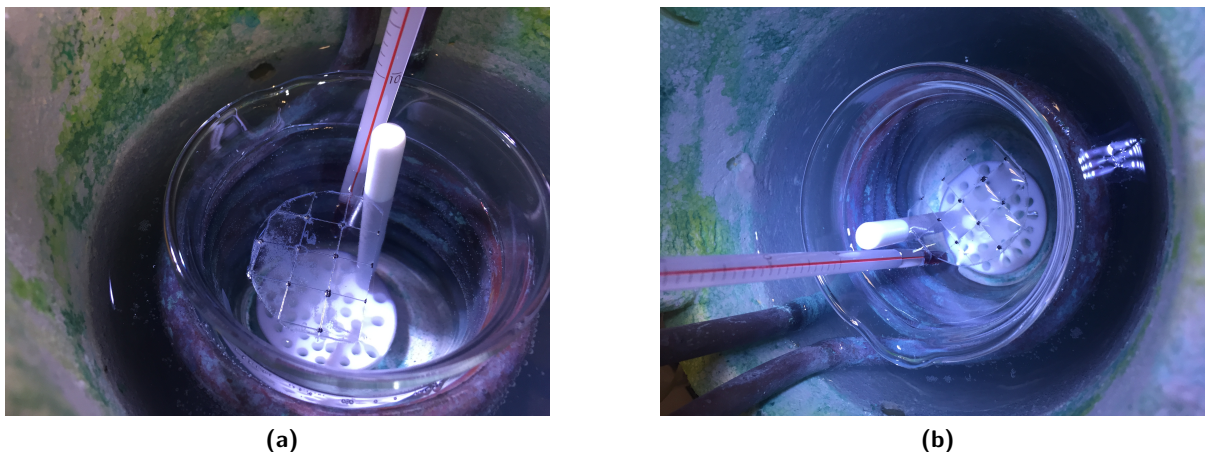


Figure 4.9 Images taken of wafer 295 during the *barrier layer* dissolution process. (a) shows milky aspects that appear after approximately twenty minutes while (b) has been taken just before removing the wafer from the acid. At this point the whole surface of the wafer is covered by phosphoric acid that passed through the pores.

Table 4.2 Diameter reduction per minute of immersion derived from the isotherms of the membranes 296a, 296c, 296d.

$t_{\text{im}}[\text{min}]$	$\Delta d_{h=60 \mu\text{m}}[\text{nm}]$	$\Delta d_{h=0 \mu\text{m}}[\text{nm}]$
0	0	0
6,5	3	0
13	6	0

are of no interest as the inhomogeneity of the pore size distributions of a wafer has been proven already in section 4.3.

Figure 4.10(a) compares the volumetric and also the transmission measurements of the immersed membranes 296c and 296d, again adding the untreated membrane 296a. As explained in section 2.6.1.2, condensation and evaporation in a closed funnelled pore occur at equilibrium pressure. Pores that are open on the large end start filling from the bottom and evaporating from the top so, regarding the isotherms in fig. 4.10(a), the lower end of the isotherm rising represents the small bottom end of the pores. This lower end of all three isotherms seems to be superimposed while the top end, representing the large open end of the pores, moves to larger diameters for longer immersion times. As the effect seems to occur linearly over the whole length of the pores, the acid seems to be saturating within the pores losing etching power. By section 2.6.1.2, the process can be visually interpreted as a pore straightening as shown in fig. 4.11(b). Moreover, the increase of the funnelling aspect seems to be linear at least within the first 13 minutes of the immersion as doubling the immersion time yields double the diameter shift on the volumetric isotherm (compare ??). For instance, table 4.2 shows the diameter increase of the pores due to the immersion of the membranes in phosphoric acid. Using this data along with the assumption of a linear etch rate gradient along the length of the pore, the respective etch rate can be plotted as shown in fig. 4.11(a). Here, the parameter h is used as the height within a vertical pore, where $h = 60 \mu\text{m}$ refers to the open top end of a $60 \mu\text{m}$ long pore that is closed on the bottom side. The effect, that reduces the funnelling aspect of the pores when floating the membranes on phosphoric acid as to dissolve the *barrier layer* shall be referred to as *inverse funnelling* from now on.

As for the transmission measurements, the shifts of the beginning of the condensation dip and also the end of the evaporation dips correspond to the interpretation explained above. Ob the other

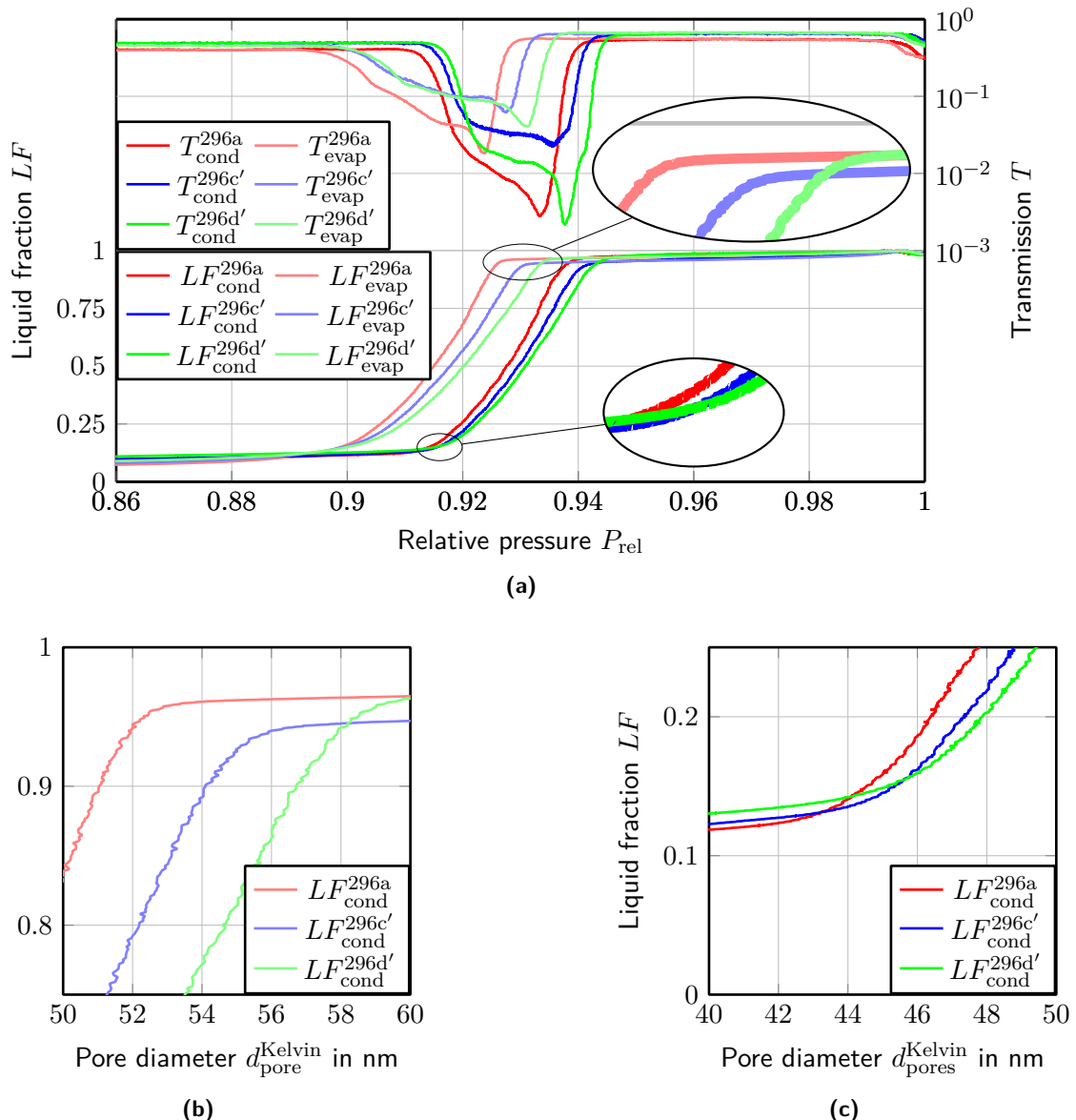


Figure 4.10 Membrane 296c' has been immersed in phosphoric acid for $t_{296c'} = 13$ min, 296d' for $t_{296d'} = 26$ min. (a) shows the isotherms of the immersion experiment conducted using wafer 296. The shift to larger pressures of the beginning of the evaporation branch and the unmoving beginning of the condensation branch are clearly visible. (b) and (c) are higher resolution plots of the relevant areas of the evaporation and respectively condensation branch of the isotherm on a pore diameter scale. For interpretations please refer to ???. ???EXPLAIN WHY EVAP START AND COND START ARE THE SPOTS TO LOOK AT ???

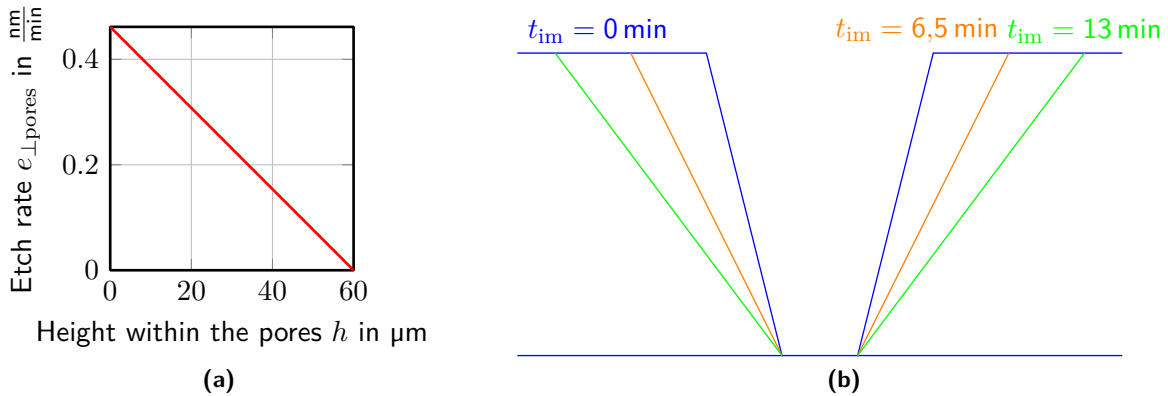


Figure 4.11 Immersion of a closed pore membrane resulting in an increase of the funnelling aspect of the pores as shown in (b) due to the saturation of the acid within the pores. The visualized theory is backed by the isotherms in fig. 4.10(a) which lead to the etch rate dependency plotted in (a) on the height within a pore. For further explanations please refer to ??.

hand, the magnitude difference of the three isotherms' dips cannot be explained, neither interpreted at this point.

4.4.2.2 Inverse funnelling upon barrier layer dissolution

Explain that the pores appear to be straightened bc of floating. Refer to the theory, that there are two sorts of alumina (pure and acid polluted).

With the conclusions reached in section 4.4.2.1, it is clear now that indeed, the *barrier layer* dissolution process reduces the funnelling of the pores. One more thing still does not fit into the great picture, though, which is that the kink of the volumetric isotherm of membrane 295b (compare ??) disappears upon pore opening. So far, the etch rate has been proven to show a gradient along the length of the pore, but a linear one which cannot account for this type of change in shape.

Therefore, a different explanation must exist to account for this change. cite the nice book here and explain the two sorts of alumina which are etched at different rates. Check if that can be true ith the thickness of that thing

4.4.3 Etch rate difference

4.4.3.1 Pore opening widening pores much less than expected

The thickness of the *barrier layer* of wafer 292 has been determined to be

$$d_{\text{barrier-layer}} = 30 \text{ nm} \quad (4.17)$$

by elecetron beam microscopy. After having been floated for

$$t_{\text{float}}^{292} = 20 \text{ min}, \quad (4.18)$$

milky aspects as shown in ?? appeared. As the latter are assumed to imply that the *barrier layer* is etched off the wafer, this makes for an etch rate of

$$e = 1,5 \frac{\text{nm}}{\text{min}}. \quad (4.19)$$

This result is drastically different from the etch rate computed in section 4.4.2.1 and thus raises questions regarding the etch rate of phosphoric acid on alumina.

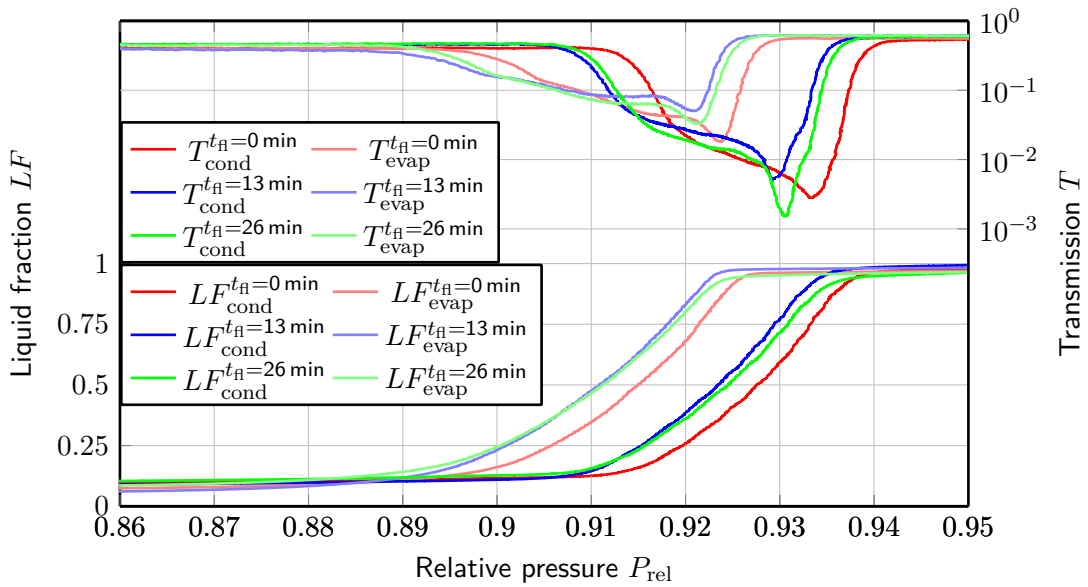


Figure 4.12 Comparison of the isotherms measured for the membranes 296a, 296e' and 296f'. While the pore diameters are marginally smaller for the membranes 296e' and 296f' than they are for 296a, the overall picture is equivalent. It makes for closed pores (or constricted open pores as explained in section 4.4) with the same funnelling aspect.

Using the result eq. (4.19) for further calculations yields a theoretical pore diameter increase of

$$\Delta d_{\text{pore}} = 22.5 \text{ nm} \quad (4.20)$$

during the fifteen minutes etching of filled pores when disregarding the acid saturation within the pores. Nevertheless, even regarding the saturation, the bottom end of the pores that is exposed to the bulk acid reservoir should be widened dramatically which is not observed on either electron beam microscopy images nor the volumetric measurements. Further analysis on the difference of the etch rate parallel to the pore axis e_{\parallel} and perpendicular to the axis e_{perp} follows in section 4.4.3.

As a way to not increase the distribution of pore diameters on a given wafer, the idea of floating the wafer on acid for a time just short enough to not open any pores, followed by its full immersion in acid has been developed. As to not increase the pores diameter by too much regardless of the acids saturation, the immediate immersion of the whole wafer without prefloating discarded. Again, the acid's etch rate on the *barrier layer* is a prerequisite and shall be deduced in section 4.4.3.

4.4.3.2 Etch rate of phosphoric acid on alumina not clear

Explain that the shapes of the isotherms are correct, but that no real conclusion could be made due to the bad MEB views.

In order to calibrate the etch rate on the *barrier layer* of a give wafer and to try to reduce its thickness in order to immerse the wafer after for the final pore opening, two membranes are floated on phosphoric acid for

$$\begin{aligned} t_{\text{fl}}^{296e} &= 13 \text{ min}, \\ t_{\text{fl}}^{296f} &= 26 \text{ min}. \end{aligned} \quad (4.21)$$

After, measurements are conducted and the results compared to membrane 296a, which is an untreated membrane in closed pore state, for a reference (fig. 4.12). While a slight shift in diameter between the floated membranes and the untreated one is visible, this is assumed not to be due to the treatments but rather due to the inhomogeneity of a given wafer. Moreover, the shapes of the isotherm do not show any significant slopewise deviation. Still, as explained before, the membranes

could include pores badly open on the *barrier layer* side. Anyways, to probe the thickness of the *barrier layer*, electron beam microscopy is used and along with the cross section, the two sides of the membranes are imaged. Due to the drift that could not be resolve, the attempt to measure the thickness of the *barrier layer* did not work out well as can be seen on fig. 4.13(a). On the other hand, the views of the aluminum side of 295e' (fig. 4.13(b)) confirm that the pores of the membrane remain closed on the bottom side.

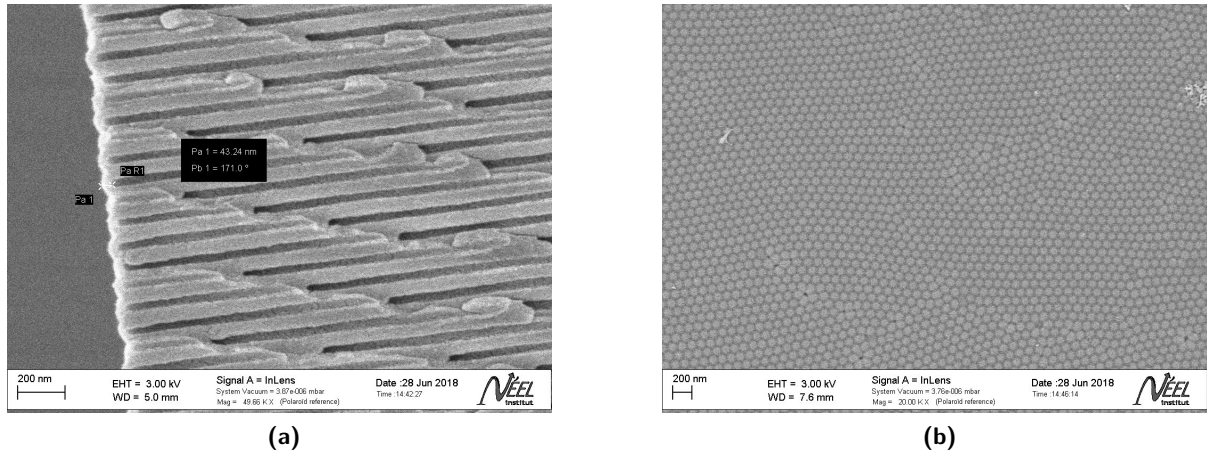


Figure 4.13 Electron beam microscopy images of membrane 296e' that has been floated on acid for $t_{\text{fl}} = 13 \text{ min}$. (a) shows the cross section view with the attempt to measure the thickness of the membrane's *barrier layer*, while (b) is the aluminum side on which the membrane has been floated on.

4.4.4 Do thinner membranes improve things?

Compare 295 and 296. Talk about the sharpness of both, the volumetric and the optical isotherm. Also speak about the rather broad isotherm for closed pores of 295 which is not understood. Use diameter translation by Kelvin law!!

Wafer 295 is only

$$l_{\text{pore}}^{295} = 30 \mu\text{m} \quad (4.22)$$

thick. Hereby, the effect of the funnelling observed upon the previously measured membranes of a thickness of

$$l_{\text{pore}}^{292,293,294,296} = 60 \mu\text{m} \quad (4.23)$$

is expected to be reduced. Assuming that the funneling aspect is linear implies a reduction of the effect by half which should lead to a sharper evaporation branch.

?? shows the comparison of the membranes 295a and 296b on a KELVIN diameter axis. Both membranes' pores are closed by the *barrier layer* on the bottom side. In contrast to expectations, the evaporation branches show a similar spread

$$\begin{aligned} \Delta d_{\text{evap}}^{295a} &= 15 \text{ nm} \\ \Delta d_{\text{evap}}^{296b} &= 17 \text{ nm}. \end{aligned} \quad (4.24)$$

To determine the latter, the volumetric isotherms' rise and also the transmission drops have been regarded. At this point, assuming some uncertainty also due to the slightly different values derivable from optics and volumetrics, the funneling aspect seems unchanged by moving to thinner membranes. But, looking at the condensation branches of the volumetric isotherms could bring clarity. While the condensation branch of membrane 296b shows approximately the same slope and shape as its evaporation branch, for membrane 295a this is not true. The latter membrane's condensation branch

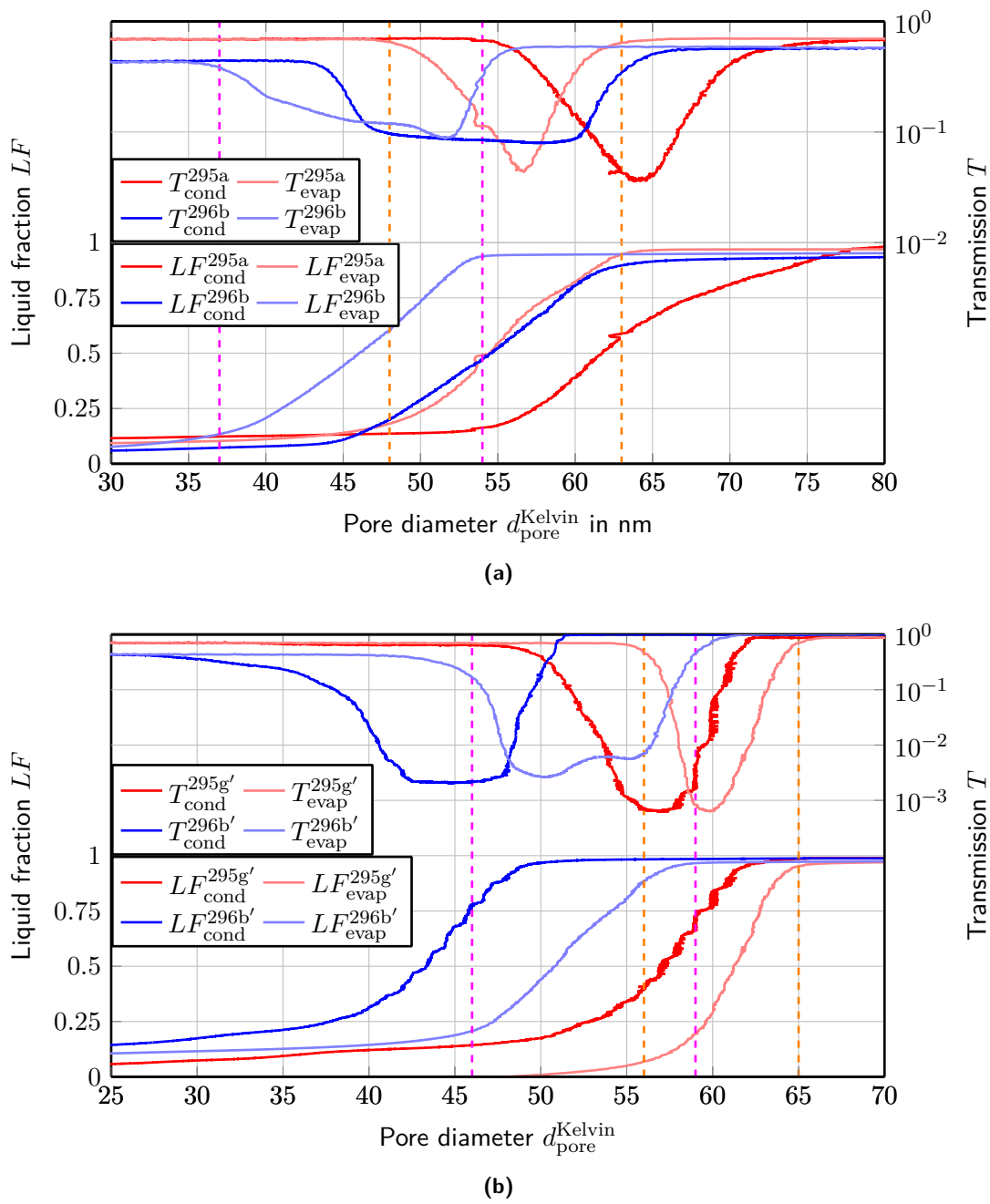


Figure 4.14

spreads out over about 25 nm so it is much broader than its evaporation branch. This can only be explained by severe corrugations within the pores as straight funnelling should not cause any differences in shape between the condensation and evaporation branches according to section 2.6. The transmission signals match in magnitude for both membranes while it is much sharper for the thinner one. As a first guess, this could be interpreted as a sign more less flawed or even less corrugated pores, though that would contradict the before made analysis. In conclusion, from the closed pore isotherms no conclusion can be drawn as to how the funnelling aspect is affected by reducing the membrane thickness.

Figure 4.14(b) then shows the isotherm comparison of the open pore membranes 295g' and 296b'. For these isotherms, the condensation does match the evaporation branch shapewise. The spread of the evaporation is

$$\begin{aligned}\Delta d_{\text{evap}}^{295g'} &= 9 \text{ nm} \\ \Delta d_{\text{evap}}^{296b'} &= 13 \text{ nm.}\end{aligned}\quad (4.25)$$

Again, the transmission drops for the thirty micrometer membrane 295g' are more sharp but within the same magnitude as those of 296b'. A difference in funnelling seems more probable from this measurement even though, the bottom line is that no precise conclusion can be drawn from the measurements at this point.

For more clarity, electron beam microscopy is used to check the difference of the diameters on solution and aluminum side. Figure 4.15 shows the images for the membranes 295g' and 296b' which state a diameter offset of about

$$\begin{aligned}\Delta d_{\text{sem}}^{295g'} &= 6 \text{ nm,} \\ \Delta d_{\text{sem}}^{296b'} &= 6 \text{ nm.}\end{aligned}\quad (4.26)$$

So the SEM images show the same tendency as the volumetric and optical measurements.

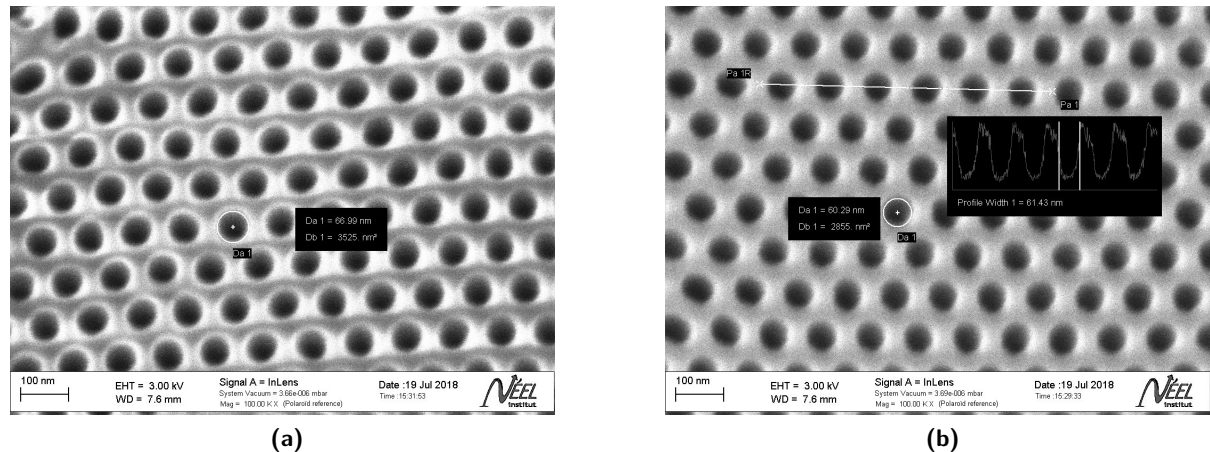


Figure 4.15 Electron beam microscopy images of membrane 295g' with measurements of the pore diameters on the solution side (a) and aluminum side (b).

To conclude with, even though the effect is not as significant as expected, thinner membranes indeed do improve the pore quality.

4.4.5 Transmission signal not well understood

To begin with it must be mentioned here, that all open pore membranes measured before the wafers 295 and 296 have shown the same transmission characteristics in regard of the significant magnitude difference of the condensation and evaporation isotherm branch which can be seen on ???. Therefore,

a theory to explain this phenomenon were developed. The prominent one at the beginning of the conducted experiments mentioned in this report shall be explained in the following.

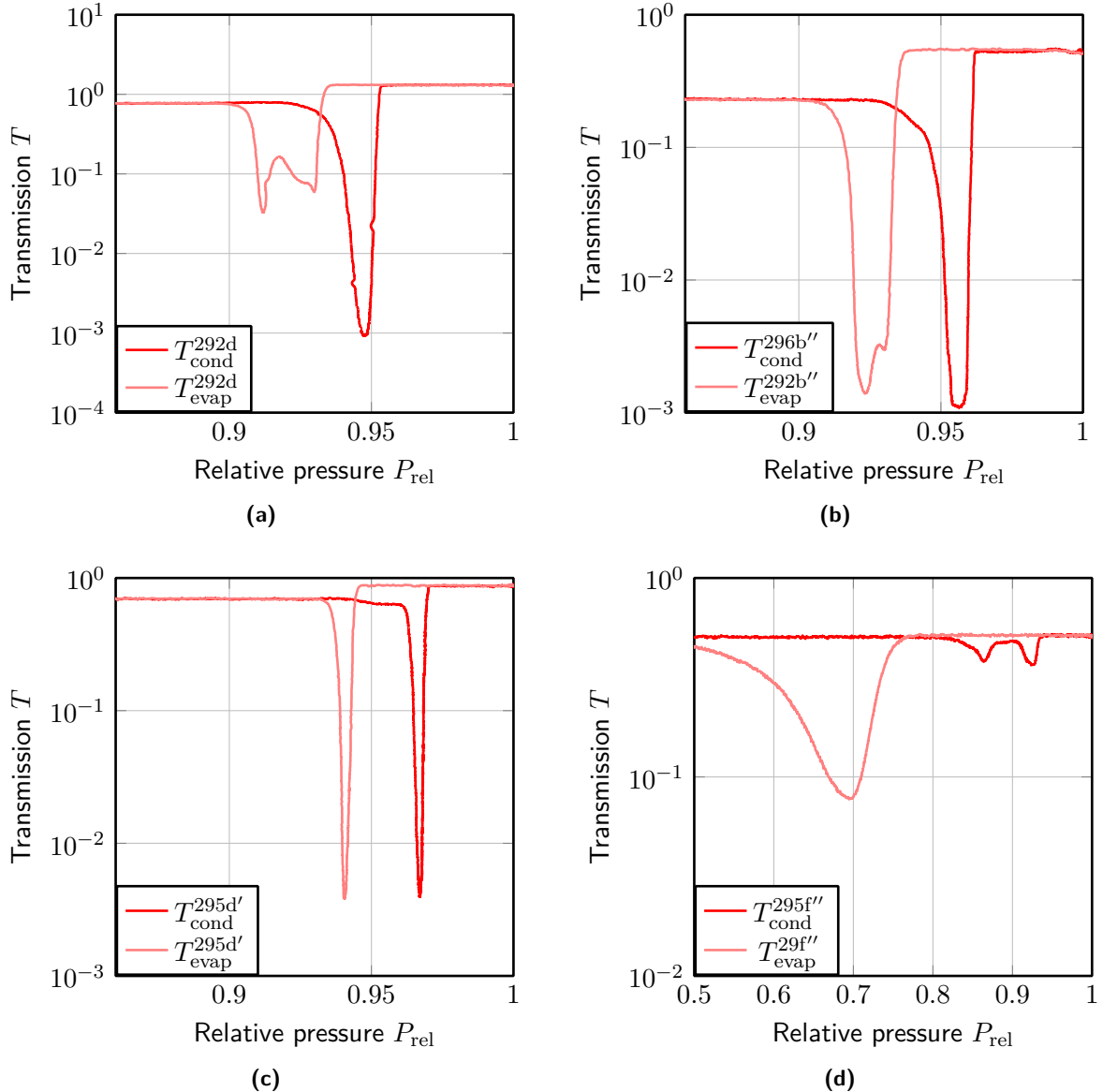


Figure 4.16 P_{rel} transmission isotherms of the membranes 292d (a), 296b' (b), 295d' (c), and 295f'' (d). All membranes have open pores. Unlike the isotherm of membrane 292d, the transmission drops of condensation and evaporation are of the same magnitude. The magnitudes of condensation and evaporation dip are reversed in respect to membrane 292d for membrane 295f 200ALD.

Firstly, a completely filled membrane should always yield a higher transmission coefficient T than it would in its dry state according to the theory of index matching explained in section 2.11. This fact serves as a tool to optically detect membranes that do not fill completely due to constrictions which by experience show a weaker transmission after the condensation process is complete than they did before. Furthermore, due to the disorder created by pore filling and emptying, the transmission drops during the processes. Phenomena occurring on the volumetric measurements can therefore be linked to the measured transmission coefficient.

Moreover, the phenomenon of the transmission dropping to lower values for the condensation than for evaporation branch of a given isotherm has been repeatedly observed on open pore membranes. An example is given by membrane 292d's isotherm which is displayed in fig. 4.16(a). At this point it must be mentioned that all open pore membranes measured before the wafers 295 and 296 have

shown this same transmission characteristics. As interpretation serves the degree of disorder caused inside the membrane by the respective process. As the membrane contains pores open on both ends, the condensation occurs at spinodal pressure $P_{sp}(d_{pore})$. Due to the distribution of pore sizes, funnelization, corrugation and constrictions, the pores fill at different pressures $P_{sp}^1 \neq P_{sp}^2$. At a given pressure

$$P_{sp}^1 < P < P_{sp}^2,$$

where P_{sp}^1 shall correspond to the smallest pore diameter found on the membrane and P_{sp}^2 the largest one, the state of the membrane regarding filled and empty pores is assumed to be comparable to figure fig. 4.17(a). The hexane evaporates at equilibrium pressure P_{eq} , though. That means that, assuming the same pore size distribution, funnelization, corrugation and constrictions, the pores empty continuously. The theoretical state of the membrane is visualized in fig. 4.17(b).

The difference is given by the most significant contrasts between neighboring pores during the condensation process, in explanation empty and filled pores, for spinodal condensation, while for evaporation at equilibrium pressure the pores only show different levels of liquid during most of the process. As a result, the absorption of hexane creates a higher grade of disorder than the desorption and therefore causes a more significant drop of the transmission coefficient (compare fig. 4.16(a)).

The splitting of the evaporation drop into two dips separated by a small local maximum cannot be explained by this theory, nor by any other means mentioned in this report. Moreover, the later analysed membranes of wafer 295 and 296 yield a more even dip distribution (compare fig. 4.16(c) and fig. 4.16(b)) and upon reducing the pore diameter of 295 using ALD, the membranes even show the inverse behaviour (fig. 4.16(d)).

In connection with the sharper isotherms, the first phenomenon could be explained by the pores being less flawed talking corrugations and funneling. The latter assumption is backed by the fact, that the transmission drops of 295d are of smaller magnitude than those of 296b. While both are open pore membranes, membrane 295d is only half as thick as 296b, meaning the pores are only half as long and therefore the influence of the funneling aspect is reduced as will be explained in section 4.4.4.

The second phenomenon of the deeper evaporation dip remains unclear though.

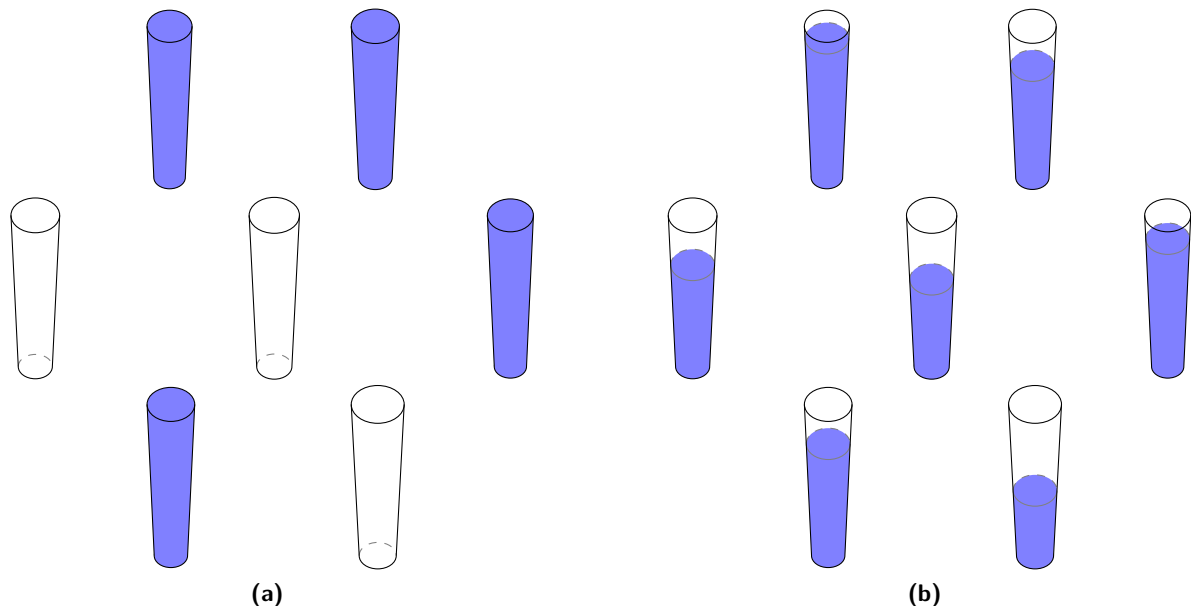


Figure 4.17 Disorder between neighboring pores during absorption (a) and desorption (b). Important is the larger degree of disorder upon the absorption process. Upon condensation pores fill immediately when the spinodal pressure $P_{sp}(d_{min})$ is reached, where d_{min} is the radius of the opening at the small end. The evaporation is continuous at equilibrium pressure $P_{eq}(d)$ and empties each pore simultaneously while the diameter d is large enough.

4.5 Pore quality linked to transmission drop and hysteresis

As of now the shapes of the isotherms are more familiar to the reader, at this point the isotherms of the open pore membranes of wafer 295 are analysed in more detail. For this please refer to the isotherms shown in fig. 4.6(b) of section 4.3. There are two isotherms that sting the eye as they do not blend in: The membranes 295d' and 295g'. Again, the analysis of membrane 295c' shall be postponed. Focusing on 295d' shows that its isotherm is not only shifted to larger pressures in comparison to the other membranes, but also is the hysteresis smaller. Moreover, the transmission drops are of a smaller magnitude for membrane 295d' than for all others. As the pressures translate to diameters

$$d_{\text{pore}} > 60 \text{ nm}, \quad (4.27)$$

KELVIN equation is assumed to be sufficiently correct. The isotherms of the membranes 295d' and 295g', which is from here on used as a representative of the rest of the open pores membranes of wafer 295, are plotted over a diameter axis in section 4.5. Interesting at this point is, that hysteresis is actually smaller for membrane 295g' on a KELVIN diameter scale. Also, the evaporation branch seems sharper which could account for less funnelled pores.

Very weird stuff here... HELP???

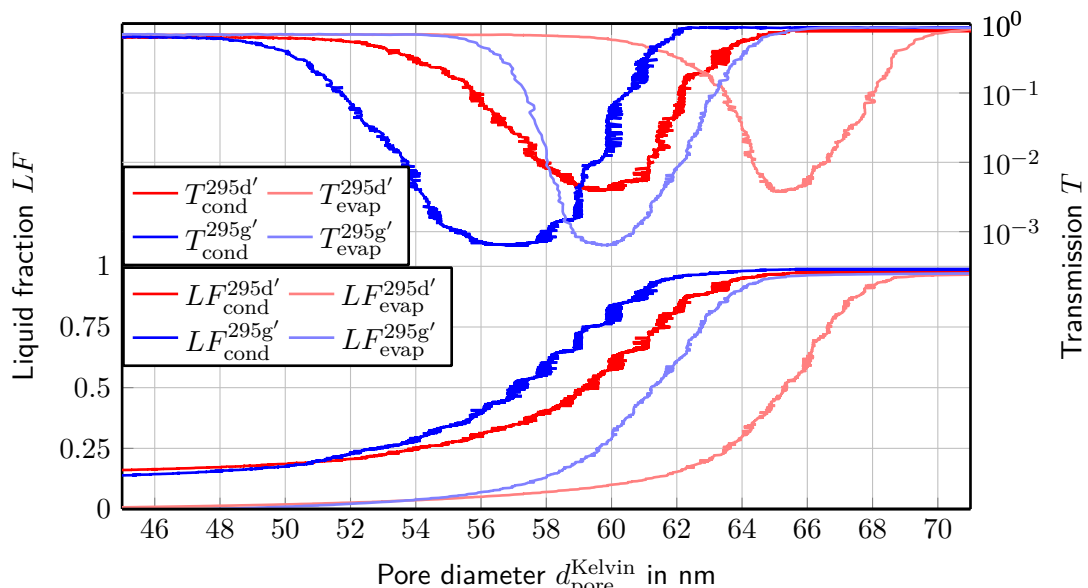


Figure 4.18 Comparison of the isotherms of the membranes 295d' and 295g' on a KELVIN diameter axis. Important for the analysis in section 4.5 is.

4.6 Testing theory using electron beam microscopy

4.7 Pore size reduction using atomic layer deposition

Finally, as the open pore membranes of wafer 295 prove to be very good in the sense of producing very sharp isotherms and showing similar diameters, the goal of sub ten nanometer pore diameters is resumed. The pore diameters are reduced using atomic layer deposition (ALD). ?? shows the treatments and measurements of the inspected membranes of wafer 295.

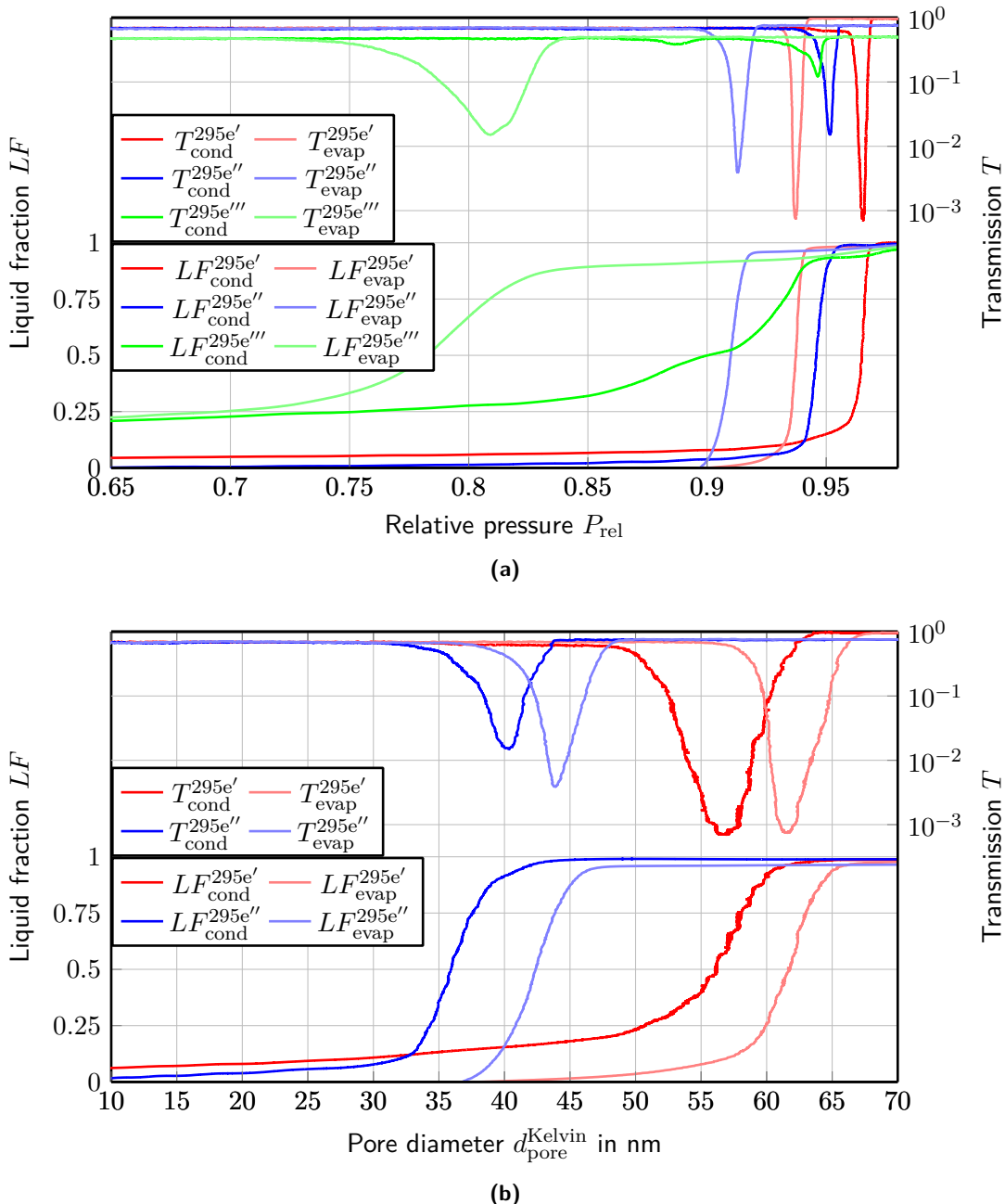


Figure 4.19 Comparison of membrane 295e' in initial open pore state and after 100 and 200 cycles of ALD over relative pressure axis in (a). While the shape of the isotherm does not change for the first 100 cycles, the result after the second 100 cycles is drastic. (b) shows the comparison of initial state membrane 295e' and 100 cycles of ALD membrane 295e'' on a KELVIN diameter axis. For analysis please read section 4.7.

4.7.1 Atomic layer deposition effectively reduces pore diameters

The first important question is if ALD works to serve as a diameter reduction at all. Therefore, on membrane 295e' 100 cycles of ALD are conducted and the membrane then probed using the experimental setup and SEM. The measurement results are shown in fig. 4.19. While the result for the first 100 cycles of ALD matches expectations perfectly, the second 100 cycles give a very different impression, though, and its result's discussion shall be postponed in favor of the analysis of 295e' and 295e'' at this point.

Firstly, the shape of the volumetric isotherm does not change for membrane 295e'' in comparison to 295e'. It is only shifted towards lower pressures. Only the hysteresis increases by a little bit which can be explained by the logarithmic context of relative pressure to pore diameters though. Regarding the isotherms of 295e' and 295e'' on a KELVIN diameter axis as shown in fig. 4.19(b), the change of the hysteresis disappears and the evaporation branches show the same spread for both membranes. Furthermore, the diameter reduction by 100 cycles of ALD according to the isotherms is

$$\Delta d_{\text{pore}}^{295e' \rightarrow 295e''} = 20 \text{ nm} \quad (4.28)$$

which makes for

$$\Delta = 0,2 \text{ nm} \quad (4.29)$$

diameter reduction per ALD cycle. This value matches the expectations of

$$\Delta = 0,2 \text{ nm} \quad (4.30)$$

per cycle as explained in ???.

The transmission measurements also yield very sharp drops for the membranes 295e' and 295''. One phenomenon, which has not been observed before, is that the evaporation transmission drop of membrane 295e'' is deeper than its condensation transmission drop. This does not go together with the theory for the before observed inverse phenomenon as explained in section 4.4.5. Up to this point, no explanation could be found for the observation.

4.7.2 Diameter reduction by atomic layer deposition is reproducible

Next, membrane 295e'' and 295f'' must be compared to probe the reproducibility of the pore diameter reduction using atomic layer deposition. As on the one hand the membranes 295e' and 295f' yielded equivalent measurement results as can be seen in fig. 4.6(b) and on the other hand both, 295e'' and 295f'', have undergone 200 cycles of ALD in total, their measurements should produce very similar results.

The measured data is plotted in fig. 4.20. While the overall picture of the two membranes seems to match, clearly there is a shift towards lower pressures visible for membrane 295f''. Anyways, the membranes used for this comparison both show isotherms that do not match expectations and imply that the atomic layer deposition did not work out properly. As, according to section 4.7.1, it works for only 100 cycles and also the result seems independent of the ALD process being interrupted during the full 200 cycles, leads to the conclusion that something is off for smaller diameters which will be further analysed in the following section. Talking reproducibility, a tendency towards yes is justifiable but needs to be confirmed through further experiments.

4.7.3 Atomic layer deposition parameters need improvement

In the following, the transition from membrane 295e'' to 295e''' using 100 layers of ALD shall be tried to understand. ?? shows the measured isotherms over a relative pressure axis. The condensation in two steps together with a one step evaporation hint at a population of closed or constricted pores. Therefore, the isotherms are plotted on a KELVIN diameter axis in fig. 4.22(b) twice, once using the

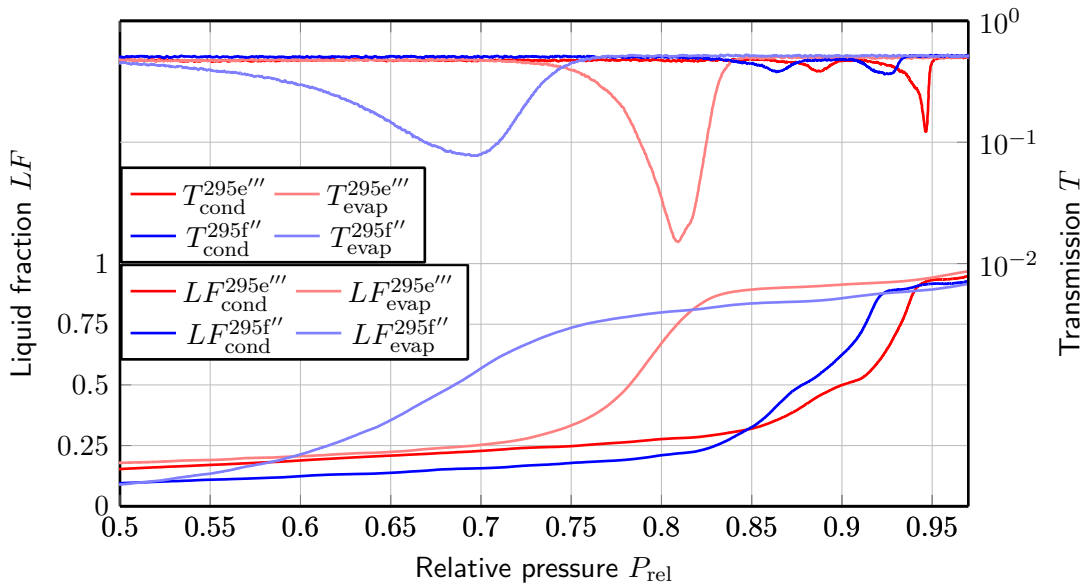


Figure 4.20 Full comparison of the closed pore membranes of wafer 296 with the open pore membrane 296b'. For interpretation please refer to section 4.4.

conversion for open pores (cylindrical meniscus) and once that closed pores (spherical meniscus). A black circle marks where the two steps of the isotherm's condensation branch superimpose on the same diameter range as a result. Moreover, another circle marks the corresponding transmission drops. They are both shifted towards higher pore diameters in comparison to the volumetric signals of condensation, but still, they are aligned on top of each other. These observations back the suspicion of closed or constricted pores.

Already in section 4.7.2, the similarity between the results of the membranes 295e''' and 295f'' has been analysed. For the sake of completeness, the same analysis as for membrane 295e''' shall be done here. Again, the two step condensation together with the single step evaporation hint at closed or constricted pores. Using KELVIN equation to convert the relative pressure to diameters for closed and open pores yields the same superposition as observed for membrane 295e''', again marked by black circles for volumetrics and optics. In addition to the volumetric and the transmission measurements, for membrane 295f'' SEM images have been taken. Figure 4.23(a) and fig. 4.23(b) show the solution and aluminum side of the membrane. The pore diameters of

$$\begin{aligned} d_{\text{pore,SEM}}^{295d'',\text{Sol}} &= 27 \text{ nm}, \\ d_{\text{pore,SEM}}^{295d'',\text{Al}} &= 27 \text{ nm} \end{aligned} \quad (4.31)$$

approximately match the diameters derived from the condensation branches of the volumetric isotherms whereas the evaporation branch would imply pore diameters of about

$$d_{\text{pore,evap}}^{295d''} = 10 \text{ nm}. \quad (4.32)$$

Up to this point though, the evaporation branch has been assumed to be more precise for measuring the pore diameters as it only depends on equilibrium pressure.

??? KELVIN IS NOT RELYABLE AT THESE LOW DIAMETERS - RATHER TRUST EVAPORATION -> constricted pore ends ! CHECK FOR CONDENSED LIQUID AND COMPARE TO EXPOECTATION!!!

Finally, section 4.7.3 shows the isotherm data for membrane 295d''. While there is still a volumetric signal visible, its pressurewise position does not match expectations as the deposit of 250 layers should make for smaller pores than the 200 layer on the membranes 295e''' and 295f''. Therefore, the signal might very well just be due to noise of the measurements. On the other hand, Also the

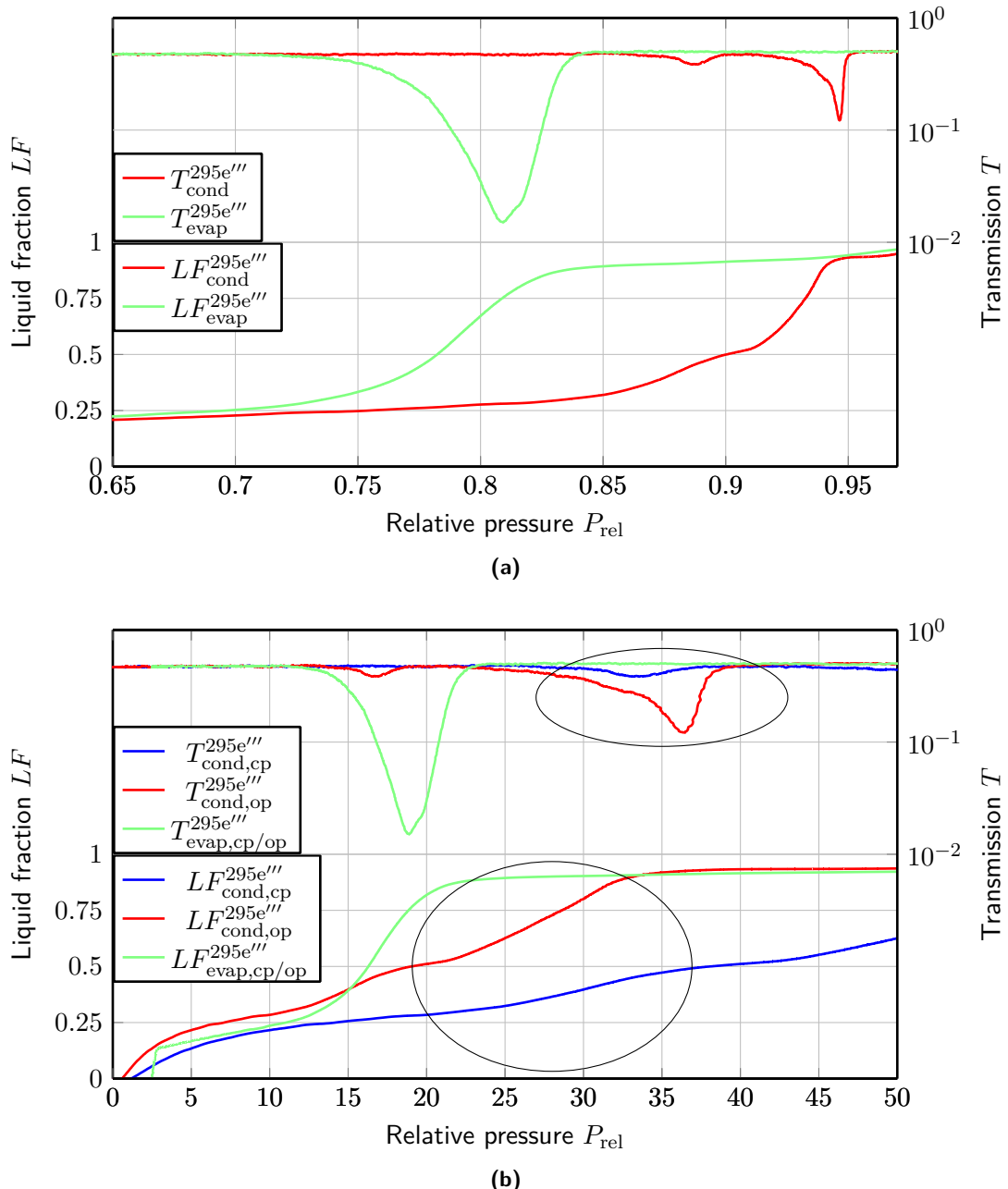


Figure 4.21 Plots for the analysis of membrane 295e''. (a) shows the isotherms over relative pressure while (b) shows it over a KELVIN diameter axis. On the latter graph, the isotherm data of membrane 295e'' is converted once using the KELVIN equation for open pores and once using it for closed pores. The black circles mark the overlap of the signals on the same diameter range.

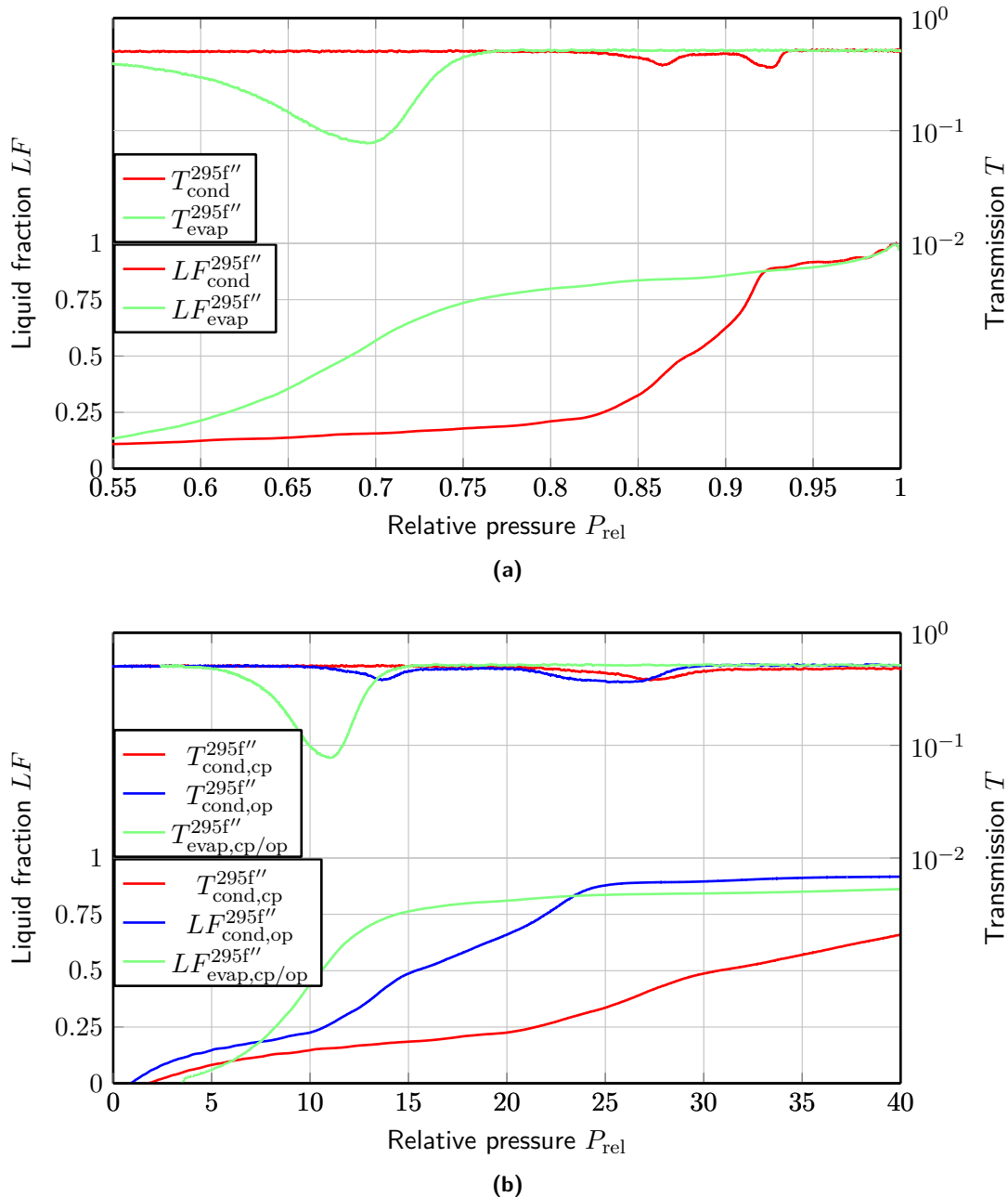


Figure 4.22 Plots for the analysis of membrane 295f''. (a) shows the isotherms over relative pressure while ?? shows it over a KELVIN diameter axis. On the latter graph, the isotherm data of membrane 295f'' is converted once using the KELVIN equation for open pores and once using it for closed pores. The black circles mark the overlap of the signals on the same diameter range.

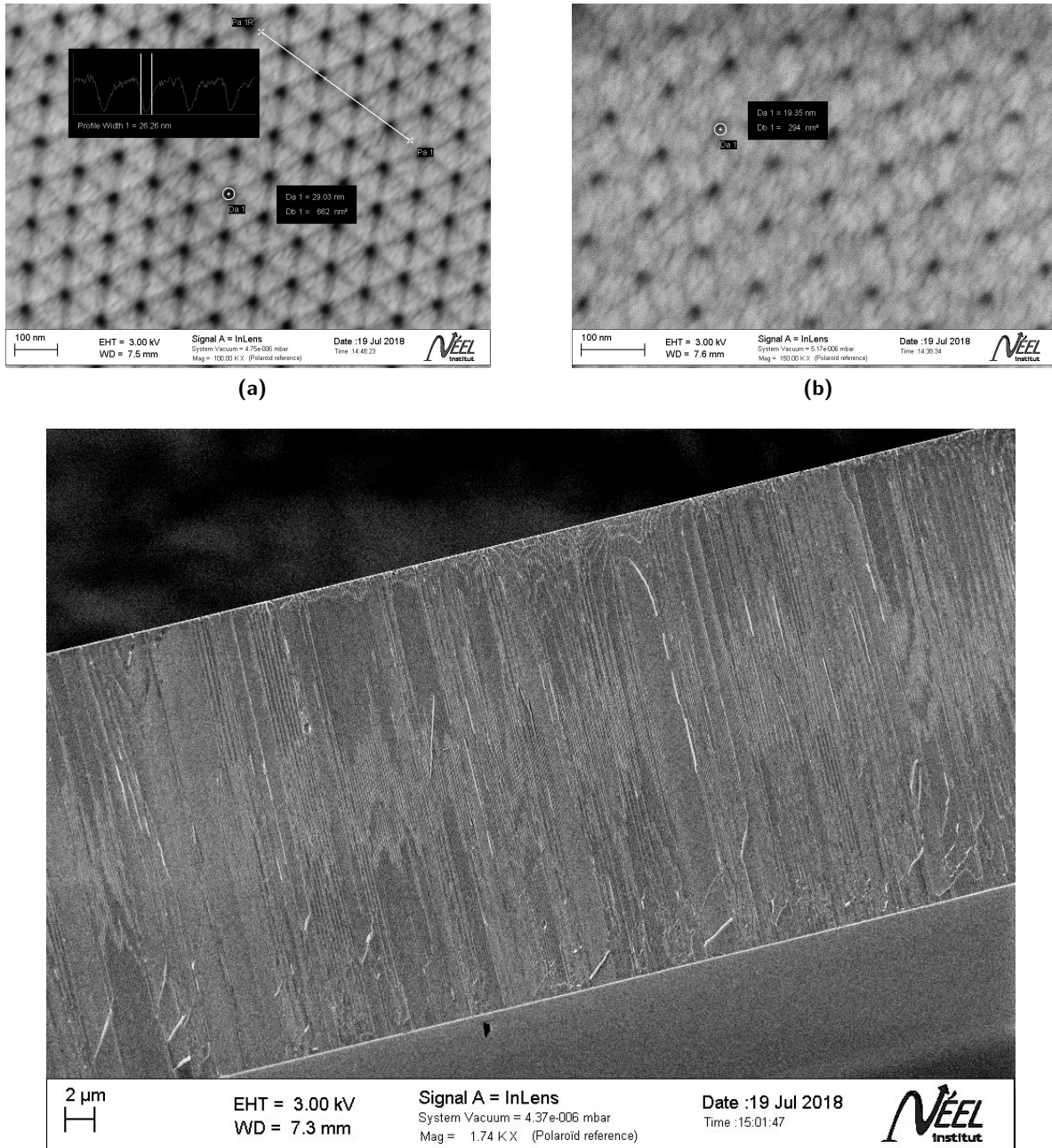


Figure 4.23 Electron beam microscopy images of membrane 295f''. (a) and (b) show images of the solution and aluminum side with pore diameter measurements. (c) captures the grayscale gradient on the membrane's cross section which gets lighter upon approaching the center from both sides.

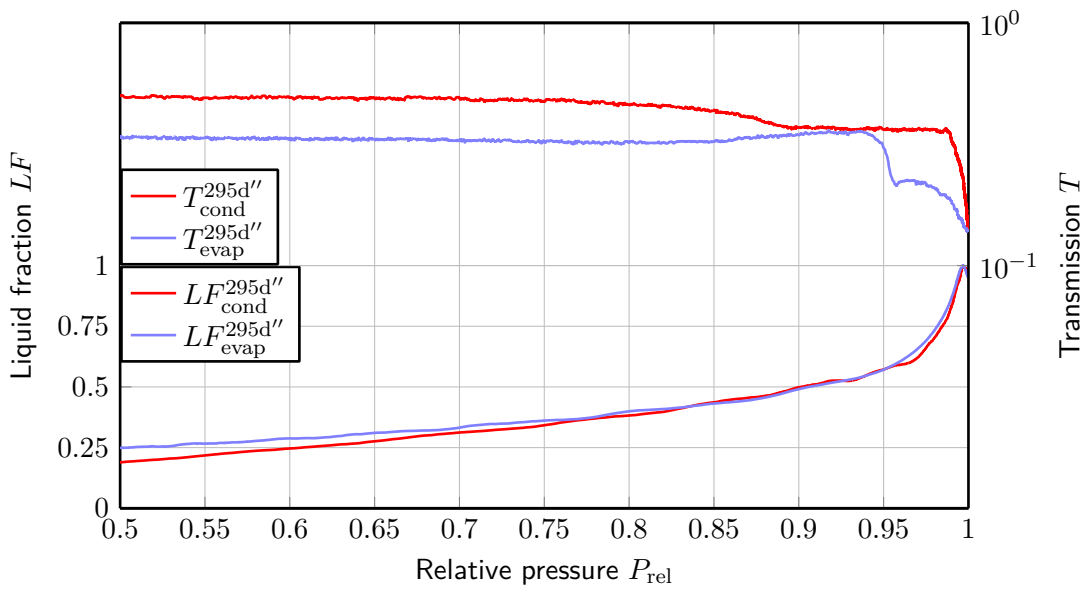


Figure 4.24 Isotherm measurement of membrane 295d''. The volumetric isotherm does not show any signal whereas the transmission measurement yields a lower transmission coefficient at saturated vapor pressure than in vacuum.

transmission signal shows a drop. The signal does not rise again even at saturated vapor pressure though. The latter observation implies constricted pores that do not fill at all.

4.8 Isotherms proves powerful to detect and characterize defects

Throughout the data evaluation, the volumetric measurements along with the laser transmission prove extremely sensitive to detect pore defect like closed pores, where they should be open, constrictions at the pore ends, corrugations or even funnellization. As a last example, membrane 295c' shall be analysed and the result applied to the other membranes of wafer 295.

Expectations are that membrane 295c' shows the same properties as the other open pore membranes of wafer 295 as they were all floated on phosphoric acid still attached to the initial wafer except for 295b'. Figure 4.25(a) displays its isotherm. In contrast to expectations, the isotherm shows a three step condensation branch while the evaporation branch consists of a single drop. An evaporation at high pressures that consists of a single sharp drop implies that all pores are distributed around a single diameter. As a consequence, the isotherm is plotted over pore diameters d_{pore} using KELVIN equation (section 2.5) for closed pores and open pores separately and superimposed in one coordinate system (fig. 4.25(b)). As the black circle tries to focus on, the first small rise at low pressures translates to the same pore diameter as the second one does for open pore analysis. This hints at a small population of closed pores on the wafer. In fact, the MEB images of the aluminum side of membrane 295c shown in fig. 4.26 actually do show areas of none open pores which fill at equilibrium pressure which is coherent with the before made assumptions based on the volumetric isotherms. Moreover, regarding the laser transmission signal, another phenomenon implying pores filling at equilibrium pressure can be found. As amplified in fig. 4.25(a), the transmission drops at about the same pressure as the first liquid fraction rise finishes and stays at this lower value until the occurrence of the spinodal condensation where it drops farther. This drop can be explained by some pores filling and scattering light as a result as before explained in ?? referring to fig. 4.17(a).

As for the third rise of the volumetric isotherm's condensation branch, it can be explained by pore size distribution of open pores with two peaks. As there is no known reason for this kind of distribution, this explanation seems unlikely though. At this point, no other interpretation has been concluded with.

Bring up membrane 293 (constricted pore ends) and membrane 295c (closed pores). MAYBE PUT THIS IN THE CONCLUSIONS CHAPTER???

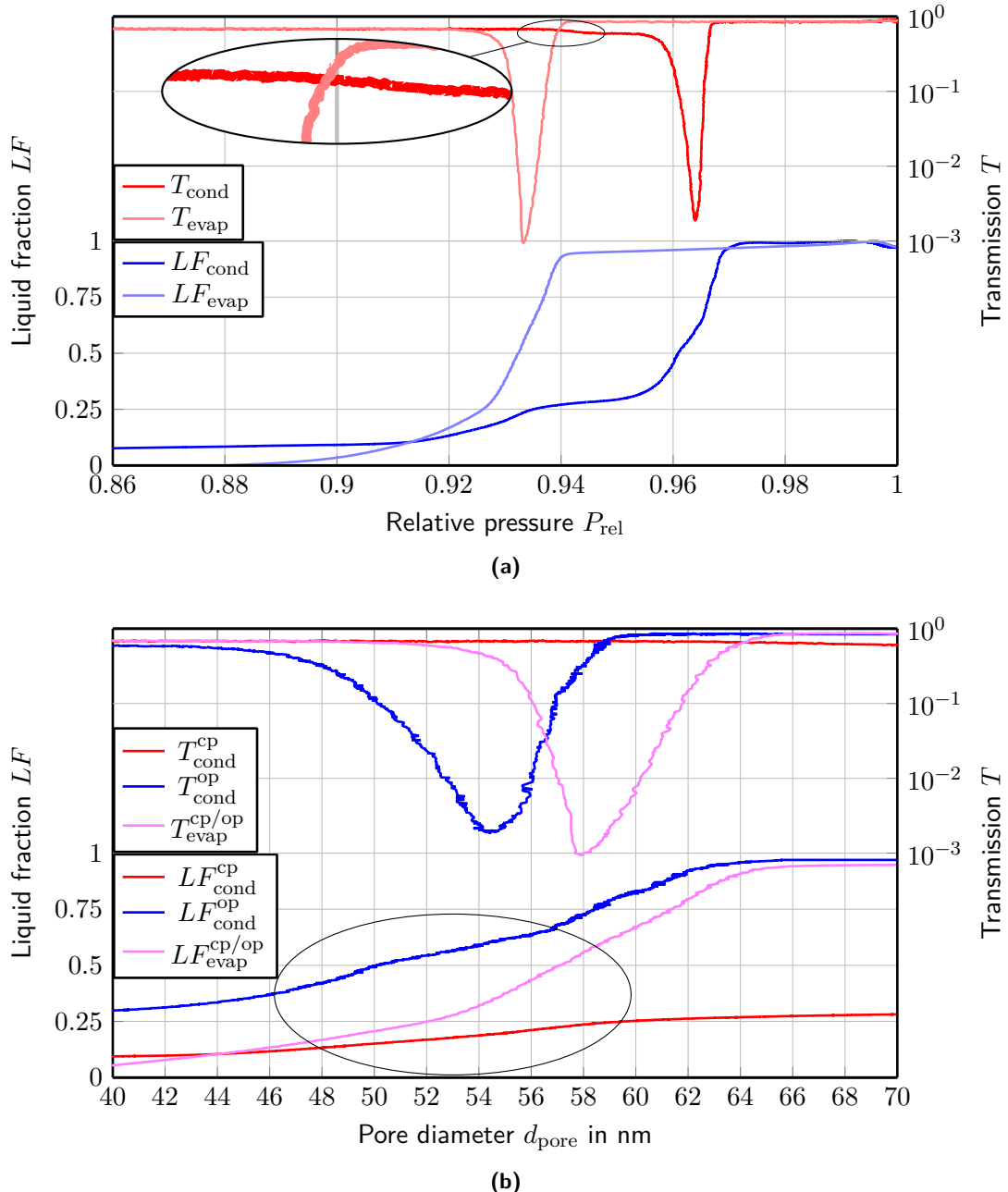


Figure 4.25 The isotherm of membrane 295c is shown in (a). To analyse the two step condensation, the isotherm is plotted on a pore diameter scale using the KELVIN equation (section 2.5) once under the assumption of condensation at equilibrium pressure for closed pores (cp) and once under that of spinodal pressure for open pores (op) in (b). For interpretations please read ??.

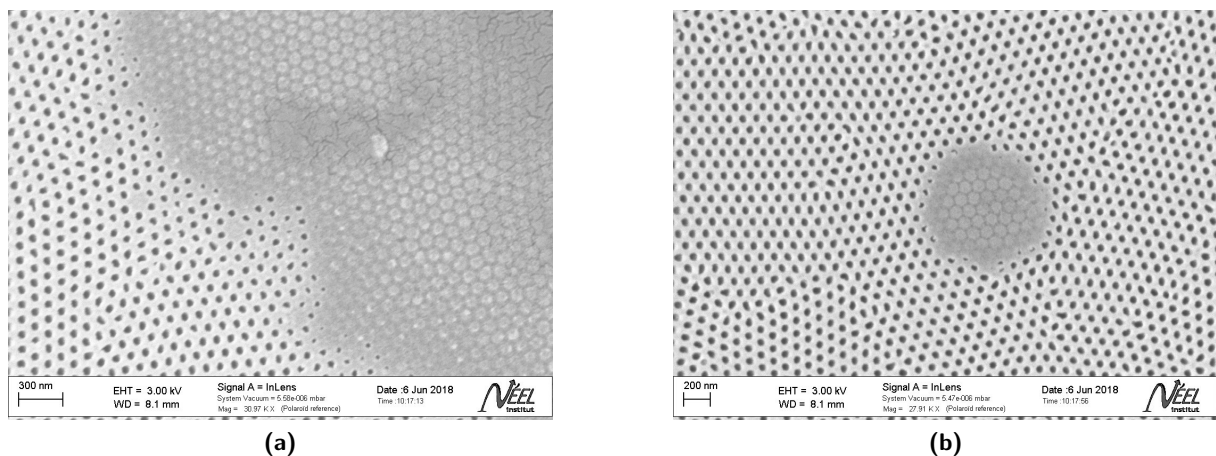


Figure 4.26 MEB images of the aluminum side of membrane 295c. Areas of none open pores are clearly visible.

Bibliography

[Cd15] Universität Konstanz: Corporate Design Manual. Universität Konstanz, (2015)